6 Pressurization and Pumping

The polymeric melt generated by the melting step must be conveyed and *pressurized* or *pumped* by the processing machine to force it *through* dies, or *into* molds, to assume useful shapes. This is the subject matter of this chapter.

We shall analyze pressurization, starting with its basic principles. First, by analyzing the various terms in the equation of motion, we deduce the possible mechanisms for pumping and pressurizing a fluid. This exercise maps out the theoretical envelope of pressurization mechanisms. Then, via a set of logical deductions, we uncover the simplest and most fundamental geometrical elements of *all* pumps, which through a sequence of systematic steps will lead us to a rich arsenal of machine configurations, among them, not surprisingly, most common pumps. In fact, this latter step serves as a formal means to *synthesize* or *invent* novel machine configurations. Finally, we examine in some detail the mathematical modeling of the most important, common machine configurations, deriving practical *design* equations.

Pumping or pressurization is perhaps the most characteristic polymer processing step, because it shows how dominant an effect the very high viscosity of polymeric melts has on processing machine configurations. High viscosity mandates very high pressures to force the melt through restrictions at the desired processing rate. Extrusion pressures up to $50\,MN/m^2$ (500 atm) and injection pressures up to $100\,MN/m^2$ (1000 atm) are not uncommon in practice. We shall see that most machines have *narrow gap* configurations, which not only enable the generation of high pressures, but also provide for good temperature control of the melt and lead to relatively short residence times. Furthermore, we shall also see that the common, practical processing machines have not only relatively short residence times but also narrow *residence time distributions*, enabling them to process temperature-sensitive polymeric materials.

Principles of Polymer Processing, Second Edition, by Zehev Tadmor and Costas G. Gogos.

6.1 CLASSIFICATION OF PRESSURIZATION METHODS

The response of a fluid to external forces is governed by the equation of motion. Therefore, by carefully analyzing the various terms of the equation of motion

$$\rho \frac{D\mathbf{v}}{Dt} = -\boldsymbol{\nabla} P - \boldsymbol{\nabla} \cdot \boldsymbol{\tau} + \rho \mathbf{g} \tag{6.1-1}$$

we can discover *all* the possible and fundamentally different pressurization mechanisms.

We first note that the equation of motion provides information only on pressure *gradients* in the liquid, and provides no information regarding the *absolute* value of the pressure. The latter is determined by *external* conditions imposed on the system. For example, the pressure in a liquid contained in a cylinder equipped with a plunger is determined by the *force* exerted by the plunger on the liquid, plus the hydrostatic head. We classify this pressurization method as *static pressurization*, because the pressure can be maintained without flow and without motion of the containing walls. The level of pressure that we can generate by this method is independent of the *rheological* properties of the fluid. Furthermore, the flow that results from this pressurization method, if we provide an exit for the liquid, is called *positive-displacement flow*. We already encountered this type of flow in Chapter 4 in solids conveying. The outstanding characteristic of this type of flow is an external surface moving *normal* to its plane and thus *displacing* part of the fluid. This pressurization method is used quite extensively in polymer processing, for example, in injection molding, compression molding, counterrotating fully intermeshing twin screw extrusion, and gear pump extrusion.

An alternative means for generating pressure in a fluid is by inducing an internal *pressure gradient*. To achieve this, a positive gradient in the direction of flow is needed for generating pressure. The equation of motion indicates that a nonzero pressure gradient can, in principle, be generated if any of the remaining three terms ($\rho D\mathbf{v}/Dt$, $\boldsymbol{\nabla} \cdot \boldsymbol{\tau}$, and $\rho \mathbf{g}$) has a nonzero value. The first term may acquire a nonzero value only if the fluid is in motion and there is acceleration (or rather deceleration). The second term will acquire a nonzero value only if the fluid is under deformation. Hence, these are defined as *dynamic pressurization mechanisms*. The third term, which is the gravitational term, creates a hydrostatic pressure gradient and is utilized, for example, in casting.

Since polymeric melts are characterized by having high viscosity, the dominant pressurization mechanism stems from $\boldsymbol{\nabla} \cdot \boldsymbol{\tau}$ (which is proportional to viscosity). Clearly, the higher the viscosity, the larger this term becomes, and potentially larger pressure gradients can be generated. Thus, the high viscosity of the polymeric melts becomes an asset in this pressurization mechanism.

The purpose of pressurization is to *generate* pressure as pumps do (as opposed to lose pressure, as in pipe flow). This can only be achieved by a moving external surface that "drags" the melt, leading to *drag-induced flows*. Indeed, the outstanding characteristic feature of *viscous dynamic pressurization* is a surface moving *parallel* to its plane. This, unlike a surface moving *normal* to its plane, will not displace the liquid, but *drag* it along. The high viscosity implies high momentum transport rates normal to the moving surface. Single screw extruders (SSEs), co-rotating intermeshing twin screw extruders (TSEs), calenders and roll mills, and co-rotating disk processors generate the pressure needed to shape, form, and mix the material by this mechanism.

Viscous dynamic pressurization is not the only pressurization mechanism that stems from the $\boldsymbol{\nabla} \cdot \boldsymbol{\tau}$ term of the equation of motion. As discussed in Chapter 3, polymeric melts exhibit

normal stress differences, and these stresses may also yield a nonzero value to this term. Indeed, the normal stress extruder utilizes this mechanism of pressurization.

The $\rho D\mathbf{v}/Dt$ term in the equation of motion accounts for acceleration. In polymer processing this is not a very important source of pressurization. Yet centrifugal casting takes advantage of angular acceleration as a mechanism for generating pressure, and linear deceleration to generate ''impact molding.''

Finally we note that, in principle, a reduction in density can generate pressure in a closed system. Low-pressure structural molding and certain reaction injection molding processes involving foaming during the molding operation generate sufficient pressure to force the melt to fill the mold.

Although the equation of motion provides information on the *possible* sources of pressurization, the actual multitude of *realistic* geometric configurations that can make efficient use of these mechanisms is a matter of creative engineering design. In the next section, we propose a methodology for *synthesizing* or *inventing* such geometrical configurations in a rational and systematic way (1,2). This process will also help elucidate the pressurization mechanism of the machines and the underlying reasons for their particular shape.

6.2 SYNTHESIS OF PUMPING MACHINES FROM BASIC PRINCIPLES

Machine *invention* is clearly an act of *synthesis*, as is engineering design. In synthesis we *construct*, *assemble*, and *put together* ideas, elements, concepts, or combinations of these in order to create an artifact that hopefully does something useful. We combine elements into a whole, into a new entity.

In contrast to invention and engineering design, in science we mostly *analyze*. We *decompose* the whole into its constituent elements. We deconstruct. And, of course, this process of *deconstruction* helps us discover the laws of nature. Similarly, when the tools of analysis and the fundamentals of science are applied to technology, to an engineering discipline, or an industrial process, they are also decomposed into their fundamental building blocks and elements. These are then systematically arranged and generalized in order to create a formal structure. Then by *recombining* the elements and building blocks in novel ways into a *new* whole, inventions and innovations can be made. Thus, through *analysis*, the fundamental building blocks and elements of processes and machines can be uncovered, and after they are uncovered, they can be *reassembled* in a rather formal way in a myriad of different ways to create new inventions and innovations.

The historical origins of this approach, often referred to as the *morphological* approach, go back to Frantz Reuleaux (3), who was seeking an ''elementary structure of the machine simple enough to be general and exhaustive enough to provide designs for special constructions,'' and was later generalized by Simon (4), Hubka (5), and others. In this section, we apply this methodology to polymer processing.

In the previous section, by exploring alternative mechanisms for pressurizing a liquid, we arrived at two basic geometrical *machine elements*, namely, a plate moving normal to its plane and a plate moving parallel to its plane. These are shown in Fig. 6.1.

Next we take these two elements and combine them with a second *stationary* or *moving* plate to create the basic *building blocks* for machine design. A building block is the simplest geometrical configuration that captures the most fundamental element of the

Fig. 6.1 The two basic machine elements: a plane moving normal to its plane and a plane moving parallel to its plane.

pressurization mechanism. For example, we already demonstrated in Example 2.5 that two parallel plates in relative motion capture the mechanism of single screw extrusion pumping, and therefore this is the building block of the SSE.

There are 14 distinguishable building blocks that can be constructed from the two machine elements and a second plate placed parallel or at an angle to the machine elements, as shown in Fig. 6.2. Not all of them have the same practical significance, not all of them may lead to useful design solutions, but they are all clear, distinguishable machine building blocks.

Next we construct machine configurations using the building blocks. In order to do this we must first find a practical solution for creating a constantly moving ''infinite'' plate. This can, of course, be accomplished by employing rotational motion. In the case of the plate moving parallel to itself, Fig. 6.3 shows several possible alternatives for achieving such motion: an infinite moving belt, the outside of a solid cylinder, the inside of hollow cylinder, and the face of a disk. Many other geometrical shapes can create moving surfaces, but they will not differ fundamentally from the ones in Fig. 6.3.

In the case of a plate moving normal to itself there are two options: (a) via simple reciprocating action, as in reciprocating plunger pumps and injection and compression molding machines, which can also take the form of rolling cylinders, as in intermeshing counterrotating twin screws; and (b) by placing planes on a rotary element, as is the case with gear pumps. These are shown schematically in Fig. 6.4.

Now we proceed with the formal invention process by pairing building blocks with the foregoing design solution to the moving surfaces. A number of the examples that follow will clarify the process.

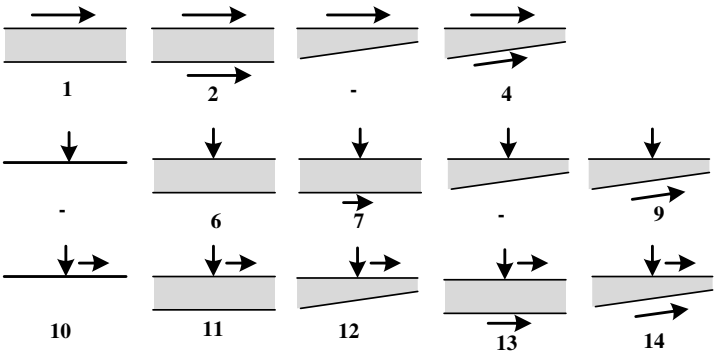

Fig. 6.2 Fourteen different building blocks created from the two machine elements and stationary plates. Note that motion of the second plane in the opposite direction will not create new building blocks because only the relative motion between the planes matters.

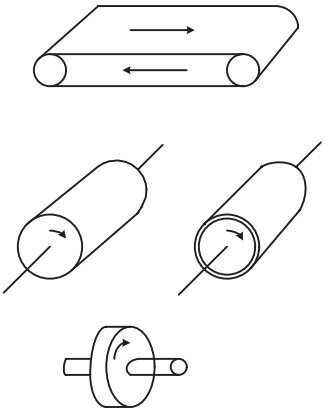

Fig. 6.3 Some design solutions for creating infinite surfaces moving parallel to their plane.

Example 6.1 The Synthesis of the Roll Pump Consider building block 1 in conjunction with an infinite surface created by a rotating solid cylinder, as shown in Fig. E6.1a(a) and Fig. E6.1a(b). The curvature of the cylinder does not change the concept and mechanism of drag flow. Next, the stationary surface must be created. The simplest solution is to place the solid cylinder inside a stationary barrel, as in Fig. E6.1a(c) and Fig. E6.1a(d), where in addition we created entrance and exit ports through the barrel separated by a solid obstruction.

Thus, we have invented a new geometrical configuration for a viscous pump. We can now easily construct a mathematical model and design such a pump for a desired pressure and flow rates. The pressurization capability of such a pump, at a given frequency of rotation and geometry, is proportional to the length of the flow channel. In our case, this will be one circumference. We can relax this constraint by assembling several rolls in sequence, as shown in Fig. E6.1b. This leads to an apparently infinite number of possible solutions, because in principle we can add as many rolls as we wish. Of course, most of these will not be practical solutions. Single roll extruders can be designed not only as pumps, but as complete processors

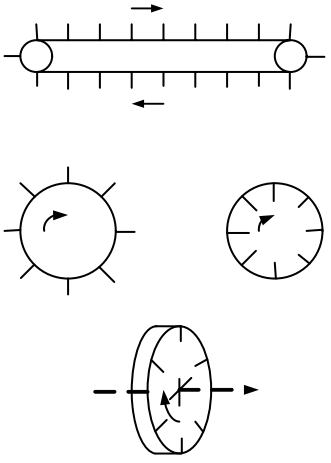

Fig. 6.4 Some possible design solutions for creating periodic continuous motion of a surface normal to its plane.

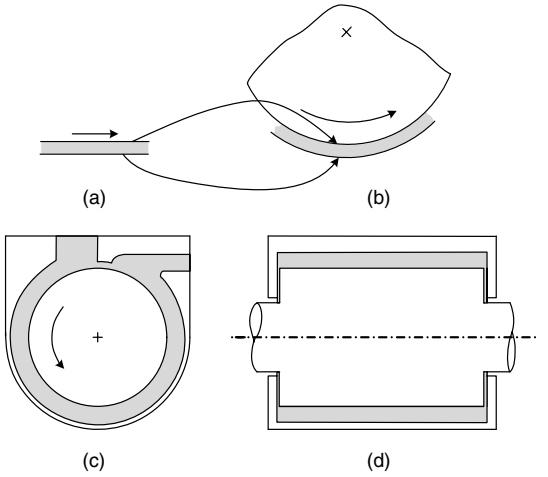

Fig. E6.1a The synthesis of a roll pump from building block 1. (a) The building block; (b) a rotating solid cylinder forms the moving surface; (c) the inner surface of a hollow cylinder forms the stationary surface. The two surfaces create a curved shallow pumping channel. Entrance and exit ports are formed by openings in the outer cylinder, and they are separated by a "channel block"; (d) side view of the roll pump.

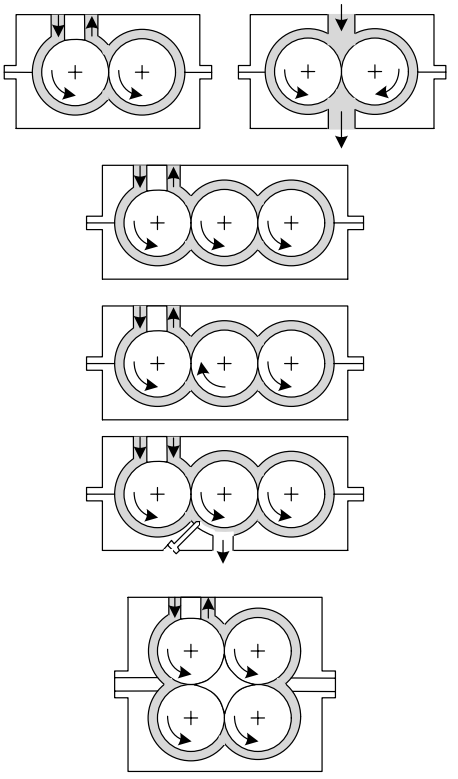

Fig. E6.1b Alternative design solution of a roll pump from building block 1. On the top we see two two-roll pumps: one co-rotating and the other counterrotating. The latter is a toothless gear pump; where the pumping mechanism is viscous drag rather than positive displacement. In the middle we have three three-roll configurations, and at the bottom a four-roll pump.

(1), and, in fact, such machines have been suggested and built (6,7). However, in practice they have too many disadvantages as compared to the screw-type processors, and are rarely, if ever, used.

Example 6.2 The Synthesis of the Inverse Single Screw Pump There is, however, another, more elegant way to relax the channel-length constraint, as shown in Fig. E6.2. After one circumference, a flow channel formed by the moving and stationary planes of a given width can be twisted helically by an amount equal to the width of the channel to create a much longer *helical* channel on the same roll or shaft. The channel itself can be simply machined onto the inner surface of the stationary cylinder or barrel.

By mathematical modeling, it can be shown that the twisting of the channel does not alter the mechanism of pressurization, but only slightly reduces the pumping efficiency. The motion of the moving surface, which now is at a certain angle to the direction of flow, reduces drag or pumping by a factor given by the cosine of this angle. But on the other hand, the twisting of the channel into a helical one brings about important gains. A cross-channel drag flow is induced, leading to better mixing and reduced residence time distribution. It enables the drag-removal melting mechanism to take place, and it also enables the operation of a partially filled channel for venting, devolatilization, and smooth

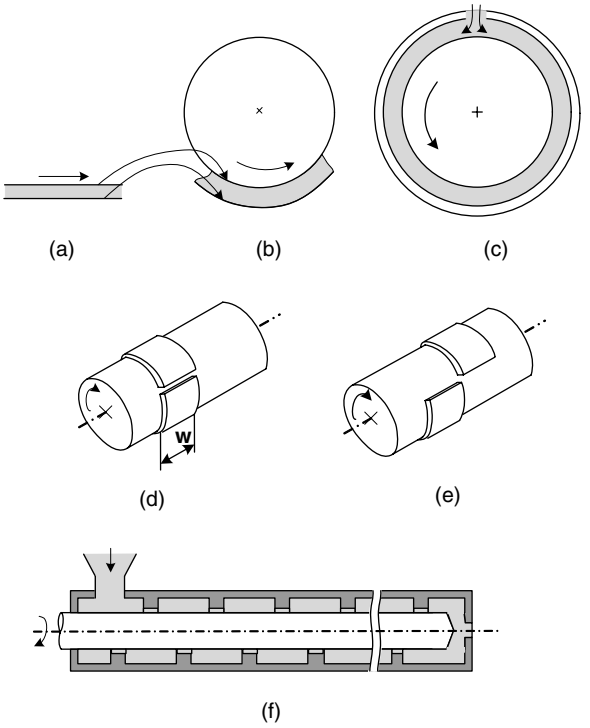

Fig. E6.2 The synthesis of an inverse screw extruder from building block 1. (a) The building block; (b) a rotating solid cylinder forms the moving surface; (c) the inner surface of a hollow cylinder forms the stationary surface. The result is a single roll processor without the channel block; (d) the shallow channel is wrapped around the rotating shaft. The maximum length of the channel is set by the circumference of the shaft; (e) a twisted channel relaxes the length constraint; (f) cross section of an inverse screw processor.

conveying of particulate solids. Finally, from a mechanical design point of view, the helical geometrical configuration makes it easy to feed the machine through an opening in the stationary barrel and discharge it by terminating the shaft, as shown in Fig. E6.2. The resulting machine is, in fact, an inverse screw extruder, where the screw channel is machined into the inside of the barrel and a smooth shaft rotates in it.[1]

Example 6.3 The Synthesis of the Hollow Cylinder Pump We take building block 1 and use the inner surface of a hollow cylinder as the moving surface. The procedure follows the same conceptual lines of design as outlined in the previous examples and it is clearly demonstrated in Fig. E6.3a. A small variation is to have the entrance and exit ports at different ends of the shaft, as shown in Fig. E.6.3b.

Example 6.4 The Synthesis of the Single Screw Extruder The SSE is the most common, important, and extensively used processing machine. It was invented and patented by Mathew Gray in 1879, although it is generally attributed to Archimedes (it is still called the ''Archimedes screw'') and the ancient Egyptians supposedly had the device long before that (8). Continuing in this distinguished tradition, this important machine configuration can

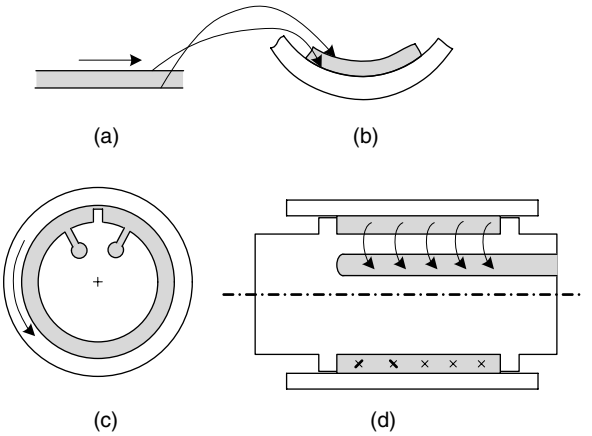

Fig. E6.3a The synthesis of a hollow cylinder pump. (a) The building block; (b) a rotating hollow cylinder forms the moving plane; (c) the stationary plane is formed by the outer surface of a solid stationary shaft. A channel block separates inlet and outlet. Feeding and discharge are carried out through slits in the shaft leading to axial holes drilled in the shaft; (d) the two surfaces that form a shallow curved channel are bounded by a sidewall or ''flight'' running along the circumference of the shaft.

1. Using this concept, a helical barrel rheometer (HBR) was developed. It is a single screw pump with a straight shaft and a helically wound channel mashined into the barrel, with the clearance being the difference between the barrel and shaft diameters. At closed discharge the pressure drop across one flight can be directly related to the melt viscosity, given the geometry and frequence of rotation. With this design the pressure trace is steady with time and not a saw-tooth as in an SSE screw pump, eliminating the need for pressure transducer time responce analysis. It is pressure generating and can thus be used as an online rheometer, since it can pump the sample stream back to the processing equipment. Additionally, since it can pressurize the melt during viscosity measurements, it is capable of measuring the effect of foaming agent diluents on the melt viscosity. [D. B. Todd, C. G. Gogos, and D. N. Charalambopoulos, U.S. Patent 5,708,197 (1998); D. B. Todd, C. G. Gogos, M. Esseghir, and D. W. Yu, ''Monitoring Process Viscosities with a New On-line Rheometer,'' *Plastics Eng*., **53**, 107 (1997); S. K. Dey, D. B. Todd, and C. Wan, ''Viscosity of Blowing Agent-laden Polymers,'' *SPE ANTEC Tech. Papers*, **50**, 3122 (2004).]

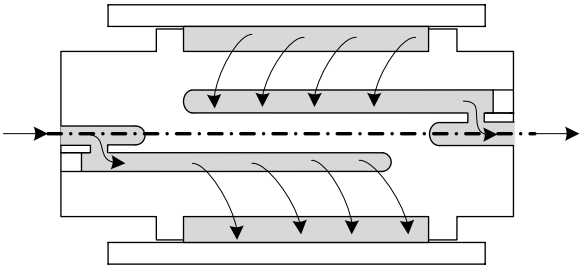

Fig. E6.3b Side view of a hollow cylinder pump with feed port at one end of the shaft and discharge at the other end.

easily be ''invented'' in a systematic way by pairing building block 1 with the inner surface of a rotating hollow cylinder, as shown in Fig. E6.4.

As in the inverse screw pump, we relax the channel length constraint to one circumference by twisting it and making it helical [Fig. E6.4(d)]. We create the helical channel by machining it onto a solid shaft, resulting in a screw. We now have a single

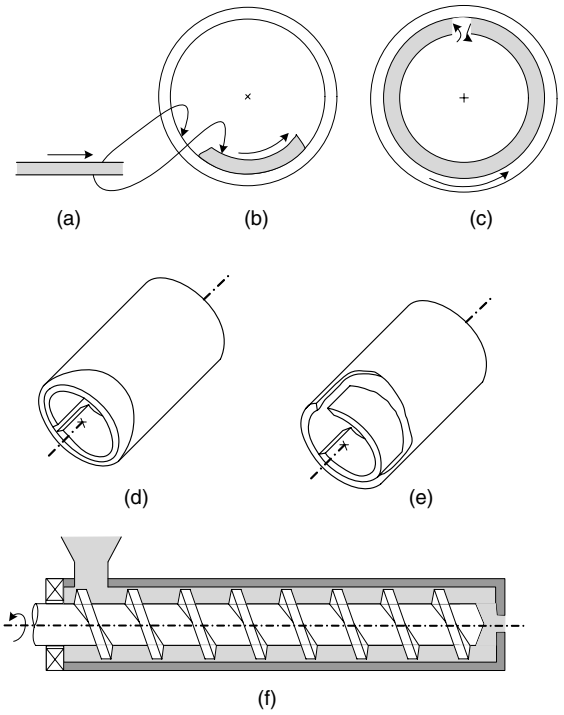

Fig. E6.4 The synthesis of the SSE for building block 1. (a) The building block; (b) a rotary hollow cylinder forms the moving plane; (c) the shallow channel of certain width spread over one circumference of the cylinder; (d) a twisted helical channel relaxes the length constraint; (e) the channel machined onto a solid shaft, the rotation of the cylinder interchanged with that of the shaft, and feeding and discharge ports fixed on the cylinder or barrel, resulting in an SSE.

screw placed inside a rotating hollow barrel. Next, we set the rotation of the barrel and that of the screw in opposite directions,[2] and then by creating an entry port in the barrel and terminating the screw for discharge, we obtain the SSE configuration, as shown in Fig. E6.4(e).

Example 6.5 The Synthesis of the Disk Processor In this example, we once again take building block 1 and pair it with the flat face of a rotating disk to obtain a disk processor, as shown in Fig. E6.5a. As was the case in the roll pump, the inlet and outlet ports are cut into the

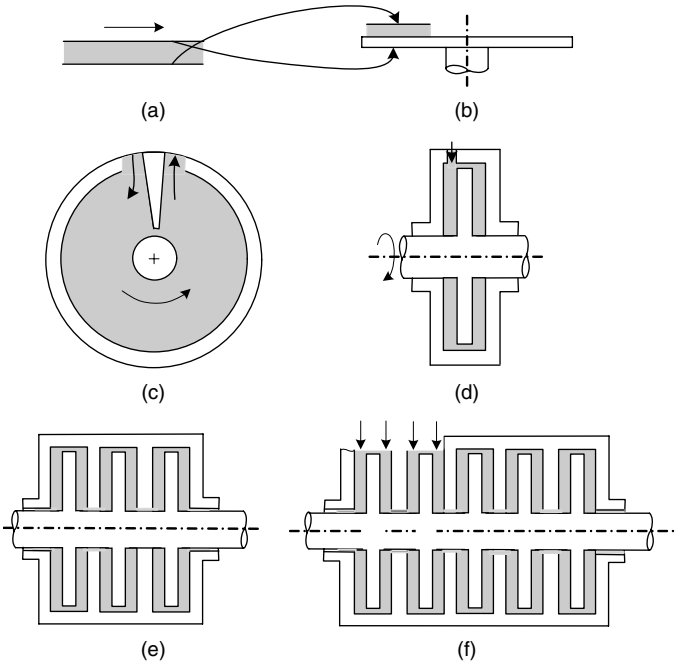

Fig. E6.5a The synthesis of a disk pump from building block 1. (a) The building block; (b) a rotating disk forms the moving plane; (c) front view of the pump in a closure with inlet and outlet ports separated by a channel block; (d) side view of the pump having two pumping chambers on either side of the rotating disk; (e) multichamber–multistage setup with material moving from stage to stage via ''transfer channels'' (not shown) machined in the closure connecting discharge port of the downstream chamber with the inlet port of the upstream one; (f) parallel-in series combination of chambers.

2. If centrifugal forces play no role in the mechanisms taking place in the machine, as is the case for viscous polymeric materials at common screw speeds, then from a fluid mechanics point of view, it makes no difference whatsoever if the barrel rotates or if the screw rotates in the opposite direction. A fluid particle in the screw channel is oblivious to what moves. It only senses the relative motion generating the shearing forces. However, it is far more convenient to place the coordinate system on the screw, because then the boundary conditions become far simpler, with stationary channel walls and a single surface (that of the barrel), moving relative to them. Moreover, we are interested in the motion of the melt relative to the stationary screw channel due to drag exerted by the barrel surface, and not relative to a stationary barrel on which rigid rotation is superimposed. Just consider a slippery barrel surface, which leaves the melt rotating in unison with the screw with zero output. Clearly, for a fluid particle, the screw will appear stationary. Therefore, in analyzing SSEs theoretically, we assume that the screw is stationary and that the barrel rotates in the opposite direction.

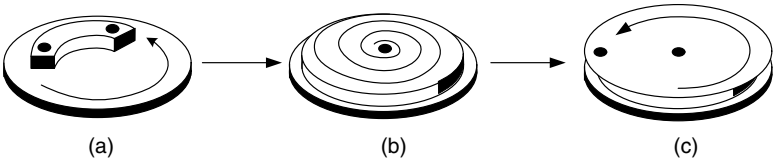

Fig. E6.5b The synthesis of a flat spiral pump from building block 1. (a) A section of the curved channel formed by a stationary plane and the rotating disk plane; (b) the extension of the channel into a flat spiral; (c) outside view of the flat spiral pump, with the spiral channel machined into the surface of one disk and another closely spaced rotating disk covering it.

barrel and separated by a ''channel block.'' Clearly, both surfaces of the disk can be utilized as shown in Fig. E6.5a(d). Moreover, like the roll pump, we can relax the length restriction by using a multichamber–multistage arrangement as in Fig. E6.5a(e), or by creating a spiral channel on the surface of the flat disk, as shown in Fig. E6.5b.

Example 6.6 The Synthesis of the Rotating Cup Pump We now take building block 2 and pair it with both a rotating solid cylinder and a hollow cylinder to create two moving planes, as shown in Fig. E6.6a. The separation between the axial inlet and outlet ports machined into the cover plate [Fig. E6.6a] is a bit cumbersome and has to be created by an axial channel block attached to the cover plate and extending into the cup. Apparently, no such machine actually exists and it may not be too useful, but the point is that this

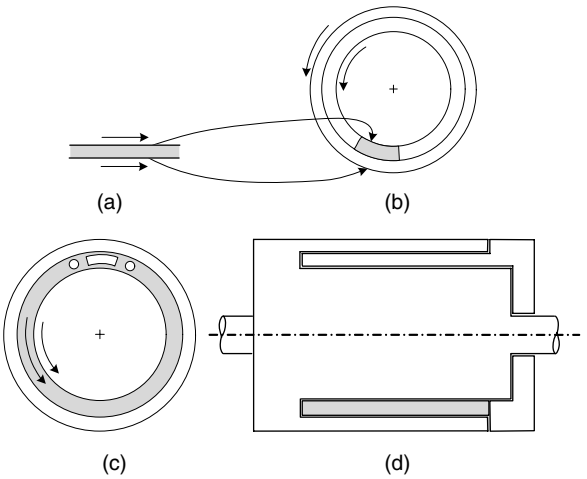

Fig. E6.6a The synthesis of the rotating cup pump from building block 2. (a) The building block; (b) a rotating solid cylinder and a rotating hollow cylinder for the moving planes; (c) the rotating elements are separated by a channel block with feeding and discharge ports shown on either side; (d) side view of the processor where the rotating elements are combined into a rotating cup and a stationary cover plate closure holds the channel block.

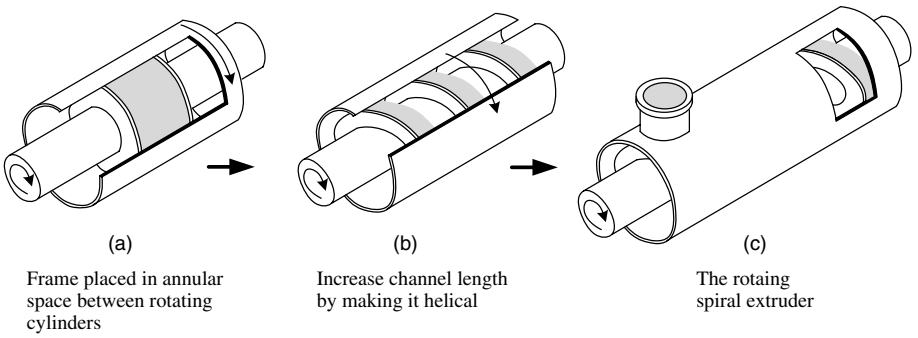

Fig. E6.6b The synthesis of the free rotating flight pump from building block 2. (a) an annular channel is created between the rotating shaft and hollow cylinder; (b) the channel is twisted and extended into a helical spiraling channel; (c) the channel is formed by a spiral that rotates between a stationary shaft and stationary barrel, with a feed port and exit port machined into the barrel.

novel configuration, which would surely work, emerged systematically from our ''invention'' procedure.

As in the previous examples, we can relax the channel length limitation either by adding a second stage using an axially rotating cup pump or alternatively, by creating a spiral channel between a rotating shaft and hollow cylinder, as shown in Fig. E6.6b. This leads to a rotating spiral pump which, when optimized, generates eightfold more pressure at the same frequency of rotation (for a Newtonian fluid) as the single screw pump. Building such a pump for viscous liquids and high pressure is mechanically rather challenging, but it is a common configuration for short solids feeders.

Example 6.7 The Synthesis of the Co-rotating Disk Processor The last example in synthesizing new machine configurations from building blocks is the co-rotating disk processor. Here we pair building block 2 with the moving planes of two rotating disks, as shown in Fig. E6.7. The disks are attached to a rotating shaft enclosed within a stationary barrel with inlet and outlet ports, separated by a channel block. The space thus created forms a processing chamber.

Processing chambers can be connected in parallel or in series. In the latter case, material can be conveniently transferred from one chamber to the next via transfer channels machined into the barrel. Heating and cooling of the disks can be accomplished by temperature-controlled liquids fed through rotary joints into the shaft and the disks. Theoretical analysis shows that this geometrical configuration is most effective not only for pumping but for all the other elementary steps as well. This configuration was invented by one of the authors (9) and the concept was commercialized by the Farrel Company in Ansonia, CT (10–16), which manufactured and sold a whole series of such machines, trademarked Diskpack (See Section 9.4).

The preceding examples have shown the potential of the methodology using only two building blocks. Some additional examples are given in the problems listed in Section 6.5 and at the end of this chapter. The others are left as a challenge to the readers. Uncovering a novel design solution hidden among the multitude of alternatives offers a worthy experience in what can be termed ''the joy of design.''

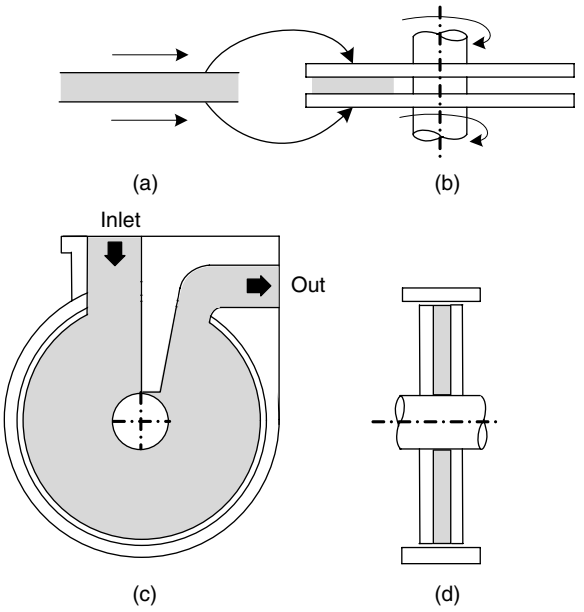

Fig. E6.7 The synthesis of the co-rotating-disk pump. (a) The building block; (b) two co-rotating disks form the moving planes; (c) front view of the processor showing the inlet and outlet ports separated by the channel block; (d) side view of the pump.

6.3 THE SINGLE SCREW EXTRUDER PUMP

In this section we derive a simple mathematical model for the single screw pump. In such a model, we seek relationships between performance and operating variables with the geometrical variables as parameters.

The single screw configuration has held its ground for over 125 years as the simplest and most useful geometrical configuration for processing plastics. In fact, the bulk of plastics are processed using an SSE, shown schematically in Fig. 6.5, at least once in their journey from raw material to finished product. A detailed treatment of single screw extrusion is given by Tadmor and Klein (17).

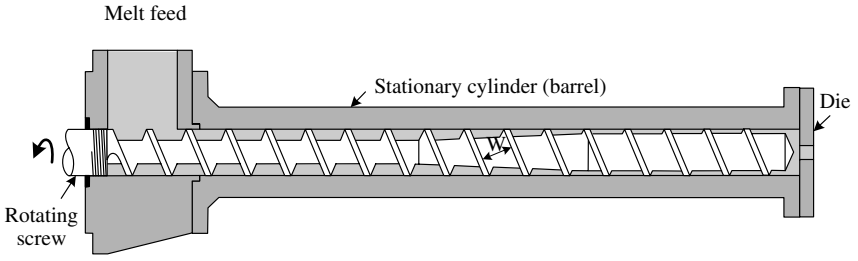

Fig. 6.5 Schematic view of an SSE. Its main components are a rotating screw within a stationary barrel. Polymer is fed through an inlet port and leaves the machine through a closure equipped with a die at the discharge end. Not shown in the figure are the electric motor drive and gear reducer for adjusting the rotational speed.

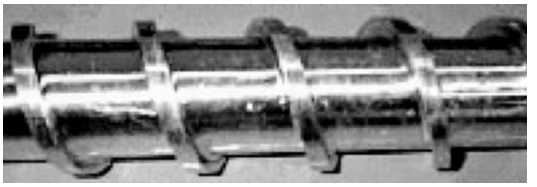

Fig. 6.6 A single-flighted square-pitched screw.

Not only is the single screw a very efficient pump but, as we saw in Chapter 4, it also conveys particulate solids well, and by virtue of its geometry it triggers and maintains the elegant *drag-removal melting mechanism* (see Section 5.7). It operates smoothly and conveniently with partially filled screws for venting (see Problem 6.9) and having a narrow residence time distribution, it enables processing of temperature-sensitive materials. It is a good extensive distributive mixer, though of course being close to plug flow, it lacks back mixing,[3] and contrary to common wisdom, it can also be designed for dispersive mixing (2).

The single screw as shown in Figs. 6.6 and 6.7 is a relatively simple geometrical configuration that is easy to manufacture, and therefore relatively inexpensive. Thus multiple screws can be retained with a single machine for different applications.

Geometry

Single screw extruders range in size from as small as 2 cm to as large as 75 cm in diameter, with axial length L to diameter D (taken at the tip of flight) ratios of 24 to 26, although occasionally we find extruders with L/D ratios as high as 40 or as low as 8. The latter are generally either rubber extruders or early[4] thermoplastic extruders. Between the tip of the

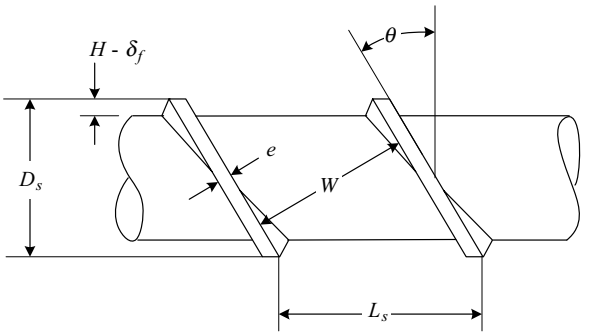

Fig. 6.7 Geometry of a square-pitched single-flighted screw.

3. Albert Aly Kaufman, one of the pioneers of extrusion, who established the celebrated Prodex Extruder Manufacturing Company, used to say ''What goes in comes out. Don't expect the screw to even-out non-uniform feeding of additives. It can't.''

4. The extruders used for rubber do not require the length of those used for plastics, because they do not need as long a melting section as plastics do. When the plastics industry adopted the rubber machinery, it imitated the rubber extruder design, but as demands for output and quality mounted, the length-to-diameter ratio of the extruder grew over time, until it leveled off at current values.

flight of the screw and the inner surface of the barrel D_b, there is a small radial clearance δ_f of the order of 0.1–0.3% of D_b. Polymer melt fills this gap and acts as a lubricant, preventing metal-to-metal contact. The diameter of the screw at the tip of the flights is $D_s = D_b - 2\delta_f$. The axial distance of one full turn of the flight is called the *lead* L_s.

Most screws of SSEs are single flighted, with $L_s = D_s$, referred to as *square-pitched screws.* The radial distance between the root of the screw and the barrel surface is the *channel depth*, H. The main design variable of screws is the *channel depth profile* that is $H(z)$, where z is the helical, down-channel direction, namely, the direction of net flow of the material. The angle formed between the flight and the plane normal to the axis is called the *helix angle*, θ, which, as is evident from Fig. 6.8, is related to lead and diameter

$$\tan\theta = \frac{L_s}{\pi D} \tag{6.3-1}$$

The value of the helix angle is therefore a function of the diameter. At the tip of the flight it is smaller than at the root of the screw. A square-pitched screw, neglecting the flight clearance, has a helix angle of 17.65° ($\tan\theta = 1/\pi$) at the flight tip.

The width of the channel W is the perpendicular distance between the flights, and as shown in Fig. 6.8, is

$$W = L_s \cos\theta - e \tag{6.3-2}$$

where e is the flight width. Clearly, since θ is a function of radial distance, so is W. Finally, the helical distance along the channel z is related to the axial distance l

$$z = \frac{l}{\sin\theta} \tag{6.3-3}$$

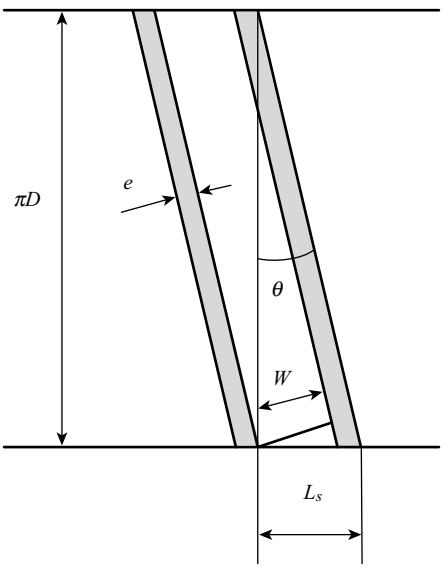

Fig. 6.8 The geometry of an unwound channel. This geometry is obtained by "painting" with ink the tips of the flights and rolling them one full turn on a sheet of paper. The track left by the flights is shown in the figure.

The Isothermal Newtonian "Standard" Mathematical Pumping Model

The mathematical model of isothermal flow of a Newtonian fluid in shallow-screw channels results in a simple design equation, which gives excellent insight into the flow mechanism and is very useful for first-order calculations. This model serves as the classic *pumping model* for single screw extrusion.

We commence its development by reversing the conceptual synthesis process. The space between a tightly fitting screw and the barrel is a helical channel. We unwind the channel from the screw and lay it on a flat surface. The result is a shallow rectangular straight channel, as in Fig 6.9.

The barrel surface becomes a flat plate covering the channel and moving at constant velocity of V_b at an angle θ_b to the down channel direction

$$V_b = \pi N D_b \tag{6.3-4}$$

where N is the frequency of rotation. The surface velocity of the barrel can be decomposed into down-channel and cross-channel components, given, respectively, by

$$V_{bz} = V_b \cos\theta_b \tag{6.3-5}$$

and

$$V_{bx} = V_b \sin\theta_b \tag{6.3-6}$$

The former drags the polymer melt toward the exit, whereas the latter induces cross-channel mixing.

Comparing the present flow configuration to that in Example 2.5 of flow between two infinite parallel plates in relative motion, we note two important differences. First, the flow in the down-channel z direction is two-dimensional due to the stationary side walls created by the flight [i.e., $v_z(x, y)$], and the barrel surface has a velocity component in the x direction that results in a circulatory flow in the cross-channel direction.

The simplifying assumptions for solving this flow problem are the same as those used in Example 2.5 for parallel plate flow, namely, we assume the flow to be an incompressible,

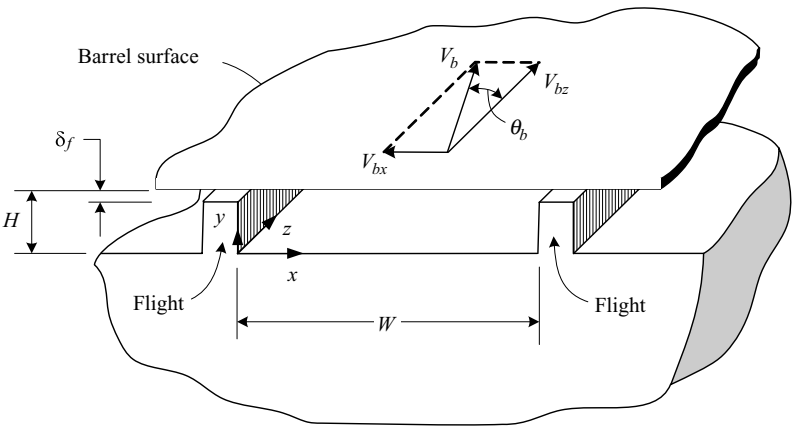

Fig. 6.9 Geometry of the unwound rectangular channel.

steady, isothermal, fully developed flow of a Newtonian fluid. The three components of the Navier–Stokes equation in rectangular coordinates defined in Fig. 6.9 reduce to

$$\rho\left(v_x\frac{\partial v_x}{\partial x}+v_y\frac{\partial v_x}{\partial y}\right)=-\frac{\partial P}{\partial x}+\mu\left(\frac{\partial^2 v_x}{\partial x^2}+\frac{\partial^2 v_x}{\partial y^2}\right) \tag{6.3-7}$$

$$\rho\left(v_x\frac{\partial v_y}{\partial x}+v_y\frac{\partial v_y}{\partial y}\right)=-\frac{\partial P}{\partial y}+\mu\left(\frac{\partial^2 v_y}{\partial x^2}+\frac{\partial^2 v_y}{\partial y^2}\right) \tag{6.3-8}$$

$$\rho\left(v_x\frac{\partial v_z}{\partial x}+v_y\frac{\partial v_z}{\partial y}\right)=-\frac{\partial P}{\partial z}+\mu\left(\frac{\partial^2 v_z}{\partial x^2}+\frac{\partial^2 v_z}{\partial y^2}\right) \tag{6.3-9}$$

where ρ is the density of the melt. In these equations the velocity components are not functions of z, since the flow is fully developed. It is further assumed that the flow in the cross-channel direction is also fully developed. This is a good approximation for shallow channels, except in the close neighborhood of the flights. Therefore, $\partial v_x/\partial x$, $\partial v_y/\partial x$, and $\partial v_z/\partial x$ vanish, and with these assumptions we obtain from the equation of continuity that $\partial v_y/\partial y = 0$, and consequently that $v_y = 0$. Equation 6.3-8 thus reduces to $\partial P/\partial y = 0$, implying that the pressure is a function of only x and z. Therefore, Eq. 6.3-7 reduces to

$$\frac{\partial P}{\partial x}=\mu\frac{\partial^2 v_x}{\partial y^2} \tag{6.3-10}$$

In Eq. 6.3-9 the left-hand side represents acceleration terms, which in the case of slow motion of a viscous fluid, will be much smaller than the terms representing the viscous forces on the right-hand side. In a typical flow situation in extruders, the ratio of the inertia to viscous forces is of the order of 10^{-5} (17a). Thus Eq. 6.3-9 reduces to

$$\frac{\partial P}{\partial z}=\mu\left(\frac{\partial^2 v_z}{\partial x^2}+\frac{\partial^2 v_z}{\partial y^2}\right) \tag{6.3-11}$$

Returning to Eq. 6.3-10, it is clear that the right-hand side is a function of y only, whereas, the left-hand side is a function only of x and z. Since neither side is dependent on the variable of the other, both must equal a constant, and Eq. 6.3-10 can be integrated to give

$$v_x=\frac{y^2}{2\mu}\left(\frac{\partial P}{\partial x}\right)+C_1 y+C_2 \tag{6.3-12}$$

The integration of constants C_1 and C_2 is evaluated from the boundary conditions $v_x(0) = 0$ and $v_x(H) = -V_{bx}$. Substituting these boundary conditions into Eq. 6.3-12 yields the cross-channel velocity profile

$$u_x=-\xi+\xi(\xi-1)\left(\frac{H^2}{2\mu V_{bx}}\frac{\partial P}{\partial x}\right) \tag{6.3-13}$$

where $u_x = v_x/V_{bx}$ and $\xi = y/H$. This equation correctly indicates that the cross-channel velocity profile depends on the cross-channel pressure gradient. But neglecting leakage flow, the net cross-channel flow rate is zero

$$\int_0^1 u_x\, d\xi = 0 \tag{6.3-14}$$

which, subsequent to substituting Eq. 6.3-13 and integration, enables us to express the pressure gradient in terms of the other variables as follows

$$\frac{\partial P}{\partial x} = -6\mu \frac{V_{bx}}{H^2} = -6\mu \frac{\pi N D_b \sin \theta_b}{H^2} \tag{6.3-15}$$

Thus we observe that the cross-channel gradient is proportional to screw speed and barrel diameter, and inversely proportional to the square of the channel depth. By substituting Eq. 6.3-15 into Eq. 6.3-13, we obtain the cross-channel velocity profile

$$u_x = \xi(2 - 3\xi) \tag{6.3-16}$$

shown in Fig. 6.10.

We note that the melt circulates around a plane located at exactly two-thirds of the channel height. A fluid particle in the upper one-third of the channel will move in the negative x direction at the velocity determined by its y position. Then, as the particle approaches the flight, it turns around and will move in the positive x direction at location y^*. The relationship between y and y^* can be obtained by a simple mass balance. We shall return to this subject and its implication in Chapter 7 when discussing extensive mixing in screw extruders.

The velocity profile just derived has been repeatedly verified experimentally (17b). Deviation from it occurs only in the close neighborhood of the flights [at $x < H/2$ or $x > (W - H/2)$], where the fluid acquires $v_y(x, y)$ components.

A full analytical solution of the cross channel flow $v_x(x, y)$ and $v_y(x, y)$, for an incompressible, isothermal Newtonian fluid, was presented recently by Kaufman (18), in his study of Renyi entropies (Section 7.4) for characterizing advection and mixing in screw channels. The velocity profiles are expressed in terms of infinite series similar in form to Eq. 6.3-17 below. The resulting vector field for a channel with an aspect ratio of 5 is shown

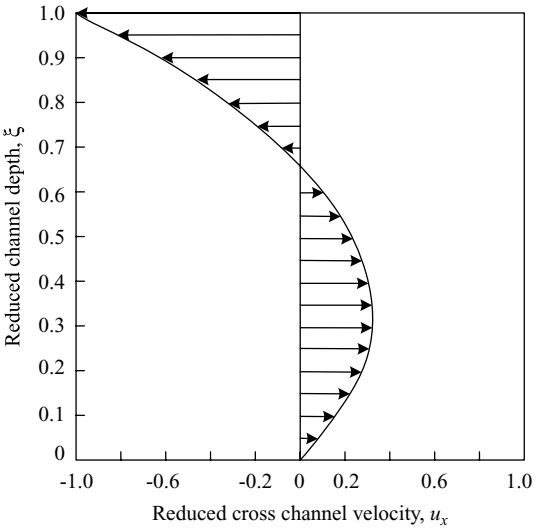

Fig. 6.10 Cross-channel velocity profile from Eq. 6.3-16. Note that melt circulates around a plane located at exactly two-thirds of the height.

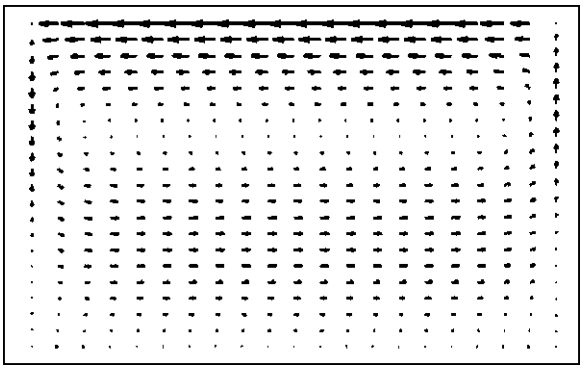

Fig. 6.11 Vector field of the cross-channel flow of an incompressible isothermal Newtonian fluid in a channel with an aspect ratio of 5. [Reprinted by the permission from M. Kaufman, "Advection and Mixing in Single Screw Extruder—An Analytic Model," *The AIChE Annu. Tech. Conf. Meeting Proc.*, San Francisco (2003).]

in Fig. 6.11. We note the stagnant region in the lower corners and at two-thirds of the height. The side wall effects are evident up to a distance of about $H/2$.

In the down-channel direction, the velocity profile is obtained by solving the partial differential equation (Eq. 6.3-11). It can be shown (17a) that the pressure gradient $\partial P/\partial z$ is constant (although P is a function of both x and z), which makes the solution, where the boundary conditions are $v_z(x,0) = 0$, $v_z(x,H) = V_{bz}$, $v_z(0,y)$, and $v_z(W,y) = 0$, rather straightforward.

Pure pressure flow was first formulated and solved by Joseph Boussinesq in 1868, and combined pressure and drag flow in 1922 by Rowell and Finlayson (19) in the first mathematical model of screw-type viscous pumps. The detailed solution by the method of separation of variables is given elsewhere (17c), and the resulting velocity profile is given by

$$u_z = \frac{4}{\pi}\sum_{i=1,3,5}^{\infty}\frac{\sinh(i\pi h\xi)}{i\sinh(i\pi h)}\sin(i\pi\chi) + \left(\frac{H^2}{2\mu V_{bz}}\frac{\partial P}{\partial z}\right) \times \left[\xi^2 - \xi + \frac{8}{\pi^3}\sum_{i=1,3,5}^{\infty}\frac{\cosh[i\pi(\chi - 0.5)/h]}{i^3\cosh(i\pi/2h)}\sin(i\pi\xi)\right] \tag{6.3-17}$$

where $u_z = v_z/V_{bz}$, $\chi = x/W$, and $h = H/W$.

Figure 6.12 depicts the velocity distribution of pure drag flow ($\partial P/\partial z = 0$) as constant velocity curves at different *H/W* ratios. We note the increasing significance of the restraining effect of the flight with increasing *H/W* ratios.

The flow rate through the extruder, the pressure profile along the screw, and the power consumption are the main quantities of interest for design, and these are calculated nextfrom the velocity profile. The net volumetric flow rate Q is obtained by integrating Eq. 6.3-17 across the channel

$$Q = WHV_{bz}\int_0^1\int_0^1 u_z\, d\xi\, d\chi \tag{6.3-18}$$

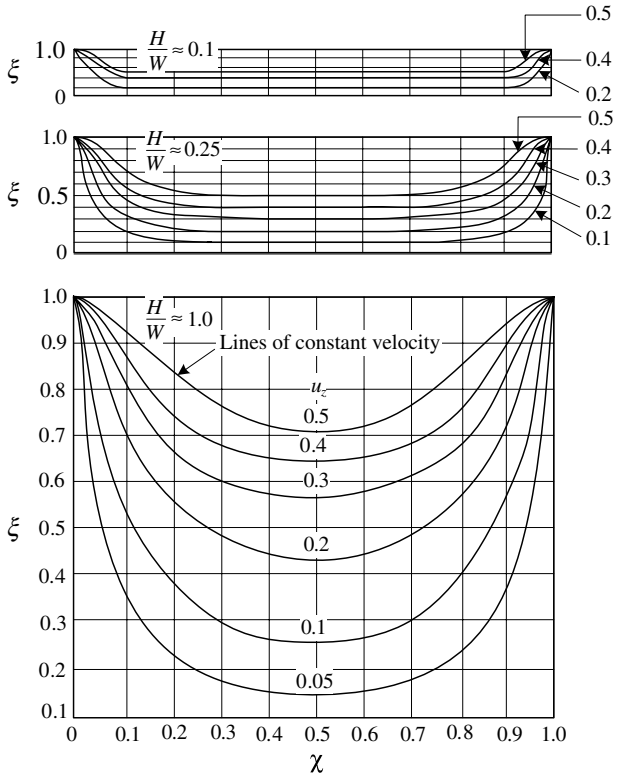

Fig. 6.12 Down-channel velocity distribution for pure drag flow from Eq. 6.3.17 for various *H/W* ratios. [Reprinted by permission from E. C. Bernhardt, Ed., *Processing of Thermoplastic Materials*, Reinhold, New York, p. 290 (1959).]

The integration of the infinite series in Eq. 6.3-17 is permissible termwise, because the series is uniformly converging. The results are given by

$$Q = \frac{V_{bz}WH}{2}F_d + \frac{WH^3}{12\mu}\left(-\frac{\partial P}{\partial z}\right)F_p \tag{6.3-19}$$

where F_d and F_p are "shape factors" for drag and pressure flow, respectively. They assume values that are smaller than 1 and represent the restricting effect of the flight on flow between infinite parallel plates. They are given by

$$F_d = \frac{16W}{\pi^3 H}\sum_{i=1,3,5}^{\infty}\frac{1}{i^3}\tanh\left(\frac{i\pi H}{2W}\right) \tag{6.3-20}$$

$$F_p = 1 - \frac{192H}{\pi^5 W}\sum_{i=1,3,5}^{\infty}\frac{1}{i^5}\tanh\left(\frac{i\pi W}{H}\right) \tag{6.3-21}$$

Note that the shape factors plotted in Fig. 6.13 are a function of only the *H/W* ratio. The effect of the flight on the pressure flow is stronger than that on drag flow. When the ratio *H/W* diminishes, both approach unity. In this case, Eq. 6.3-19 reduces to the simplest possible model for pumping in screw extruders, that is, isothermal flow of a Newtonian fluid between two parallel plates.

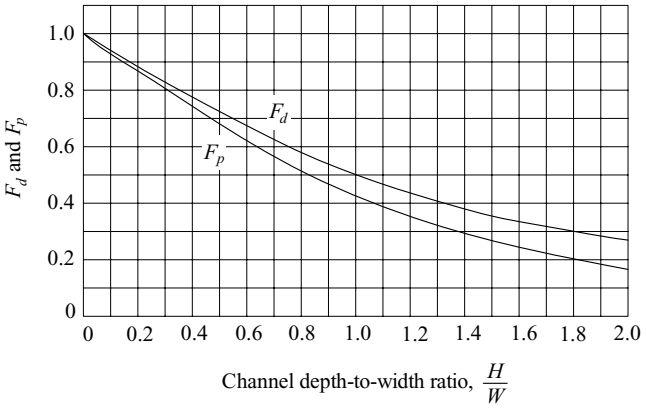

Fig. 6.13 Shape factors for drag and pressure flows from Eqs. 6.3-20 and 6.3-21.

Equations 6.3-19 is the well-known isothermal Newtonian extrusion theory. Since it was obtained by the solution of a linear differential equation, it is composed of two *independent* terms, the first representing the contribution of drag flow Q_d, and the second, the pressure flow, Q_p. The net flow rate is the linear superposition of the two.

$$Q = Q_d + Q_p \tag{6.3-22}$$

We note that if the pressure gradient is positive (pressure rises in the direction of flow), the pressure-flow term is negative and $Q < Q_d$, whereas if pressure drops in the direction of flow, $Q > Q_d$. The ratio of pressure to drag flow is obtained from Eq. 6.3-19

$$\frac{Q_p}{Q_d} = -\frac{H^2}{6\mu V_{bz}}\left(\frac{\partial P}{\partial z}\right)\frac{F_p}{F_d} \tag{6.3-23}$$

A negative pressure flow for the positive pressure gradient led to the term *back flow*, namely, that the pressure drives the fluid opposite to the direction of the net flow. This term led to the erroneous concept that actual flow toward the feed end occurs in some part of the channel. However, it is important to note that *under no condition* does the melt flow backward along the screw axis.[5] Fluid particles may move backward along the z direction, but not along the axial direction, l. Once a fluid particle passes a given axial location, it cannot cross this plane backward. This is evident from the velocity profile in the axial direction:

$$v_l = v_x \cos\theta + v_z \sin\theta \tag{6.3-24}$$

Substituting Eqs. 6.3-16 and 6.3-17 (which for very shallow channels simplify to the velocity profile between infinite parallel plates given in Eq. E2.5-8 with $V_0 = V_{bz}$, and $(P_L - P_0)/L = \partial P/\partial z$ into Eq.6.3-24, using Eq. 6.3-23, and assuming that $\theta_b \cong \theta$, we get

$$u_l = 3\xi(1-\xi)\left(1 + \frac{Q_p}{Q_d}\right)\sin\theta\cos\theta \tag{6.3-25}$$

5. Except if a head pressure higher than the pressure generated by the screw is imposed at the discharge end (e.g., by another extruder in head-on configuration).

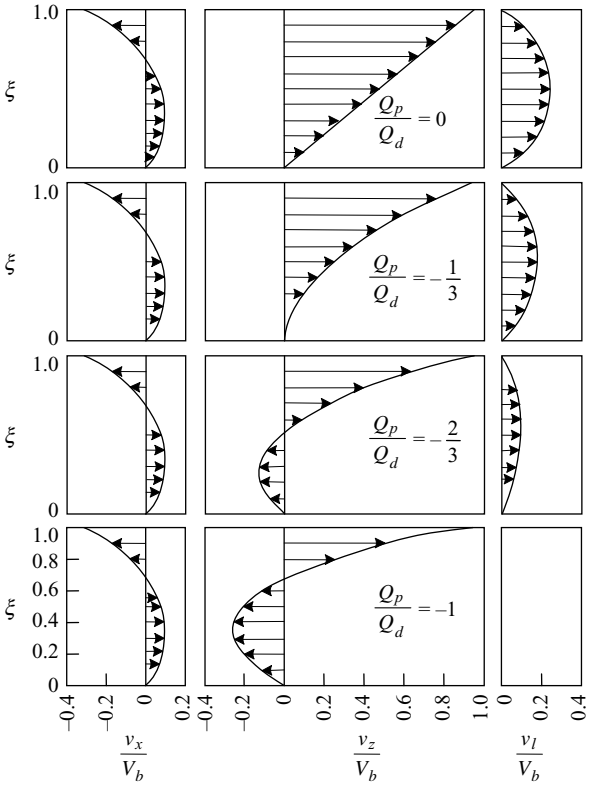

Fig. 6.14 Cross-channel, down-channel, and axial velocity profiles for various Q_p/Q_d values, in shallow square-pitched screws [Reproduced by permission from J. M. McKelvey, *Polymer Processing*, Wiley, New York, 1962.]

where $u_l = v_l/V_b$. We observe that this equation implies that for helix angles between 0 and $\pi/2$, u_l is always positive. In other words, in the axial direction there cannot be any backflow. Moreover, the shape of the velocity profile is parabolic with the maximum velocity at midplane $\xi = 0.5$. The value at the maximum is determined by the pressure to drag flow ratio. For closed discharge $(Q_d + Q_p = 0)$, u_l vanishes everywhere. The maximum velocity increases with reduction in pressure flow until it reaches a maximum value for pure drag flow

$$u_{l,\max} = \frac{3}{4}\sin\theta\cos\theta \tag{6.3-26}$$

The velocity at any ξ as indicated by Eq. 6.3-25 is a function of the helix angle θ and attains a maximum value at $\theta = \pi/4$. Hence this is also the optimum helix angle for maximum flow rate.[6] Figure 6.14 shows cross- and down-channel and axial velocity profiles for various pressure-to-drag flow ratios. From the velocity profiles, we can deduce the path of the fluid particles in the channel, as depicted in Fig. 6.15.

6. In spite of this, screws are normally square pitched with a 17.6° helix angle. The reason is that the optimum is rather flat and the gain in flow rate not that significant. Moreover, a 45° helix will yield a more sensitive screw to fluctuating head pressure, and finally, the other elementary steps are not necessarily optimal at 45°.

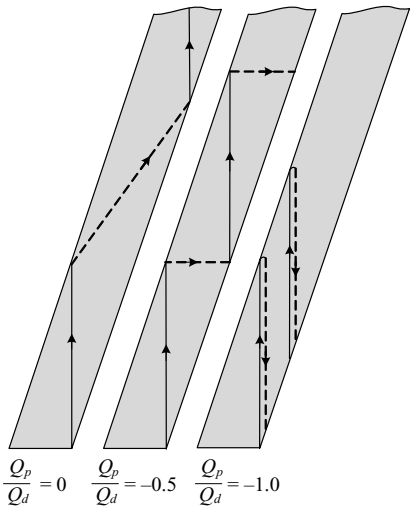

Fig. 6.15 The path of a fluid particle in the screw channel for $Q_p/Q_d = 0$, $Q_p/Q_d = -0.5$, $Q_p/Q_d = -1.0$. Solid lines show the path of the fluid in the upper portion of the channel at a selected value of $\xi = 0.9$, and the broken lines show the path of the same fluid particle in the lower portion of the channel at the corresponding $\xi^* = 0.35$.

At closed discharge conditions when the net flow rate or throughput is zero $(Q_p/Q_d = -1)$, the fluid particle circulates at a fixed axial plane by advancing and retreating in the z and x directions. As the particles come close to the flight, they acquire velocity in the y direction (neglected in this model) and turn around. Under closed discharge conditions we also note that fluid particles at $\xi = 2/3$ are stationary. As the throughput increases, the loops open and the fluid particles travel along a flattened helical path. The closer the flow is to pure drag flow, the more open the loops of the helix are. Thus polymer particles travel in a path that is a flat helix within a helical channel.

So far we have neglected the effect of the flight clearance. As small as the clearance is, polymer melt is being dragged across the clearance by the barrel surface and the pressure drop may pump melt across the flight width. This creates a continuous leakage flow from downstream locations to (one turn back) upstream locations, reducing net flow rate.

It is very difficult to accurately evaluate the effect of leakage flow across the flight in a real situation with significant non-Newtonian and nonisothermal effects included. At the very high shear rates prevailing in the clearance, these might be quite significant, and even tax sophisticated finite element methods (FEMs). But for the isothermal Newtonian model, a useful approximate solution has been derived (17d). The analysis leads to a modified design equation (Eq. 6.3-19):

$$Q = \frac{V_{bz} W (H - \delta_f)}{2} F_d + \frac{W H^3}{12\mu} \left(-\frac{\partial P}{\partial z} \right) F_p (1 + f_L) \tag{6.3-27}$$

where δ_f is the radial flight clearance and f_L is given by

$$f_L = \left(\frac{\delta_f}{H} \right)^3 \frac{e}{W} \frac{\mu}{\mu_f} + \frac{\left(1 + \dfrac{e}{W}\right) \left[\dfrac{1 + e/W}{\tan^2 \theta} + \dfrac{6\mu V_{bz} (H - \delta_f)}{H^3 (\partial P/\partial z)} \right]}{1 + \dfrac{\mu}{\mu_f} \left(\dfrac{H}{\delta_f} \right)^3 \dfrac{e}{W}} \tag{6.3-28}$$

where μ_f is the viscosity in the flight clearance and μ is the viscosity in the channel. This is an attempt to approximately account for non-Newtonian effects by evaluating the viscosity at the prevailing shear rates in the clearance. For Newtonian fluids the two are equal.

Equation 6.3-28 suggests that drag flow is always reduced by the flight clearance by a factor of $1 - \delta/H$. The effect of pressure flow is more complicated. In the special case of pure drag flow ($\partial P/\partial z = 0$), the cross-channel pressure gradient creates higher pressure at the pushing flight than one turn back at the trailing flight, causing pressure leakage backflow across the flight. This leakage flow increases if pressure rises in the down-channel direction, and decreases if pressure drops in the down-channel direction over that one turn segment.

We have seen how the screw extruder pump is *synthesized* from a simple building block of two parallel plates in relative motion. We have also seen how the *analysis* of the screw extruder leads in first approximation back to the shallow channel parallel plate model. We carried out the analysis for isothermal flow of a Newtonian fluid, reaching a model (Eq. 6.3-27) that is satisfactory for gaining a deeper insight into the pressurization and flow mechanisms in the screw extruder, and also for first-order approximations of the pumping performance of screw extruders.

The screw extruder is equipped with a die, and the flow rate of the extruder as well as the pressure rise at a given screw speed are dependent on both, as shown in Fig. 6.16. The screw characteristic line at a given screw speed is a straight line (for isothermal Newtonian fluids). This line crosses the abscissa at open discharge (drag flow rate) value and the ordinate at closed discharge condition. The die characteristic is linearly proportional to the pressure drop across the die. The operating point, that is, the flow rate and pressure value at which the system will operate, is the cross-point between the two characteristic lines, when the pressure rise over the screw equals the pressure drop over the die.

The classic extrusion model gives insight into the screw extrusion mechanism and first-order estimates. For more accurate design equations, it is necessary to eliminate a long series of simplifying assumptions. These, in the order of significance are (a) the shear rate-dependent non-Newtonian viscosity; (b) nonisothermal effects from both conduction and viscous dissipation; and (c) geometrical factors such as curvature effects. Each of these

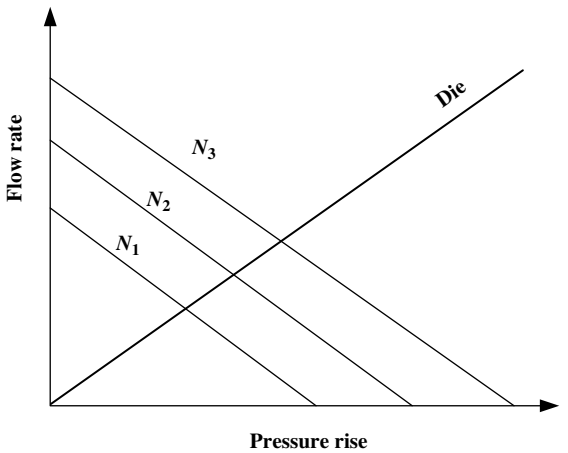

Fig. 6.16 Screw characteristic lines at three screw speeds $N_1 < N_2 < N_3$ and die characteristic line.

introduces significant mathematical complications. Thus, whereas it is possible to derive analytical parallel-plate extrusion models for an isothermal non-Newtonian fluid (e.g., using Power Law or Ellis fluid models), it is impossible to have an analytical solution for channel flows and certainly for nonisothermal flows.

Even the parallel plate non-Newtonian isothermal model is no longer a linear superposition of drag and pressure flow, but a more complex combination of the variables. Nonisothermal flows by and large require numerical solutions. The ultimate model would be a model for nonisothermal flow of a non-Newtonian fluid in the actual helical channel, including leakage flow and accounting for boundary conditions (e.g., barrel temperature and screw temperature profiles,[7] and possible slip on solid surfaces). Recent advances in computerized fluid mechanics (CFM) using FEMs indeed enable such solutions. However, they may be time-consuming and expensive and also exhibit numerical difficulties with real melts that are not only shear thinning but also viscoelastic fluids, in situations of sudden changes in geometry, such as, for example, at the entrance and exit to flight clearance, and with circulating flows as those occurring in the screw channel.

Historically, before CFM or even FEMs were available, two complementary approaches were used to tackle this problem. On the one hand, there was a continuing effort to solve increasingly more realistic flow situations analytically or numerically. This approach was taken by Griffith (20), Colwell and Nicholls (21), Pearson (22) Zamodits (23), Booy (24), Choo et al. (25), Nebrensky et al. (26), Hami and Pittman (27), Pearson (28), Pittman and Rashid (29), Bruker et al. (30), and others. On the other hand, ''approximate correction factors'' were derived using simple models, which could improve accuracy by accounting at least for the bulk part of the complexity. The ''shape factors'' in Eq. 6.3-27 can be viewed as correction factors accounting for the wall effect on the parallel-plate model. Thus, by comparing Couette and annular pressure flow with straight corresponding straight-channel flows, a ''curvature correction'' factor can be derived separately for drag and pressure flows (17e). Some nonisothermal correction factors and non-Newtonian correction factors can be similarly evaluated. These lumped-parameter stepwise models, discussed in Section 9.1, surprisingly agree reasonably well with experiments using minimal computational effort.

6.4 KNIFE AND ROLL COATING, CALENDERS, AND ROLL MILLS

Knife coating is shown schematically in Fig. 6.17, and roll coating, roll mills, and calenders are shown schematically in Fig. 6.18. These are devices that generate pressure on the basis of Building Blocks 3 and 4, namely, two nonparallel plates in relative or joint motion. The processing function of each device is made possible by the fact that these geometrical configurations can generate pressure. Thus they are not pumps per se, although two rolls can act as a continuous pump, as shown in Fig 6.18(d).

7. The correct barrel temperature to be used is the inner surface temperature. This is generally not known and a heat transfer problem in the barrel must be solved in conjunction with the flow model of the melt in the screw channel. Screw temperature is generally not controlled and it can be assumed to be roughly equal to the average melt temperature.

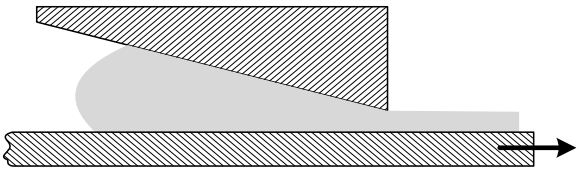

Fig. 6.17 Schematic representation of knife coating, based on building block 3.

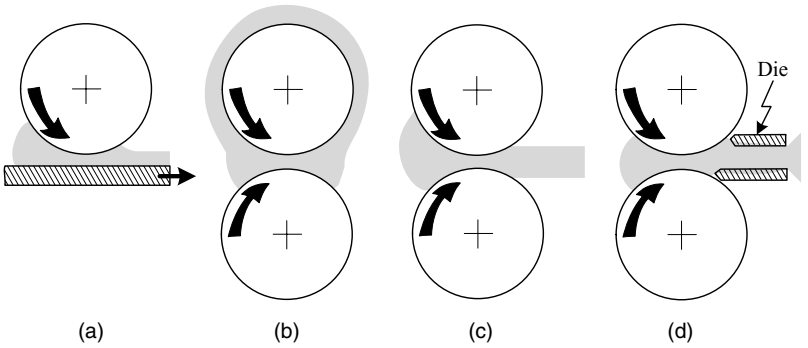

Fig. 6.18 Schematic representation of pressure generating devices based on building blocks 4: (a) roll coating; (b) roll mill; (c) calender; (d) twin roll extruder.

Non–parallel Plate Drag Flow

The flow configuration of building block 3, of two non-parallel plates in relative motion, shown in Fig. 6.19, was analyzed in detail in Example 2.8 using the lubrication approximation and the Reynolds equation. This flow configuration is not only relevant to knife coating and calendering, but to SSEs as well, because the screw channel normally has constant-tapered sections. As shown in Fig. 6.19, the gap between the plates of length L is H_0 and H_1 at the entrance and exit, respectively, and the upper plate moves at constant velocity V_0.

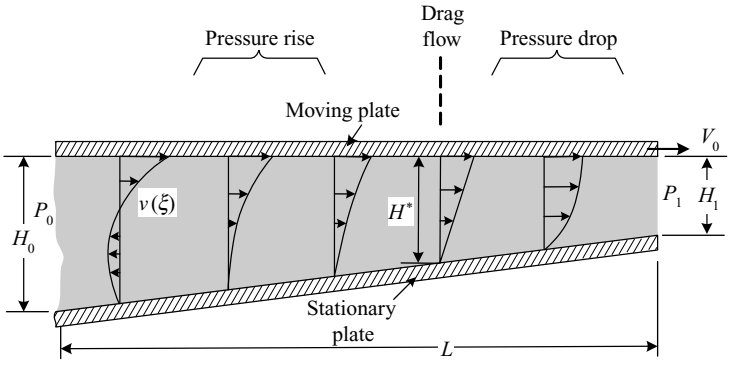

Fig. 6.19 Two non-parallel plates in relative motion, with schematic velocity profiles for a condition with equal entrance and exit pressure, in which case the pressure profile exhibits a maximum in the flow range.

As shown in Example 2.8, the pressure profile along the plates is given by

$$P = P_0 + \frac{6\mu L V_0}{H_0 H_1}\left[\frac{\zeta_0 - \zeta}{\zeta(\zeta_0 - 1)} - \left(\frac{q}{V_0 H_0}\right)\frac{\zeta_0^2 - \zeta^2}{\zeta^2(\zeta_0 - \zeta)}\right] \tag{6.4-1}$$

where P_0 is pressure at the entrance, $\zeta_0 = H/H_1$, $\zeta = H_0/H_1$, and q is the volumetric flow rate per unit width, which can be expressed in terms of the channel gap where pressure exhibits a maximum value, H^*

$$q = \frac{1}{2}V_0 H^* \tag{6.4-2}$$

The pressure profile thus depends on a number of variables: geometrical (H_0, H_1, and L), operational (q, V_0), and physical property variables, and the viscosity μ. The maximum pressure that can be attained is $\zeta = 1$ ($z = L$) at closed discharge condition ($q = 0$)

$$P_{\max} = P_0 + \frac{6\mu V_0 L}{H_0 H_1} \tag{6.4-3}$$

By examining Eq. 6.4-1, as pointed out in Example 2.8, we see that at equal entrance and discharge pressures, the pressure profile exhibits a maximum at $H^* = 2H_0/(1 + \zeta_0)$, or at $z/L = \zeta_0(1 + \zeta_0)$, which for $\zeta_0 = 2$ is two-third of the way down the channel. This result focuses attention on the important difference between parallel plate and non-parallel plate geometries. In the former, equal inlet and outlet pressures imply no pressurization and pure drag flow; in the latter it implies the existence of a maximum in pressure profile. Indeed, as we saw in Section 2.11, Example 2.9, this pressurization mechanism forms the foundation of hydrodynamic lubrication.

The gap between the plates does not have to change gradually; it can be an abrupt change, as shown in Fig. 6.20, with a pressure profile rising linearly and then dropping linearly, with the maximum value at the step decrease in height. Slider pads are used for hydrodynamic lubrication because they have good loading capacity. Westover (31) converted this pressurization method into a continuous rotary slider pad pump, as shown in Fig. 6.21.

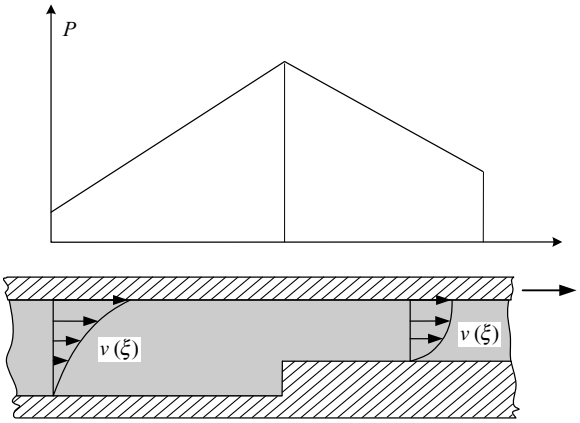

Fig. 6.20 Schematic representation of a slider pad.

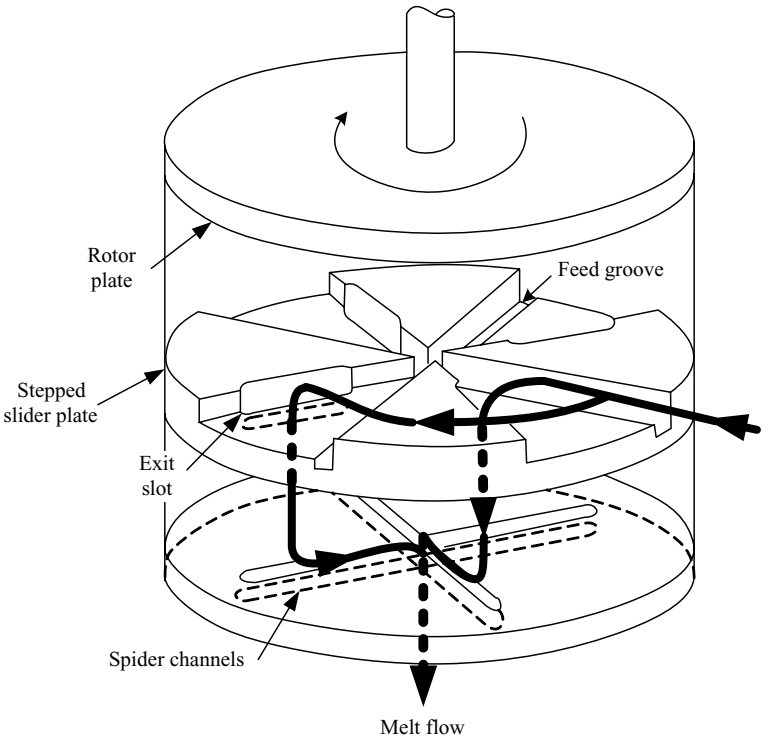

Fig. 6.21 A rotary-sector slider pad extruder. [Reprinted by permission from R. F. Westover, ''A Hydrodynamic Screwless Extruder'' *Soc. Plastics Eng. J.*, 1473 (1962).]

Finally, as pointed out earlier, extruder screws have tapered channel sections. The various shaped pressure profiles that can be obtained in simple non–parallel plate geometry explain the experimentally observed pressure profiles in screw extruders. For example, in a common metering screw (with a constant channel depth feed section, followed by a tapered section and a constant channel depth metering section), under normal conditions the pressure profile exhibits a maximum in the tapered section with the pressure dropping in the metering section to the die pressure.

From Eq. 6.4-1, with $\zeta = 1$ we can obtain an expression for the flow rate in terms of the pressure drop over the tapered section given by

$$q = \frac{V_0 H_0}{2}\left(\frac{2}{1+\zeta_0}\right) + \frac{H_0^3}{12\mu}\left(\frac{P_0 - P_1}{L}\right)\left(\frac{2}{\zeta_0(1+\zeta_0)}\right) \tag{6.4-4}$$

For parallel plates, $\zeta_0 = 1$, this equation reduces to Eq. 6.3-19 with pressure *drop* replacing pressure *gradient*. Hence, the terms containing ζ_0 can be viewed as ''correction factors'' of the parallel plate model for tapered geometries.

Example 6.8 Knife Coating Consider a knife at angle to a substrate, which moves at velocity V_0 and being covered by a thin film coating of a viscous Newtonian liquid of thickness δ, as shown schematically in Fig. E6.8. Derive an expression for the film thickness δ.

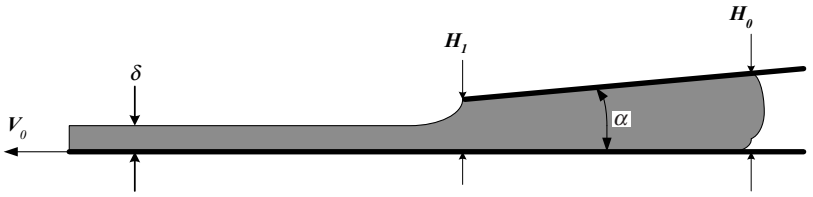

Fig. E6.8 An infinitely long substrate coated by a knife coater at angle α to it.

Solution We assume that Eq. 6.4-4 holds with $P_0 = P_1$ and $q = V_0\delta$, and it reduces to

$$\delta = \frac{H_0}{1+\zeta_0} = \frac{H_1}{1+1/\zeta_0}$$

where $\zeta_0 = H_0/H_1$. Clearly, for a knife placed parallel to the substrate, the thickness of the coating is one half of the gap, and the higher the taper the closer the thickness comes to the gap size at the exit point, which will be reached with a sharp-edge coating, with the knife perpendicular to the substrate.

Two Rotating Rolls: Roll Mills and Calenders

The two rotating roll geometry of roll-mills and calenders is an important application of the non-parallel plate pressurization concept with both plates moving, stemming from building block 4 in Figure 6.2. There are, however, some differences between the two cases. In roll mills the operation is generally a batch operation with the polymer forming a continuous blanket around one of the rolls and the two rolls generally rotating at different frequencies. In calenders, on the other hand, there is one pass between any set of two rolls, which occasionally are of different radii, and operate at different speeds. The purpose of the former is to melt and mix the polymer, whereas the aim of the latter is to shape a product. Hence, we discuss roll mills in more detail in Chapter 7, which deals with mixing, and in Chapter 15, which covers calendering. Nevertheless the nip flow in both cases is based on the same principle of pressurization, and thus it is addressed in this chapter.

Figure 6.22 depicts schematically the flow configuration. Two identical rolls of radii R rotate in opposite directions with frequency of rotation N. The minimum gap between the rolls is $2H_0$. We assume that the polymer is uniformly distributed laterally over the roll width W. At a certain axial (upstream) location $x = X_2$ ($X_2 < 0$), the rolls come into contact with the polymeric melt, and start "biting" onto it. At a certain axial (downstream) location $x = X_1$, the polymeric melt detaches itself from one of the rolls. Pressure, which is assumed to be atmospheric at X_2, rises with x and reaches a maximum upstream of the minimum gap location (recall the foregoing discussion on the pressure profile between non-parallel plates), then drops back to atmospheric pressure at X_1. The pressure thus generated between the rolls creates significant separating forces on the rolls. The location of points X_1 and X_2 depends on roll radius, gap clearance, and the total volume of polymer on the rolls in roll mills or the volumetric flow rate in calenders.

First we derive the simple Newtonian model following Gaskell's (32) and McKelvey's (33) models. The following assumptions are made: the flow is steady, laminar, and isothermal; the fluid is incompressible and Newtonian; there is no slip at the walls; the

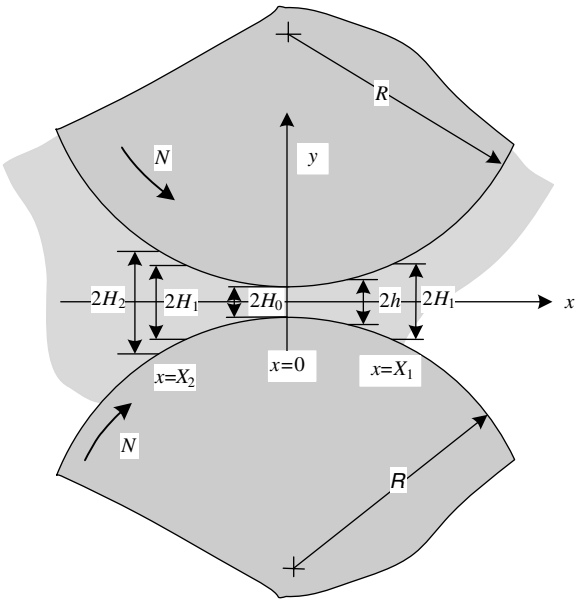

Fig. 6.22 The nip region of the two-roll geometry, with radii R. A rectangular coordinate system is placed at the midplane in the gap between the rolls connecting the two roll centers.

clearance-to-radius ratio is $h/R \ll 1$ throughout the region; in other words, we assume narrow gap flow with slowly varying gap separation, which enables us to invoke the lubrication approximation (which implies that the velocity profile at any location x with local gap separation $2h$ equals the velocity profile between two infinite parallel plates at a distance $2h$ apart, with pressure gradient and plate velocities equal to the local values between the rolls); finally, gravity forces are neglected and there is only one nonvanishing component $v(y)$. Hence, the equation of continuity and motion, respectively, reduce to

$$\frac{dv_x}{dx} = 0 \tag{6.4-5}$$

and

$$\frac{dP}{dx} = -\frac{\partial \tau_{yx}}{\partial y} = \mu \frac{\partial^2 v_x}{\partial y^2} \tag{6.4-6}$$

Equation 6.4-6 can be integrated twice without difficulty, because the pressure P is a function of x only. The boundary conditions are $v_x(\pm h) = U$, where U is the tangential velocity of the roll surface

$$U = 2\pi NR \tag{6.4-7}$$

The resulting velocity profile is

$$v_x = U + \frac{y^2 - h^2}{2\mu}\left(\frac{dP}{dx}\right) \tag{6.4-8}$$

Note that Eq.6.4-8 indicates that for a positive pressure gradient (i.e., pressure rises in the positive x direction), $v_x(0) < U$, and for a negative pressure gradient, $v_x(0) > U$.

The flow rate per unit width q is obtained by integrating Eq. 6.4-8 to give

$$q = 2\int_0^h v_x\, dy = 2h\left(U - \frac{h^2}{3\mu}\frac{dP}{dx}\right) \tag{6.4-9}$$

At steady state, q is constant and dependent on position x. To solve for the pressure profile, we require that the velocity be uniform at the exit $v_x(y) = U$. This requirement implies that $\tau_{yx} = 0$, and from Eq. 6.4-6 we conclude that the pressure gradient also vanishes at this point. Hence, the flow rate in Eq. 6.4-9 can be expressed in terms H_1 and U as

$$q = 2H_1U \tag{6.4-10}$$

Substituting Eq. 6.4-10 into Eq. 6.4-9, subsequent to some rearrangement, gives

$$\frac{dP}{dx} = \frac{3\mu}{H_1^2}\left(1 - \frac{H_1}{h}\right)\left(\frac{H_1}{h}\right)^2 \tag{6.4-11}$$

Equation 6.4-11 implies that the pressure gradient is zero not only at $x = X_1$ but also at $x = -X_1$, where h also equals H_1, and where, as we shall see later, the pressure profile exhibits maximum. The pressure profile is obtained by integrating Eq. 6.4-11 with the boundary condition $P(X_1) = 0$. First, however, we must find a functional relationship between h and x. From plane geometry we get the following relationship

$$h = H_0 + R - \sqrt{R^2 - x^2} \tag{6.4-12}$$

which can be simplified by expanding the $\sqrt{R^2 - x^2}$ using the binomial series and retaining only the first two terms. This results in

$$\frac{h}{H_0} = 1 + \rho^2 \tag{6.4-13}$$

where

$$\rho^2 = \frac{x^2}{2RH_0} \tag{6.4-14}$$

Integration of Eq. 6.4-11, subsequent to substituting Eqs. 6.4-13 and 6.4-14, gives the pressure profile

$$P = \frac{3\mu U}{4H_0}\sqrt{\frac{R}{2H_0}}\left\{\left[\frac{\rho^2 - 1 - 5\lambda^2 - 3\lambda^2\rho^2}{(1+\rho^2)^2}\right]\rho + \left(1 - 3\lambda^2\right)\tan^{-1}\rho + C(\lambda)\right\} \tag{6.4-15}$$

where

$$\lambda^2 = \frac{X_1^2}{2RH_0} \tag{6.4-16}$$

and the constant of integration $C(\lambda)$ is obtained by setting $P = 0$ at $\rho = \lambda$

$$C(\lambda) = \frac{(1 + 3\lambda^2)}{(1 + \lambda^2)}\lambda - (1 - 3\lambda^2)\tan^{-1}\lambda \tag{6.4-17}$$

McKelvey suggested the following approximation for $C(\lambda)$

$$C(\lambda) \cong 5\lambda^3 \tag{6.4-18}$$

The maximum pressure is obtained by substituting $\rho = -\lambda$ into Eq. 6.4-15

$$P_{\max} = \frac{3\mu U}{4H_0}\sqrt{\frac{R}{2H_0}}[2C(\lambda)] \cong \frac{15\mu U\lambda^3}{2H_0}\sqrt{\frac{R}{2H_0}} \tag{6.4-19}$$

Note that the maximum pressure is very sensitive to λ. An increase in λ brings about both a broadening of the pressure profile as well as an increase in the maximum value. This is demonstrated in Fig. 6.23 where $P/P_{\max,\lambda=1}$ is plotted versus ρ with λ as a parameter.

Results indicate that for any given λ, there is a particular upstream position at which the pressure drops to zero, which is denoted as X_2. This unique relationship between λ and X_2, obtained by setting $P = 0$ in Eq. 6.4-15, is plotted in Fig. 6.24 in terms of $\rho_2 = X_2\sqrt{2RH_0}$. Note that both ρ_2 and X_2 are negative. Finally, another property of the pressure profile is that at $x = 0$, the pressure equals exactly $P_{\max}/2$.

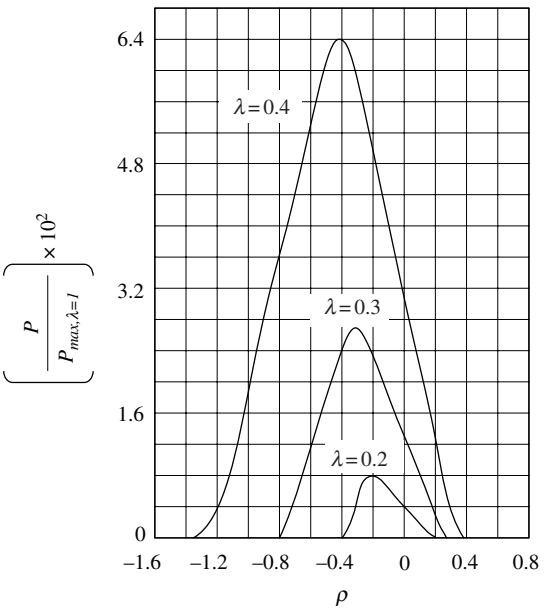

Fig. 6.23 Pressure profiles between rolls with λ as a parameter. [Reprinted by permission from J. M. McKelvey, *Polymer Processing*, Wiley, New York, 1962.]

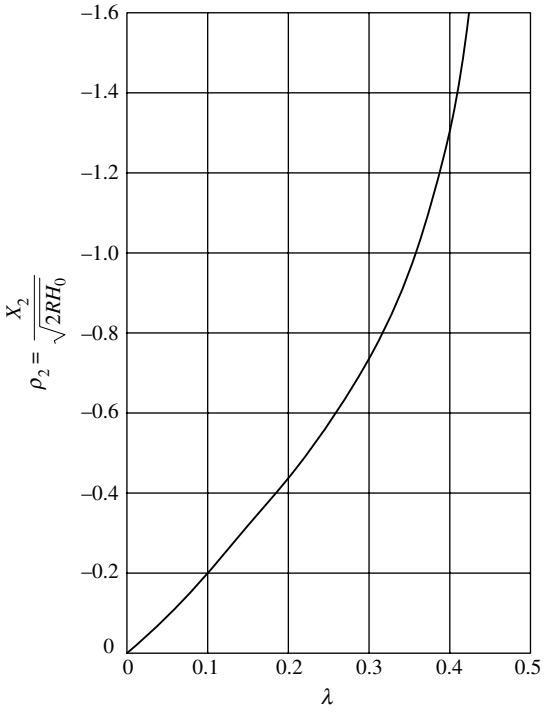

Fig. 6.24 Relationship between ρ_2, where the rolls "bite" onto the polymer (equivalent to X_2) and λ where the polymer detaches (equivalent to X_1). [Curve based on computation from G. Ehrmann and J. Vlachopoulos, *Rheol. Acta*, **14**, 761 (1975).]

The velocity profile is obtained by substituting Eq. 6.4-11 into Eq. 6.4-8, with the aid of Eqs. 6.4-13, 6.4-14, and 6.4-16

$$u_x = 1 + \frac{3}{2}\frac{(1-\xi^2)(\lambda^2-\rho^2)}{(1+\rho^2)} \tag{6.4-20}$$

where $u_x = v_x/U$ and $\xi = y/H$. Figure 6.25 shows velocity profiles for $\lambda^2 = 0.1$.

Equation 6.4-20 indicates that at a certain axial location ρ^* at $\xi = 0$, a stagnation point may occur $(v_x(0) = 0)$

$$\rho^* = -\sqrt{2+3\lambda^2} \tag{6.4-21}$$

For $\lambda = 0.425$, the stagnation point is at the contact point; hence, for $\lambda > 0.425$a circulatory flow develops in the entrance region.

The rate of strain and stress distributions can now be obtained from the velocity profile, which together with Eq. 6.4-13, gives:

$$\dot{\gamma}_{yx}(\xi) = \frac{3U(\rho^2-\lambda^2)}{H_0(1+\rho^2)^2}\xi \tag{6.4-22}$$

and

$$\tau_{yx}(\xi) = \frac{3\mu U(\lambda^2-\rho^2)}{H_0(1+\rho^2)^2}\xi \tag{6.4-23}$$

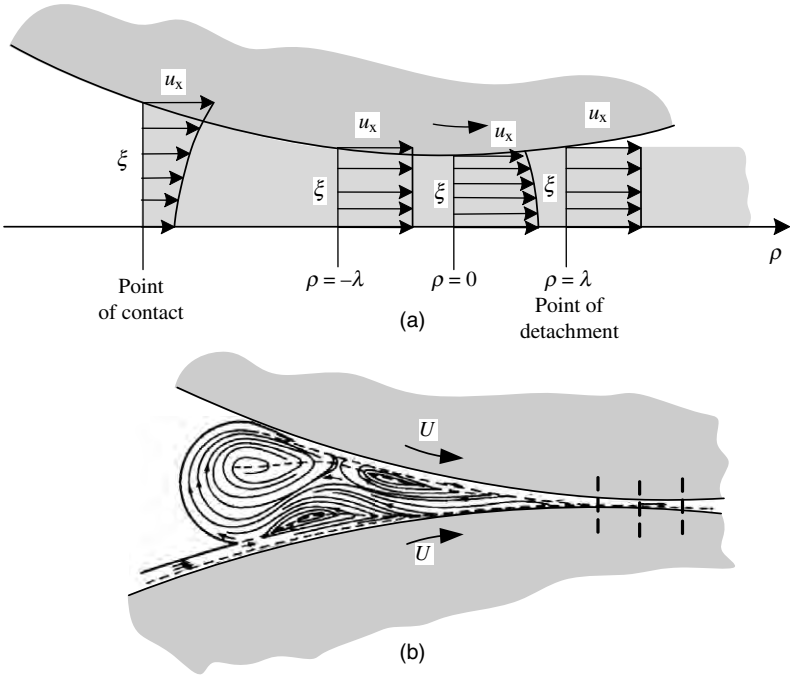

Fig. 6.25 (a) Velocity profiles between rolls for $\lambda^2 = 0.1$ from Eq. 6.4-25. At $\rho = \pm\lambda$ velocity profiles are flat (plug type flow) because pressure gradients vanish at these locations. At $\rho = -2.46\lambda$ the melt comes in contact with the rolls and the velocity profile indicates a pressure rise in the direction of flow. (b) Schematic view of flow patterns obtained by W. Unkrüer using color tracers. His results indicate circulation patterns not predicted by the Gaskell model. [W. Unkrüer, "Beitrag zur Ermittlung des Druckverlaufes und der Fliessvorgange im Walzspalt bei der Kalanderverarbeitung von PVC Hart zu Folien," Doctoral Dissertation, Technische Hochschule Aachen, Aachen, Germany, 1970. See also, W. Unkrüer, *Kunstoffe*, **62**, 7 (1972).]

An extremum in shear rate $\dot{\gamma} = |\dot{\gamma}_{yx}|$ and stress occur at the roll surface at $\rho = 0$, where the gap is at minimum

$$\dot{\gamma}_{\text{ext}} = \frac{3U\lambda^2}{H_0} \tag{6.4-24}$$

and

$$\tau_{\text{ext}} = \frac{3\mu U\lambda^2}{H_0} \tag{6.4-25}$$

but the overall maximum value of the shear stress and shear rate occur at $\rho = \rho_2$ if $\rho_2 > -\sqrt{1 + 2\lambda^2}$, and at $\rho = -\sqrt{1 + 2\lambda^2}$ if $\rho_2 < -\sqrt{1 + 2\lambda^2}$. The total power input into both rolls can now be calculated by integrating the product of roll velocity and the shear stress at the surface, which is obtained by setting $\xi = 1$ in Eq. 6.4-23

$$P_w = 2UW\sqrt{2RH_0}\int_{\rho_2}^{\lambda} \tau_{yx}(1)d\rho \tag{6.4-26}$$

where W is the width of the rolls, resulting in

$$P_w = 3\mu W U^2 \sqrt{\frac{2R}{H_0}} f(\lambda) \tag{6.4-27}$$

where

$$f(\lambda) = (1 - \lambda^2)[\tan^{-1}\lambda - \tan^{-1}\rho_2] - \left[\frac{(\lambda - \rho_2)(1 - \rho_2\lambda)}{(1 + \rho_2^2)}\right] \tag{6.4-28}$$

Figure 6.26(a) plots the function $f(\lambda)$.

Finally, the force separating the two rolls is obtained by integrating the pressure given in Eq. 6.4-15 over the area of the rolls this pressure acts upon

$$F_N = W\sqrt{2RH_0}\int_{\rho_2}^{\lambda} P\, d\rho \tag{6.4-29}$$

resulting in

$$F_N = \frac{3\mu URW}{4H_0} g(\lambda) \tag{6.4-30}$$

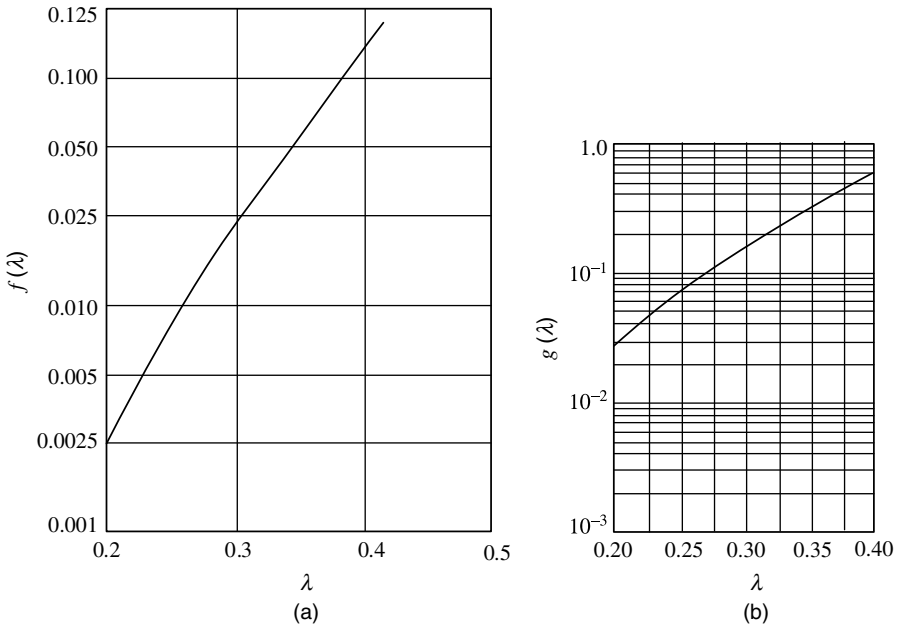

Fig. 6.26 (a) Relation between $f(\lambda)$ and λ from Eq. 6.4-28 [Reprinted by permission from G. Ehrmann and J. Vlachopoulos, *Rheol. Acta*., **14**, 761–764 (1975).] (b) $g(\lambda)$ and λ from Eq. 6.4-31. [Reprinted by permission from J. M. McKelvey, *Polymer Processing*, Wiley, New York 1962).]

where

$$g(\lambda) = \left(\frac{\lambda - \rho_2}{1 + \rho_2^2}\right) \\ [-\rho_2 - \lambda - 5\lambda^3(1 + \rho_2^2)] + (1 - 3\lambda^2)[\lambda \tan^{-1} \lambda - \rho_2 \tan^{-1} \rho_2] \tag{6.4-31}$$

The function $g(\lambda)$ is given in Fig. 6.26(b). Note that in calculating the separating force, we have neglected the roll curvature, which is consistent with the simplifying assumption on which the model is based, namely, that $h/R \ll 1$. The treatment of non-Newtonian fluids was outlined by Gaskell (32) in his original publication for Bingham Fluids. Later, McKelvey (33) reported a detailed solution for Power Law model fluids.

As shown in Fig. 6.25(a) $\dot{\gamma}_{yx}(\xi) \geq 0$ for $\rho < -\lambda$, and $\dot{\gamma}_{yx} \leq (\xi) \leq 0$ for $\rho > -\lambda$, where $-\lambda$ is a yet unknown location, and where the pressure profile exhibits a maximum value (or $dP/dx = 0$). Moreover, because of symmetry, we have the convenient boundary condition $\tau_{yx} = \dot{\gamma}_{yx} = 0$ at $y = 0$ or $\xi = 0$. Making the same simplifying assumptions as the Newtonian analysis, the following results are obtained for the velocity profile and flow rate:

$$v_x = U + \frac{\text{sign}(\dot{P})}{(1 + s)} \left[\frac{\text{sign}(\dot{P})}{m} \frac{dP}{dx}\right] (y^{1+s} - h^{1+s}) \tag{6.4-32}$$

where $\text{sign}(\dot{P})$ is defined as

$$\text{sign}(\dot{P}) = \frac{dP/dx}{|dp/dx|} = \begin{pmatrix} +1 & \rho < -\lambda \\ -1 & \rho > -\lambda \end{pmatrix} \tag{6.4-33}$$

and

$$q = 2h\left\{U - \text{sign}(\dot{P})\left(\frac{h}{2 + s}\right)\left[\text{sign}(\dot{P})\frac{h}{m}\frac{dP}{dx}\right]^s\right\} \tag{6.4-34}$$

By expressing the flow rate in terms of the clearance at the point of detachment, the following expression is obtained for the pressure gradient:

$$\frac{dP}{dx} = K\frac{[\text{sign}(\dot{P})(\rho^2 - \lambda^2)]^n}{(1 + \rho^2)^{2n+1}} \tag{6.4-35}$$

where

$$K = \text{sign}(\dot{P})m\sqrt{\frac{2R}{H_0}}\left[\frac{(2 + s)}{2H_0}\right]^n \tag{6.4-36}$$

The pressure profile is obtained by numerical integration of Eq. 6.4-35, where λ is given by Eq. 6.4-16 and is determined by the flow rate.

Experimental measurements of pressure profiles in calenders were conducted by Bergen and Scott (34). A strain gauge transducer was embedded in the surface of one of the 10-in-diameter rolls, and traces were recorded at various conditions corresponding to both calendering and roll milling.

Figure 6.27 compares the experimental pressure profiles using plasticized thermoplastic resin (unfortunately, the rheological flow curve was not provided) with

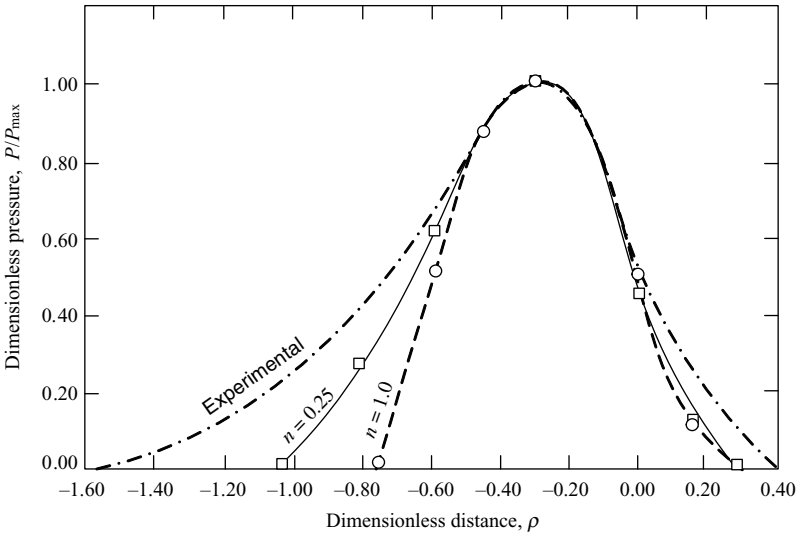

Fig. 6.27 Comparison between experimental pressure profile for plasticized thermoplastic resin (34) and theoretical pressure profiles for $n = 1$ and $n = 0.25$ calculated by Kiparissides and Vlachopoulos (35). The theoretical curves were calculated both by finite element method and analytically by way of Gaskell type models, as discussed in this section, giving virtually identical results. [Reprinted by permission from C. Kiparissides and J. Vlachopoulos, "Finite Element Analysis of Calendering," *Polym. Eng. Sci.*, **16**, 712–719 (1976).]

theoretically calculated profiles by Kiparissides and Vlachopoulos (35) using Newtonian and Power Law model fluid models. The maximum pressure was forced to coincide by appropriate selection of λ. With a Newtonian fluid, a good agreement between experiment and theory is observed in the region $\rho > -\lambda$; whereas, in the region $\rho < -\lambda$, the theoretical prediction falls well below the experimental measurements. The same conclusion is reached when the comparison is made by selecting a viscosity that forces the experimental and theoretical curves to coincide at $\rho = 0$, and matching the location of maximum pressures, as done originally by Bergen and Scott (34). This effective viscosity was lower by three orders of magnitude than the measured viscosity. The latter, however, was measured at much lower shear rates than those prevailing in the nip region.

This disagreement between theory and practice must therefore partly be due to the non-Newtonian shear-thinning viscosity. This conclusion is supported by the work of Kiparissides and Vlacopoulos (35), who showed that for a Power Law model fluid, lower n values reduce the disagreement between theory and experiments, as illustrated in Fig. 6.27. They used the FEM for computing the pressure profile, which eliminates the geometrical approximations needed in the Gaskell model.

Alternatively the two-roll geometry can be conveniently represented by bipolar coordinates, as suggested by Finston (36). This approach, as well as the FEM, enables the analyses of both equal and unequal roll diameters and frequency of rotation, termed asymmetrical calendering. However, the FEM method provides the most flexibility in dealing with both Newtonian and non-Newtonian fluids and asymmetrical calendering. Chapter 15 covers this method in some detail.

In addition to the shear thinning effect, other non-Newtonian properties bring about additional complexities in the flow pattern, as demonstrated by Unkrüer (37), such as cross-machine flow superimposed on the main machine-direction flow in the inlet region.

By using color tracers, he also revealed a much more complex flow and several circulating regions, as shown in Fig. 6.25. The results indicate that the incoming stream of melt elastic normal-stress properties and possibly roll deflection may all affect the flow pattern. All these effects are neglected in the Gaskell model; therefore, it is not surprising that the predication of the model is at variance with the experimental findings. Yet, the model does explain the basic elements of the process; it gives an insight into its nature and can serve well for first-order approximations. Further discussion on calendering is given in Chapter 15.

6.5 THE NORMAL STRESS PUMP

In Section 6.1 we noted that the term $\nabla \cdot \boldsymbol{\tau}$ in the equation of motion is an important source of pressurization. We have further pointed out that this source may be related either to viscosity or to the normal stress difference coefficient. We discuss the latter case in this section.

Consider a two-disk geometry of radii R with one of the disks rotating at frequency Ω and a non-Newtonian polymeric melt filling the space between them, as shown in Fig. 6.28. This geometrical arrangement is a schematic representation of a centripetal[8] normal stress extruder suggested by Maxwell and Scalora (38) and analyzed by a number of investigators, both theoretically and experimentally (39–41).

When a Newtonian fluid is placed between the disks, the centrifugal forces created by the rotational motion "sucks" the fluid in through the die and expels it at the circumference, much as a centrifugal pump would do. If a non-Newtonian fluid exhibiting normal stresses is placed between the disks, however, an opposite effect is observed, namely, an inward radial flow *into* the die. We have seen in Example 3.2, Eq. E3.2-13, that for the cone-and-plate flow, which is similar to flow between parallel disks, the total thrust on the plate is given by that product of the plate area and one-half the primary normal stress difference. Furthermore, we saw that the experimentally measured radial pressure distribution increases logarithmically with *decreasing* radius, the relationship containing both the primary and secondary normal stress differences.

In the normal stress extruder we first want to evaluate the pressure at the center as a function of disk outer radius, frequency of rotation, and rheological properties. We do this in the absence of radial flow (i.e., for a closed discharge condition), which will give us the

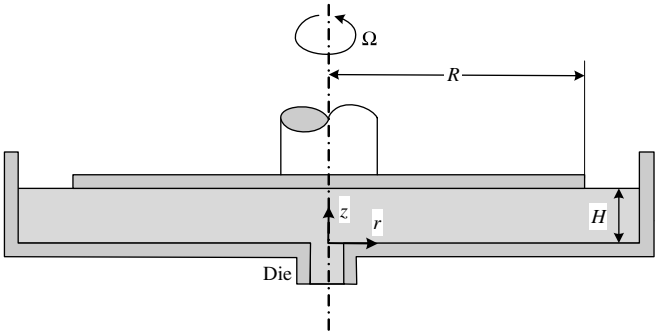

Fig. 6.28 Schematic view of the normal stress extruder. Polymer melt is placed between the disks. The upper disk is attached to a rotating shaft at frequency of rotation Ω. A pressure profile of increasing pressure toward the center develops, and the melt is extruded through the die.

8. The first centripetal pump resulting from non-Newtonian properties of liquids was suggested by Marcus Reiner in the 1950s.

maximum attainable pressure for the set conditions, and we neglect any possible secondary flows as well ($v_r = v_z = 0$), although such flows ("cigar rolling") have been observed (30). These flows impose practical limits on the pressurization capability of the normal stress extruder by forcing upper limits on Ω and R. Yet even under these rather severe simplifying assumptions, unlike the flow in the cone and plate configuration, the flow between the disks is nonviscometric, because the nonvanishing velocity component v_θ is a function of both r and z, $v_\theta(r, z)$. Nevertheless, we use the Criminale–Ericksen–Filbey (CEF) equation (Eq. 3.3-5), which, as pointed out in Chapter 3, is applicable to moderately nonviscometric flows with reasonable accuracy. Finally, steady isothermal flow with no-slip at the walls is assumed.

To determine what stresses are generated in the torsional disk flow of a CEF fluid, we assume that its flow field is that of a pure viscous fluid; then we calculate the tensor quantities $\boldsymbol{\nabla}\mathbf{v}, \dot{\boldsymbol{\gamma}}, \boldsymbol{\omega}, \{\dot{\boldsymbol{\gamma}} \cdot \dot{\boldsymbol{\gamma}}\}$, $\{\boldsymbol{\omega} \cdot \dot{\boldsymbol{\gamma}}\}$, and $\{\mathbf{v} \cdot \boldsymbol{\nabla}\dot{\boldsymbol{\gamma}}\}$ that appear in the CEF equation. Obtaining these quantities, we substitute them in the constitutive equation to find out which are the nonzero stress components.

Assuming that the flow kinematics of CEF and Newtonian fluids are identical, the velocity profile in steady torsional disk flow is

$$v = \Omega r \frac{z}{H} \tag{6.5-1}$$

where H is the separation between the disks. Thus from Table 2.3 and Table 3.3, we obtain

$$\dot{\boldsymbol{\gamma}} = \begin{pmatrix} 0 & 0 & 0 \\ 0 & 0 & \dfrac{\Omega r}{H} \\ 0 & \dfrac{\Omega r}{H} & 0 \end{pmatrix} \tag{6.5-2}$$

$$\boldsymbol{\omega} = \begin{pmatrix} 0 & 2\dfrac{\Omega r}{H} & 0 \\ -2\dfrac{\Omega r}{H} & 0 & -\dfrac{\Omega r}{H} \\ 0 & \dfrac{\Omega r}{H} & 0 \end{pmatrix} \tag{6.5-3}$$

The following expressions are obtained from Eqs. 6.5-2 and 6.5-3:

$$\{\dot{\boldsymbol{\gamma}} \cdot \dot{\boldsymbol{\gamma}}\} = \begin{pmatrix} 0 & 0 & 0 \\ 0 & \left(\dfrac{\Omega r}{H}\right)^2 & 0 \\ 0 & 0 & \left(\dfrac{\Omega r}{H}\right)^2 \end{pmatrix} \tag{6.5-4}$$

$$\{\boldsymbol{\omega} \cdot \dot{\boldsymbol{\gamma}}\} = \begin{pmatrix} 0 & 0 & \dfrac{2\Omega^2 rz}{H^2} \\ 0 & -\left(\dfrac{\Omega r}{H}\right)^2 & 0 \\ 0 & 0 & \left(\dfrac{\Omega r}{H}\right)^2 \end{pmatrix} \tag{6.5-5}$$

and

$$\{\dot{\boldsymbol{\gamma}}\cdot\boldsymbol{\omega}\} = \begin{pmatrix} 0 & 0 & 0 \\ 0 & \left(\frac{\Omega r}{H}\right)^2 & 0 \\ -\frac{2\Omega^2 rz}{H^2} & 0 & -\left(\frac{\Omega r}{H}\right)^2 \end{pmatrix} \tag{6.5-6}$$

Finally, using Table 3.2 we obtain

$$\{\mathbf{v}\cdot\boldsymbol{\nabla}\dot{\boldsymbol{\gamma}}\} = \begin{pmatrix} 0 & 0 & -\frac{\Omega^2 rz}{H^2} \\ 0 & 0 & 0 \\ -\frac{\Omega^2 rz}{H^2} & 0 & 0 \end{pmatrix} \tag{6.5-7}$$

Substituting the preceding equation into the CEF equation (Eq. 3.3-5) gives

$$\begin{pmatrix} \tau_{rr} & \tau_{r\theta} & \tau_{rz} \\ \tau_{\theta r} & \tau_{\theta\theta} & \tau_{\theta z} \\ \tau_{zr} & \tau_{z\theta} & \tau_{zz} \end{pmatrix} = -\eta \begin{pmatrix} 0 & 0 & 0 \\ 0 & 0 & \frac{\Omega r}{H} \\ 0 & \frac{\Omega r}{H} & 0 \end{pmatrix} - \frac{1}{2}(\Psi_1 + 2\Psi_2) \begin{pmatrix} 0 & 0 & 0 \\ 0 & \left(\frac{\Omega r}{H}\right)^2 & 0 \\ 0 & 0 & \left(\frac{\Omega r}{H}\right) \end{pmatrix}$$
$$+ \frac{\Psi_1}{2} \begin{pmatrix} 0 & 0 & 0 \\ 0 & -\left(\frac{\Omega r}{H}\right)^2 & 0 \\ 0 & 0 & \left(\frac{\Omega r}{H}\right)^2 \end{pmatrix} \tag{6.5-8}$$

Thus, the stress components for the assumed flow kinematics and for $\dot{\gamma} = \dot{\gamma}_{\theta z}(r) = (\Omega r/H)$:

$$\begin{aligned} \tau_{rr} &= 0 \\ \tau_{\theta\theta} &= -(\Psi_1 + \Psi_2)\left(\frac{\Omega r}{H}\right)^2 = -(\Psi_1 + \Psi_2)\dot{\gamma}^2 \\ \tau_{zz} &= -\Psi_2\left(\frac{\Omega r}{H}\right)^2 \\ \tau_{\theta z} &= \tau_{z\theta} = -\eta\left(\frac{\Omega r}{H}\right) = -\eta\dot{\gamma} \\ \tau_{r\theta} &= \tau_{\theta r} = \tau_{rz} = \tau_{zr} = 0 \end{aligned} \tag{6.5-9}$$

Hence the normal stress difference functions, keeping in mind the direction convention as discussed in Section 3.1, and noting that in this case θ is direction 1, z is direction 2, and r is direction 3, are

$$\tau_{11} - \tau_{22} = -\Psi_1\left(\frac{\Omega r}{H}\right)^2 = -\Psi_1\dot{\gamma}^2 \tag{6.5-10}$$

and

$$\tau_{22} - \tau_{33} = -\Psi_2 \left(\frac{\Omega r}{H}\right)^2 = -\Psi_2 \dot{\gamma}^2 \tag{6.5-11}$$

Having all the stress tensor components, we can proceed with the equation of motion, whose components reduce to (41)

$$-\rho \frac{v_\theta^2}{r} = -\frac{\partial P}{\partial r} + \frac{\tau_{\theta\theta}}{r} \tag{6.5-12}$$

$$\frac{\partial P}{\partial \theta} = 0 \tag{6.5-13}$$

and

$$\frac{\partial P}{\partial z} = 0 \tag{6.5-14}$$

Hence, we find that the pressure is a function of only the coordinate r. Substituting $\tau_{\theta\theta}$ from Eq. 6.5-9 and Eq. 6.5-1 into Eq. 6.5-12, we obtain

$$\frac{dP}{dr} = \rho \Omega^2 r \left(\frac{z}{H}\right)^2 - (\Psi_1 + \Psi_2) \left(\frac{\Omega}{H}\right)^2 r \tag{6.5-15}$$

The first term on the right-hand side is due to centrifugal forces and contributes to *increasing* the pressure with r, as expected; whereas, the second term is due to normal stress differences and contributes to *decreasing* pressure with r, because as pointed out in Chapter 3, experimental evidence for the shear-rate range of interest indicates that Ψ_1 is positive and Ψ_2 is negative and smaller by an order of magnitude (namely, $-\Psi_2/\Psi_1 \sim 0.1$). Furthermore, we note a certain inconsistency between the assumptions and the results. For the *assumed* velocity profile, we obtained from the equation of motion that $P \neq f(z)$; yet Eq. 6.5-15 indicates a z dependence. In reality, we should obtain a circulatory flow due to circulatory motion resulting in nonvanishing $\partial P/\partial z$, v_z, and v_r terms. Our solution is, therefore, valid only for negligible circulatory flow. Indeed, we are interested in the particular case of negligible centrifugal forces as compared to normal stress forces. Next, we average the pressure over z to obtain

$$\frac{d\bar{P}}{dr} = \rho \frac{\Omega^2 r}{3} - (\Psi_1 + \Psi_2) \left(\frac{\Omega}{H}\right)^2 r \tag{6.5-16}$$

Equation 6.5-16 can be integrated to give the pressure at $r = 0$:

$$\begin{aligned} \bar{P}(0) &= \bar{P}(R) + \left(\frac{\Omega}{H}\right)^2 \int_0^R (\Psi_1 + \Psi_2) r \, dr - \rho \frac{\Omega^2 R^2}{6} \\ &= \bar{P}(R) + \int_0^{\Omega R/H} (\Psi_1 + \Psi_2) \dot{\gamma} \, d\dot{\gamma} - \rho \frac{\Omega^2 R^2}{6} \end{aligned} \tag{6.5-17}$$

Assuming that Ψ_1 and Ψ_2 are shear rate independent, we obtain the following expression for the pressure at $r = 0$:

$$\bar{P}(0) = \bar{P}(R) + \frac{1}{2} \left(\frac{\Omega R}{H}\right)^2 (\Psi_1 + \Psi_2) - \rho \frac{\Omega^2 R^2}{6} \tag{6.5-18}$$

which is the design equation for the normal stress pump.

We find the maximum pressure rise at the center of the disk to be proportional to the square of $\Omega R/H$, which is the shear rate at $r = R$. Moreover, by comparing Eq. 6.5-18 to Eqs. 6.5-10 and 6.5-11, we find that this pressure rise is the sum of the primary and secondary normal stress-difference functions $\{-[(\tau_{11} - \tau_{22}) + (\tau_{22} - \tau_{33})]\}$ at $r = R$, less centrifugal forces. Since Ψ_2 is probably negative, it opposes pressurization; hence, the source of the pressurization in the normal stress extruder is the *primary* normal stress difference function Ψ_1.

Example 6.9 The Maximum Pressure in the Normal-Stress Extruder Calculate the maximum pressure (at closed discharge) in a normal stress extruder of two 25-cm radius disks at 0.5 cm apart, shearing Low Density Polyethylene (LDPE) at 60 rpm and 200°C.

Solution We do not have good data on Ψ_2, but we know that it is an order of magnitude smaller than Ψ_1, therefore, we shall assume the former to be negligible compared to the latter. The shear rate ranges from zero at the center to a maximum value at R, $\dot{\gamma}(R) = \Omega R/H = 314.2\,\text{s}^{-1}$. Figure 3.26 shows experimental data on Ψ_1 for LDPE. At 200°C we can calculate the following shear rate dependence

$$\Psi_1(\dot{\gamma}) \cong 9 \times 10^4 \dot{\gamma}^{-0.92}$$

Furthermore, we assume that this relationship holds for shear rates greater than $10\,\text{s}^{-1}$. Then, substituting this relationship into Eq. 6.5-17 followed by integration and taking $P(R) = 0$ and melt density $0.75\,\text{g/cm}^3$, we obtain

$$\bar{P}(0) = \frac{(9 \times 10^4)}{(1.08)}(314.2^{1.08}) - \frac{(0.75)(25^2)}{(6)} = 4.17 \times 10^6\,\text{N/m}^2\ (605\,\text{psi})$$

Two facts are worth noting. First, the normal stress pressurization is indeed much greater (10^5 times) than that brought about by centrifugal forces. Second, the level of the maximum pressure generated even at closed discharge is significant but inadequate for most processing applications. One could suggest increasing the disk speed, but we must remember that secondary flows (e.g., cigar rolling) will place rather tight upper bounds.

So far we have neglected radial flow, but in a normal stress extruder the objective is to extrude the polymer melt through a die. Such flow, however, implies a pressure loss in the inward radial direction, consequently reducing the maximum pressure at the die entrance. The die resistance determines the ensuing flow rate; at steady flow conditions, the pressure rise in the radial direction equals the pressure drop across the die.

Rigorous analytical solution of this flow problem is difficult. Good et al. (40) proposed the following approximate analytical approach, which resulted in good agreement with their experiments: they assumed that the pressure rise due to normal stresses (ΔP_{NS}) in a closed discharge condition, the pressure loss between the disks due to radial flow (ΔP_{RF}), and entrance losses into the die (ΔP_{DE}) are related to the available pressure drop for pumping across the die as follows:

$$\Delta P_T = \Delta P_{NS} - \Delta P_{RF} - \Delta P_{DE} \tag{6.5-19}$$

Figure 6.29 compares predicted pressures with an experimentally measured pressure using a polyacrylamide solution. There is an optimum separation between the disks for

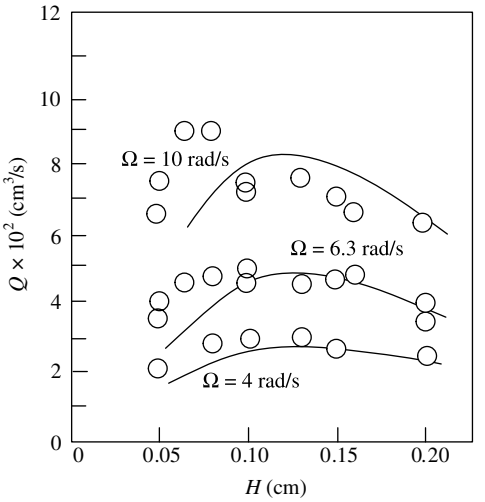

Fig. 6.29 Flow rate versus disk gap separation in normal stress pump. The polymer used was polyacrylamide solution at 28°C. Smooth curves indicate calculated values. The die was 0.482 cm long and had a diameter of 0.244 cm. [Data replotted from P. A. Good, A. J. Swartz, and C. W. Macosko, *AIChE J.*, **20**, 67(1974).]

maximum pressurization due to the different H dependence of pressure rise due to normal stress and pressure drop due to viscous radial flow.

The normal stress extruder can also be used for melting, as shown in Fig. 6.30. However, because of the limited pressurization capability, various modifications have

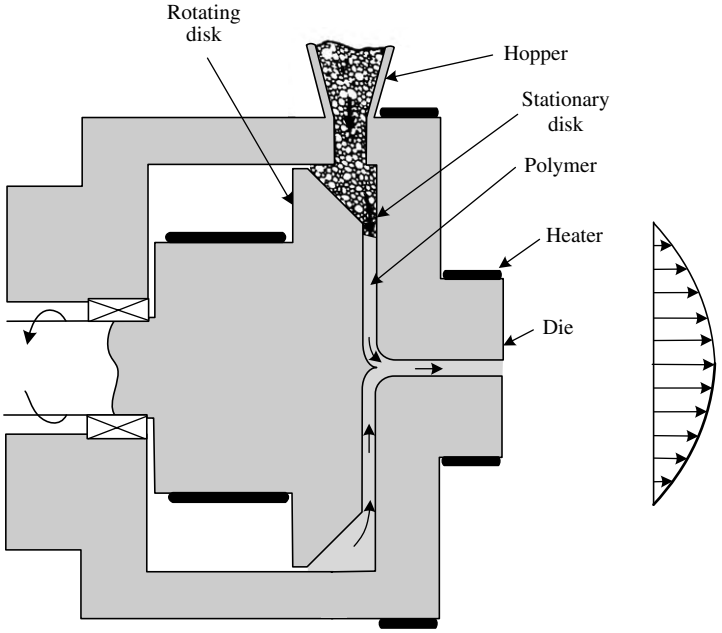

Fig. 6.30 Schematic representation of a plasticating normal stress extruder.

been suggested, one of these being a combination with a screw. Yet in spite of the modification, it has found only limited use as an extrusion system, although it appears that a later modification (42) has certain advantages in processing hard-to-mix materials.

6.6 THE CO-ROTATING DISK PUMP

In Example 6.7 we described the synthesis of a co-rotating disk processor (CDP) from building block 2 consisting of two jointly moving plates. In this section we wish to derive a mathematical model to relate flow rate and pressure rise with geometrical and operational variables. We begin by first making a comparison between a jointly moving plate configuration (JMP) pump and a single moving plate configuration (SMP) pump (43).

Example 6.10 A Comparison between an SMP- and a JMP-based Pump Figure E6.10 shows the two configurations with plates at distance H apart and constant plate velocities of V_0. For steady, fully developed isothermal flow of a Newtonian fluid, we have shown in Example 2.5 that the flow rate is given by

$$q = \frac{V_0 H}{2} - \frac{H^3}{12\mu}\left(\frac{\Delta P}{L}\right) \tag{E6.10-1}$$

where H is the separation between the plates, L is the length of the plates, ΔP is the pressure rise ($P_{\text{discharge}} - P_{\text{inlet}}$), and μ is the viscosity. This equation can be rearranged as

$$\Delta P = \frac{12\mu}{H^3}\left(\frac{V_0 H}{2} - q\right) \tag{E6.10-2}$$

For the JMP configuration, it is easy to show that the corresponding equations are

$$q = V_0 H - \frac{H^3}{12\mu}\left(\frac{\Delta P}{L}\right) \tag{E6.10-3}$$

and

$$\Delta P = \frac{12\mu}{H^3}(V_0 H - q) \tag{E6.10-4}$$

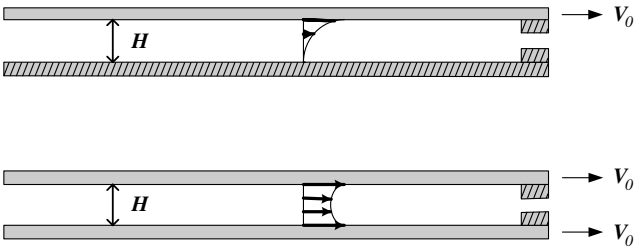

Fig. E6.10 Jointly moving plate (JMP) and single moving plate (SMP) configurations with schematic velocity profiles.

The increase in the drag-flow rate has a profound effect on performance. For a given flow rate q, the optimum gap size in SMP and JMP configurations can be obtained by differentiating Eqs. E6.10-2 and E6.10-4, respectively, with respect to H to give $H_{\text{opt}} = 3q/V_0$ and $H_{\text{opt}} = 3q/2V_0$. Next we substitute these values in Eqs. E6.10-2 and E6.10-4 and find that the ratio of pressure rises is

$$\frac{(\Delta P_{\max})_{JMP}}{(\Delta P_{\max})_{SMP}} = 8 \tag{E6.10-5}$$

Similarly, we find that the maximum flow-rate ratio for a given pressure rise is

$$\frac{(q_{\max})_{JMP}}{(q_{\max})_{SMP}} = \sqrt{8} \tag{E6.10-6}$$

For non-Newtonian Power Law model fluids, these ratios are

$$\frac{(\Delta P_{\max})_{JMP}}{(\Delta P_{\max})_{SMP}} = (1+s)2^{(1+n)} \tag{E6.10-7}$$

and

$$\frac{(q_{\max})_{JMP}}{(q_{\max})_{SMP}} = 2(1+s)^{1/(1+n)} \tag{E6.10-8}$$

where n is the power law exponent, and $s = 1/n$.

Thus, for Newtonian fluids, the pressurization capability of the optimized JMP is eight times that of the SMP, and for non-Newtonian fluids, the ratio exhibits a minimum at $n = 0.801$ and rises to 11.59 at $n = 0.25$; whereas, the flow rate at fixed pressure rise for Newtonian fluids is $8^{1/2} = 2.83$ times in JMP as compared to SMP, and for non-Newtonian fluids with $n = 0.25$ it rises to 7.25. Clearly, the JMP configuration is about an order of magnitude more efficient then the SMP one. Moreover, the specific power input in a JMP configuration for Newtonian fluids is one-half that of the SMP, and for $n = 0.25$, it is one-fifth; the corresponding ratios for specific power dissipated into heat are, one-quarter and 1/25, respectively.

The geometrical configuration of the CDP is shown in Fig. 6.31. The space between the disks can be parallel or wedged, with the latter being the optimum configuration. Tadmor et al (44) derived the mathematical model for the CDP assuming steady, fully developed[9] laminar, isothermal flow of an incompressible non-Newtonian Power Law model liquid. We begin with the parallel-disk configuration, with disk outer and inner radii R_d and R_s, respectively, at a distance H apart and rotating at frequency N. We select a cylindrical coordinate system located at the center of the shaft between the disks. As the disks rotate, they drag the fluid from the inlet to the outlet, and when there is a resistance at the outlet (i.e., a die), pressure is built up toward the outlet. We assume steady isothermal and laminar fully developed flow of an incompressible non-Newtonian Power Law model fluid, and further assume that the effect of the root of the screw and barrel are negligible.[10]

9. This assumption is valid only far from the inlet and exit regions, but as we shall see later, the distance between the disks is relatively small, and therefore this assumption is quite reasonable.

10. This implies that $H \ll R_d - R_s$, an assumption equivalent to neglecting flight effects in an SSE. Later we will show how to account for these "wall" effects.

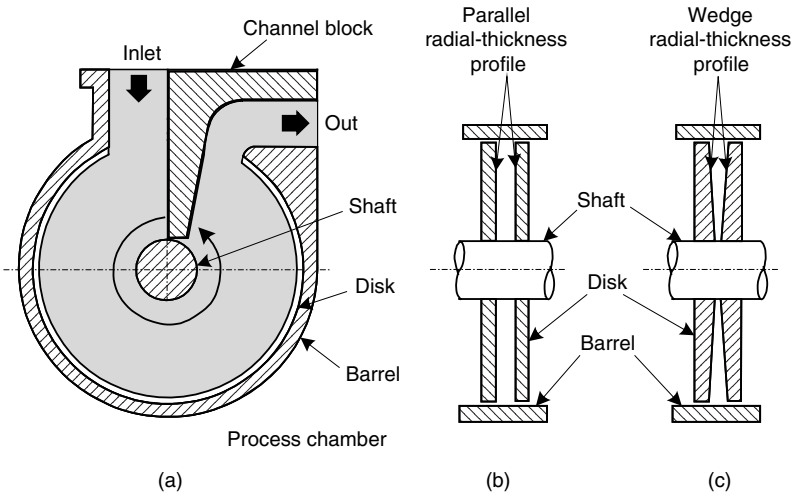

Fig. 6.31 Schematic view of a co-rotating-disk pump. (a) The disks are attached to a rotating shaft and placed within a barrel having an inlet and an outlet port, separated by a channel block attached to the stationary barrel. The space between inlet and outlet ports, the disks, and the channel block form the processing chamber, (b) parallel arrangements of the disks; (c) wedge-shaped disks.

The only nonvanishing velocity component is v_θ and it is a function only of the angular coordinates r and z. The other two velocity components v_z and v_r vanish, as implied from the equation of continuity for fully developed flow. The flow kinematics also imply that $\tau_{rr} = \tau_{zz} = \tau_{\theta\theta} = \tau_{rz} = 0$ and the only nonvanishing stress components are $\tau_{\theta z}$ and $\tau_{r\theta}$. Consequently the equation of motion reduces to

$$\frac{\partial P}{\partial r} = 0 \tag{6.6-1}$$

$$-\frac{1}{r}\frac{\partial P}{\partial \theta} = \frac{1}{r^2}\frac{\partial}{\partial r}(r^2\tau_{r\theta}) + \frac{\partial \tau_{\theta z}}{\partial z} \tag{6.6-2}$$

$$\frac{\partial P}{\partial z} = 0 \tag{6.6-3}$$

Equations 6.6-1 and 6.6-3 indicate that P is only a function of θ. Furthermore, since the right-hand side of Eq. 6.6-2 is not a function of θ, we conclude that $\partial P/\partial\theta$ is a constant, that is, the angular pressure gradient is constant or the pressure rises linearly with θ. The stress components $\tau_{\theta z}$ and $\tau_{r\theta}$, consistent to our assumption, reduce to

$$\tau_{r\theta} = -\eta\left[r\frac{\partial}{\partial r}\left(\frac{v_\theta}{r}\right)\right] \tag{6.6-4}$$

$$\tau_{\theta z} = -\eta\frac{\partial v_\theta}{\partial z} \tag{6.6-5}$$

The relative significance of these stress components can be estimated by the following order-of-magnitude calculations

$$\frac{|\tau_{r\theta}|}{|\tau_{\theta z}|} = \frac{\left|r\dfrac{\partial}{\partial r}\left(\dfrac{v_\theta}{r}\right)\right|}{\left|\dfrac{\partial v_\theta}{\partial z}\right|} \cong \frac{r\left(\dfrac{1}{R_d - R_s}\right)\left(\dfrac{\Omega r}{r}\right)}{\left(\dfrac{\Omega r}{H}\right)} \cong \frac{H}{R_d - R_s} \tag{6.6-6}$$

where Ω is the angular velocity. Clearly, in the geometry considered here, $H/(R_d - R_s) \ll 1$ and therefore $\tau_{r\theta} \ll \tau_{\theta z}$. The stress component $\tau_{r\theta}$ vanishes at the disk surfaces and increases toward the center. In a wedge-shaped gap (H/r = constant) the angular velocity v_θ/r is not a function of r and $\tau_{r\theta}$ vanishes everywhere. In either case, Eq. 6.6-2 reduces to

$$-\frac{1}{r}\frac{\partial P}{\partial \theta} = \frac{\partial \tau_{\theta z}}{\partial z} \tag{6.6-7}$$

which can be integrated to give

$$\tau_{\theta z} = -\left(\frac{1}{r}\frac{dP}{d\theta}\right)z + C \tag{6.6-8}$$

where C is an integration constant. Due to symmetry, $\tau_{\theta z} = 0$ at $z = 0$, and therefore, $C = 0$. Expressing this stress component in terms of the velocity gradients using the Power Law model gives

$$m\left|\frac{\partial v_\theta}{\partial z}\right|^{n-1}\frac{\partial v_\theta}{\partial z} = \left(\frac{1}{r}\frac{dP}{d\theta}\right)z \tag{6.6-9}$$

where m and n are the Power Law parameters. The velocity gradient is positive for $z > 0$, and Eq. 6.6-9 can be written as

$$\frac{\partial v_\theta}{\partial z} = \left[\frac{1}{mr}\left(\frac{dP}{d\theta}\right)\right]^s z^s \tag{6.6-10}$$

where $s = 1/n$. The velocity component v_θ is a function of z and r, but from the previous conclusion that $\tau_{r\theta} \approx 0$, it follows that $\partial(v_\theta/r)/\partial r \approx 0$, and therefore $v_\theta/r = f(z)$, where $f(z)$ is yet an unknown function of z, or

$$v_\theta = rf(z) \tag{6.6-11}$$

Substituting Eq. 6.6-11 into Eq. 6.6-10 gives

$$r\dot{f}(z) = \left[\frac{1}{mr}\left(\frac{dP}{d\theta}\right)\right]^s z^s \tag{6.6-12}$$

which subsequent to integration yields

$$f(z) = \left[\frac{1}{mr}\frac{dP}{d\theta}\right]^s \frac{z^{s+1}}{s+1} + C_0(r) \tag{6.6-13}$$

where $C_0(r)$ is an integration constant that may be a function of r. Substituting Eq. 6.6-13 into Eq. 6.6-11 gives

$$v_\theta = \left[\frac{1}{mr}\frac{dP}{d\theta}\right]^s \frac{z^{s+1}}{s+1} + C_1(r) \tag{6.6-14}$$

where $C_1(r) = rC_0(r)$ is evaluated from the boundary conditions $v_\theta = (H/2) = 2\pi Nr$ to give the required velocity profile:

$$v_\theta = 2\pi Nr - \frac{1}{s+1}\left[\frac{1}{mr}\left(\frac{dP}{d\theta}\right)\right]^s \left[\left(\frac{H}{2}\right)^{s+1} - z^{s+1}\right] \tag{6.6-15}$$

The flow rate is obtained by integrating the velocity profile over the cross section

$$Q = 2\int_{R_s}^{R_d}\int_0^{H/2} v_\theta \, dz \, dr = \pi \, NHR_d^2(1-\alpha^2) - \frac{H^{2+s}}{2^{1+s}}\frac{R_d^{1-s}}{(2+s)m^s}\frac{(1-\alpha^{1-s})}{(1-s)}\left(\frac{dP}{d\theta}\right)^s \tag{6.6-16}$$

where $\alpha = R_s/R_d$. Now the pressure gradient can be expressed in terms of pressure drop (or rise) as follows:

$$\frac{dP}{d\theta} = \frac{P_{\text{out}} - P_{\text{in}}}{2\pi\varepsilon} = \frac{\Delta P}{2\pi\varepsilon} \tag{6.6-17}$$

where P_{in} and P_{out} are the inlet and outlet pressures, respectively, and $\varepsilon < 1$ is the fraction of circumference in which pressurization is taking place.

In Eq. 6.6-16 the first term on the right-hand side is the drag flow and the second term is the pressure flow. The net flow rate is their linear superposition, as in the case of the Newtonian model in single screw extrusion. The reason that in this case this is valid for non-Newtonian flow as well is because the drag flow is simply plug flow.

The shear rate distribution is obtained by differentiating the velocity profile Eq. 6.6-15 to give

$$\dot{\gamma}_{\theta z} = \left(\frac{z}{mr}\frac{dP}{d\theta}\right)^s \tag{6.6-18}$$

The power consumption is obtained by the product of the shear stress at the wall and the local disk velocity integrated over the disk surface

$$P_w = 2\int_{R_s}^{R_d}\int_0^{2\pi\varepsilon} 2\pi Nr\tau_w r \, dr \, d\theta \tag{6.6-19}$$

The shear stress at the wall is

$$\tau_w = -m\dot{\gamma}_w^n = \frac{H}{2r}\frac{dP}{d\theta} \tag{6.6-20}$$

Substituting Eq. 6.6-20 into Eq. 6.6-19 subsequent to integration yields

$$P_w = \pi NHR_d^2(1-\alpha^2)\Delta P = Q_d \Delta P \tag{6.6-21}$$

where Q_d is the drag flow.

It is easy to show that the maximum flow rate for a given pressure rise, or the maximum pressure rise for a given flow rate, are obtained for such a gap size H that satisfies the following relationship:

$$\frac{Q}{Q_d} = \frac{s+1}{s+2} \tag{6.6-22}$$

For a wedge-shaped gap such that

$$\frac{H}{r} = \frac{H_d}{R_d} \tag{6.6-23}$$

where H_d is the gap size at $r = R_d$ the velocity profile is

$$\frac{v_\theta}{r} = 2\pi N - \frac{1}{s+1}\left[\frac{1}{m}\left(\frac{dP}{d\theta}\right)\right]^s \left(\frac{H_d}{R_d}\right)^{s+1}\left[1 - \left(\frac{2z}{H}\right)^{s+1}\right] \tag{6.6-24}$$

We note that the angular velocity profile v_θ/r in this geometry is independent of radial position.

The flow rate is obtained by integrating the velocity profile over the cross section of the channel to give

$$Q = \frac{2}{3}\pi N H_d R_d^2(1-\alpha^3) - \frac{H_d^{s+2} R_d^{1-s}(1-\alpha^3)}{6(s+2)2^s m^s}\left(\frac{dP}{d\theta}\right)^s \tag{6.6-25}$$

Example 6.11 Drag Flow Rate in a CDP Pump Consider a 20-cm-diameter disk CDP with $\alpha = 0.5$ and $H = 1$ cm rotating at 240 rpm. Calculate the volumetric flow rate.

Solution From Eq. 6.6-24 we get

$$Q_d = \pi \times 4(\mathrm{s}^{-1}) \times 10^{-2}(\mathrm{m}) \times (10^{-1})^2(\mathrm{m}^2) \times (1 - 0.5^2) = 9.427 \times 10^{-4}\,\mathrm{m}^3/\mathrm{s}$$

or 56.52 l/min. By attaching 11 disks to the same shaft we will increase the flow rate tenfold to 565.2 l/min, or 3.39 tons/h if the density is 1 g/cm^3. This is a very substantial flow rate for viscous liquids in laminar flow. In the next Example we examine the pressurization capability of the CDP.

Example 6.12 Flow Rate of LDPE in a CDP with Fixed Head Pressure Calculate the flow rate of a 2MI LDPE ($m = 4.31 \times 10^3\,\mathrm{N}\cdot\mathrm{s}^n/\mathrm{m}^2$, $n = 0.5$) in a 7.5-in-diameter CDP, with $\alpha = 0.5$ and wedged channel with $H_d = 0.25$ in, rotating at 75 rpm with a discharge pressure of 1200 psi. Assume that entrance and exit parts occupy 90° of the circumference.

Solution First we express the angular pressure gradient in terms of the pressure rise

$$\frac{dP}{d\theta} = \frac{\Delta P}{2\pi\varepsilon}$$

where the $\varepsilon = 0.75$ is the fraction of the circumference in which pressurization is taking place. Next, we insert the given data into Eq. 6.6-33 to obtain the flow rate:

$$Q = \frac{2}{3}\pi(1.25)(0.635 \times 10^{-2})(9.525 \times 10^{-2})^2(1 - 0.5^3) - \frac{(0.635 \times 10^{-2})^{2+2}}{6(2+2)(9.525 \times 10^{-2})}\left(\frac{8.2728 \times 10^6}{4\pi(0.75)(4.31 \times 10^3)}\right)^2(1 - 0.5^3)$$
$$= 1.3197 \times 10^{-4} - 0.2581 \times 10^{-4}\,[\mathrm{m}^3/\mathrm{s}]$$
$$= 1.0616 \times 10^{-4}[\mathrm{m}^3/\mathrm{s}] = 0.382\,[\mathrm{m}^3/\mathrm{h}]$$

or using a density of $0.9\,\mathrm{g/cm}^3$ results in 343.8 kg/h.

The barrel surface exerts a retarding effect on flow rate, just as the flights in a screw extruder do. Edelist and Tadmor (45) derived the shape correction factors for Newtonian fluids, which are plotted for parallel disks as a function of $H/(R_d - R_s)$ in Fig. 6.32 and for wedge-shaped disks in Fig. 6.33.

Table 6.1 provides all the design equations including power, specific power, temperature rise and mean residence time for both types of pumps. This theoretical model was verified experimentally by Tadmor et al. (43) by pumping molten polystyrene (PS) in a 7.5-in-diameter single-stage single-chamber experimental Diskpack[11] equipped with several pressure transducers at various angular positions, as shown in Fig. 6.34. The pressure profiles are shown in Fig. 6.35.

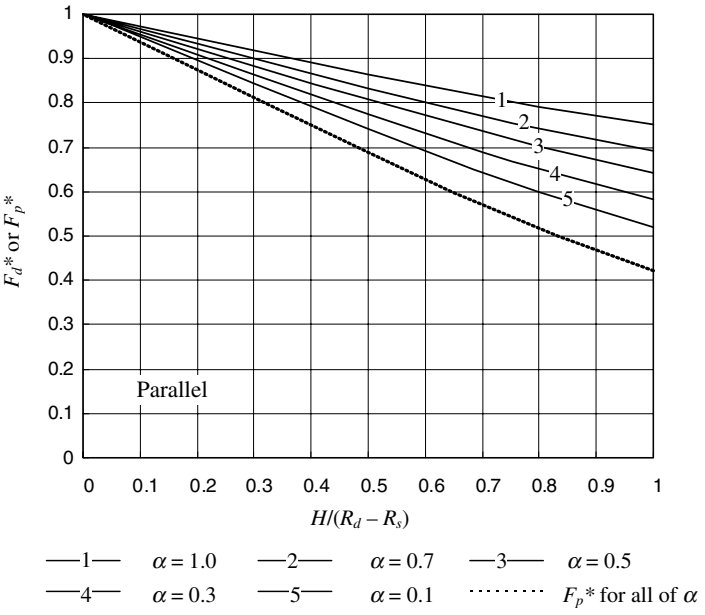

Fig. 6.32 Shape-correction factors for parallel-shaped chambers. [Reproduced by permission from Y. Edelist and Z. Tadmor, ''Velocity Profiles in a Co-rotating Disk Processor'' *Polym. Process Eng.*, **1**,1 (1983).]

11. The CDP was commercially developed into a processing machine by the Farrel Corporation of Ansonia, CT, USA, under the brand name Diskpack.

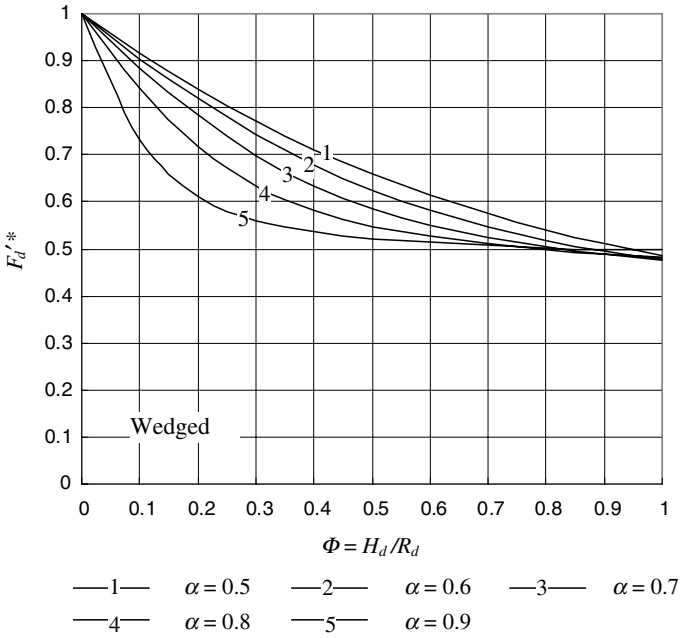

Fig. 6.33 Shape-correction factors for wedge-shaped chambers. [Reproduced by permission from Y. Edelist and Z. Tadmor, "Velocity Profiles in a Co-rotating Disk Processor" *Polym. Process Eng*., **1**, 1 (1983).]

The experiments were conducted at a constant disk speed of 70 rpm and started with open discharge, after which a discharge valve was gradually closed. Notice that, as the valve is closed, the chamber begins filling up and the discharge pressure increases. The profiles are linear as predicated by the model. As closed discharge conditions are approached, viscous dissipation begins increasing the temperature and reducing the viscosity, with a consequent drop in discharge pressure.

Figure 6.36 compares theoretical to experimental pressure gradient measured in the foregoing experimental machine and in a 350-mm-diameter machine for three different polymeric melts. Results indicate that the experimentally measured pressure gradients are up to 20% *higher* than the theoretical ones. Some possible reasons that have been suggested are either the increased drag due to cooler disks as compared to melt temperature, or stress overshoot (higher transient viscosities than used in the calculation).

Finally, Edelist and Tadmor (45) used a photogrammetric technique to experimentally verify the calculated velocity profiles, adding credibility to the theoretical model.

6.7 POSITIVE DISPLACEMENT PUMPS

Positive displacement pumps are based on a surface moving normal to its plane (building block 5 in Fig. 6.2) pressurizing the melt by an externally imposed (mechanical) force, and creating a positive displacement–type flow. There are a number of advantages to positive-displacement pumps as compared to drag-induced pumps. The latter are sensitive to the conditions at the moving surface such as, for example, wall temperature and slip at the wall, whereas, the former are generally insensitive to these problems. Moreover, flow rate

TABLE 6.1 Design Equations for Co-rotating Disk Pumps.

	Parallel Chamber	Wedge Chamber
Volumetric flow rate	$Q = Q_d - Q_p$	$Q = Q'_d - Q'_p$
Drag flow rate	$Q_d = \pi N H R_d^2 (1-\alpha^2) F_d$	$Q'_d = \frac{2}{3}\pi N H_d R_d^2 (1-\alpha^3) F'_d$
Pressure flow rate	$Q_p = \frac{H^2 R_d}{2(s+2)} \left(\frac{1-\alpha^{1-s}}{1-s}\right) \left[\frac{H}{2mR_d}\left(\frac{dP}{d\theta}\right)\right]^s F_p$	$Q'_p = \frac{H_d^2 R_d (1-\alpha^3)}{6(2+s)} \left(\frac{H_d}{2mR_d}\frac{dP}{d\theta}\right)^s F'_p$
Pressure flow for Newtonian fluids	$Q_{pN} = \frac{H^3 \ln \alpha}{12\mu}\left(\frac{dP}{d\theta}\right) F_p$	$Q_{pN} = \frac{H_d^3 (1-\alpha^3)}{36\mu}\left(\frac{dP}{d\theta}\right) F'_p$
Angular pressure gradient	$\frac{dP}{d\theta} = \frac{P_{\text{out}} - P_{\text{in}}}{2\pi\varepsilon} = \frac{\Delta P}{2\pi\varepsilon}$	
Pressure rise	$\Delta P = 4\pi m\varepsilon \frac{R_d^{1-n}}{H_d^{1+2n}} \left[\frac{2(2+s)(1+s)}{F'_p(1-\alpha^{1-s})}\right]^n (Q_d - Q)^n$	$\Delta P = 4\pi m\varepsilon \frac{R_d^{1-n}}{H_d^{1+2n}} \left[\frac{6(2+s)}{F'_p(1-\alpha^3)}\right]^n (Q'_d - Q)^n$
Pressure to drag flow ratio	$\frac{Q_p}{Q_d} = \frac{H}{2\pi N R_d} \left[\frac{1-\alpha^{1-s}}{(1-s)(1-\alpha^2)}\right] \left[\frac{H}{2mR_d}\left(\frac{dP}{d\theta}\right)\right]^s \frac{1}{(2+s)} \frac{F_p}{F_d}$	$\frac{Q'_p}{Q'_d} = \frac{H_d}{4\pi N R_d} \left[\frac{H_d}{2mR_d}\left(\frac{dP}{d\theta}\right)\right]^s \frac{1}{(2+s)} \frac{F'_p}{F'_d}$
Shaft power	$P_w = Q_d \Delta P$	$P_w = Q'_d \Delta P$
Specific energy	$P_w = \left(\frac{Q_d}{Q}\right)\Delta P$	$P_w = \left(\frac{Q'_d}{Q}\right)\Delta P$
Torque	$\mathcal{T} = H_d R_d^2 (1-a^2)\frac{\Delta P}{2}$	$\mathcal{T} = H_d R_d^2 (1-a^3)\frac{\Delta P}{3}$
Total rate of viscous heat dissipation	$E_v = Q_P\ \Delta P$	$E_v = Q'_p\ \Delta P$

Adiabatic temperature rise	$\Delta T_a = \left(\frac{1}{\rho C_p}\right)\left(\frac{Q_p}{Q}\right)\Delta P$	$\Delta T_a = \left(\frac{1}{\rho C_p}\right)\left(\frac{Q'_p}{Q}\right)\Delta P$
Mean residence time	$\bar{t} = \frac{Q_d \varepsilon}{NQ} \qquad (F_d = 1)$	$\bar{t} = \frac{Q'_d \varepsilon}{NQ} \qquad (F'_d = 1)$
Geometry	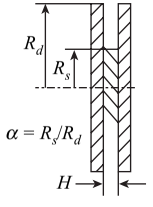	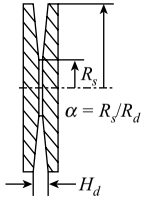
Fluid model	$\tau = \eta\dot{\gamma}$ where η is the non-Newtonian viscosity, which is a function of $\dot{\gamma}$, the magnitude of the tensor $\dot{\boldsymbol{\gamma}}$ $[\dot{\gamma} = \left(\frac{1}{2}\dot{\boldsymbol{\gamma}} : \dot{\boldsymbol{\gamma}}\right)^{1/2}]$, $\eta = m\dot{\gamma}^{n-1}$, where m and n are the Power Law model parameters and $s = 1/n$. For simple shear flow, $\dot{\gamma}$ is the shear rate. For Newtonian fluids, $n = 1$ and $\eta = m = \mu$.	

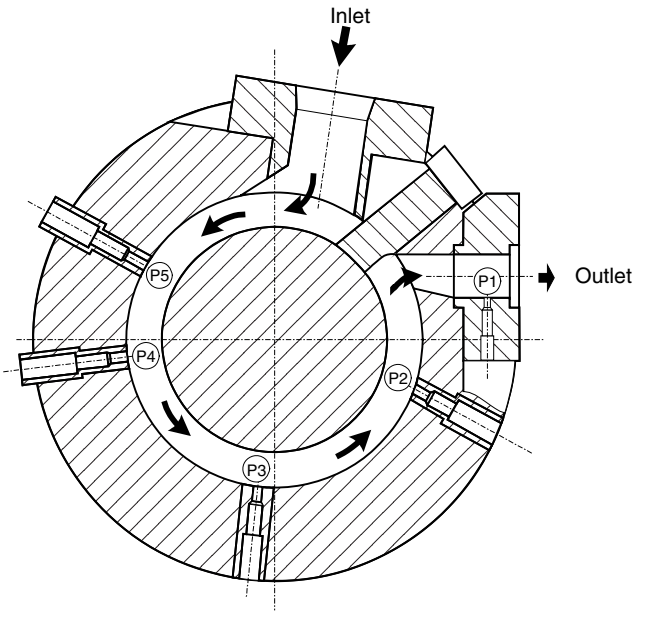

Fig. 6.34 A 7.5-in-diameter co-rotating disk pump. (Courtesy of Farrel Corporation.)

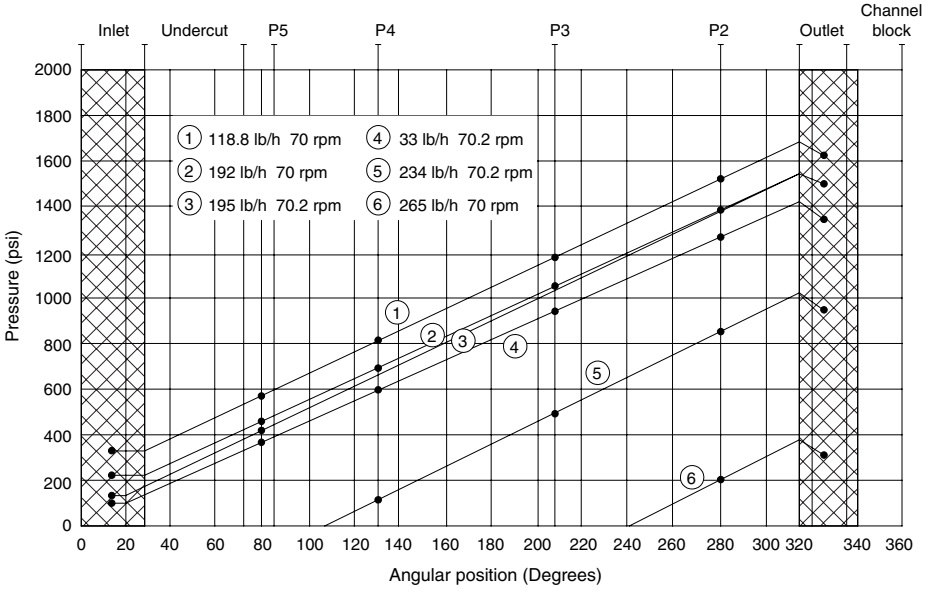

Fig. 6.35 Characteristic linear pressure profiles for molten PS in a 7.5-in-diameter pump at various discharge pressures. [Reproduced by permission from Z. Tadmor, P.S. Mehta, L.N. Valsamis and J. Yang "Co-rotating Disk Pumps for Viscous Liquids,". *Ind. Eng. Chem. Process. Res. Devel.,* **24**, 311–320 (1985).]

control (metering) is generally better and pressure sensitivity lower in positive displacement pumps as compared to drag-induced flow.

First we want to gain some insight into the nature and mechanism of positive displacement flow. In the next two examples we examine the plunger–cylinder

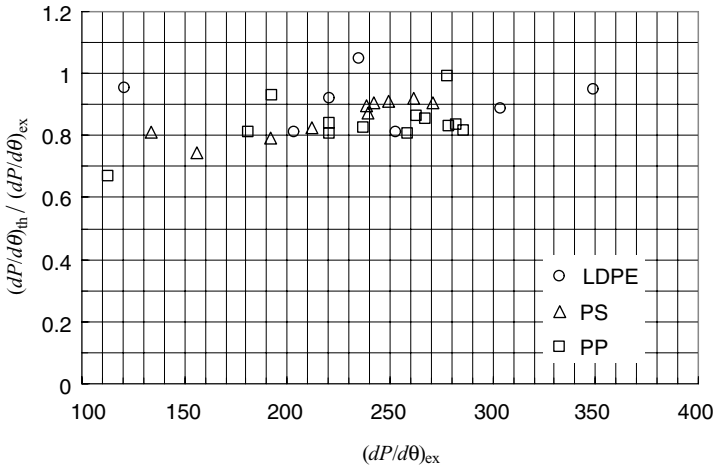

Fig. 6.36 Predicted versus measured pressure gradients for LDPE, PS, and PP. [Reproduced by per mission from Z. Tadmor, P.S. Mehta, L.N. Valsamis and J. Yang "Co-rotating Disk Pumps for Viscous Liquids,". *Ind. Eng. Chem. Process. Res. Devel.,* **24**, 311–320 (1985).]

pump and axially moving disk configurations shown schematically in Fig. 6.37(a) and Fig. 6.37(b).

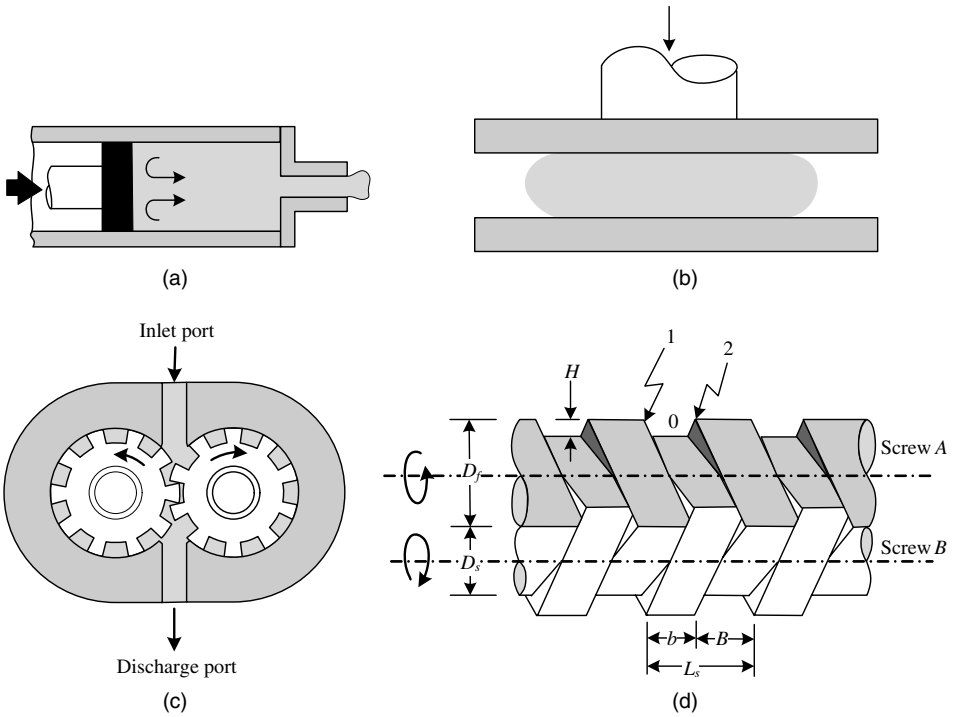

Fig. 6.37 Schematic representation of four geometrical configurations utilizing external mechanical pressurization giving rise to positive displacement flow. (a) Axially moving plunger in a cylinder. (b) Squeezing disks. (c) Intermeshing gear pump. (d) Counterrotating intermeshing twin screws.

Example 6.13 Plunger–Cylinder Pump The first recorded application of the plunger-cylinder pump in the field of polymer processing appears to have occurred in 1845 in England, for the extrusion of guttapercha. The main disadvantage of this pump for extrusion is its non-continuous operation.[12] This is, of course, irrelevant to injection molding, where the polymeric melt is pumped into the die by an axially moving cylinder. Now we discuss the flow field in front of the cylinder.

It is easier to visualize the flow field in front of the plunger in a coordinate system located on the moving surface of the plunger (*Lagrangian* point of view), as shown in Fig. E6.13. In this coordinate system, if the cylinder moves at a velocity V_0, the cylinder has a $-V_0$ velocity. By its axial motion, the cylinder drags the adjacent liquid toward the plunger. As a fluid particle approaches the plunger surface, it must acquire an inward radial velocity component while gradually decelerating the axial velocity component to zero. Then it begins to acquire a positive axial velocity component. Hence, the resulting flow pattern is one that has a ''skin'' layer of liquid moving toward the plunger, and a core layer moving axially away from the plunger. Such a flow pattern was termed by Rose (46)[13] as ''a reverse fountain flow.''

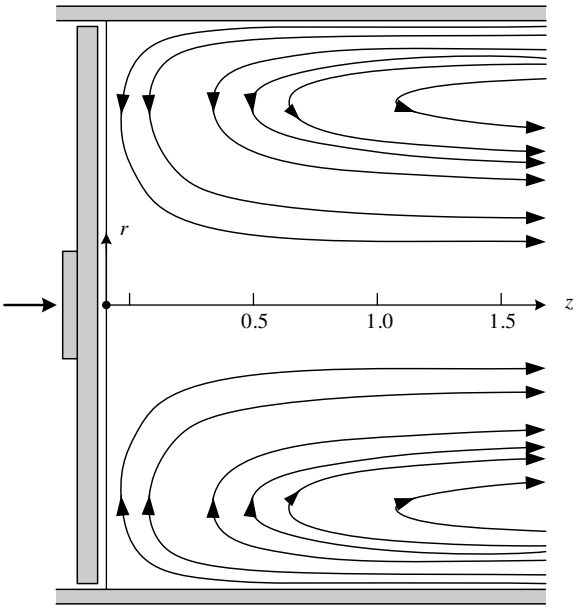

Fig. E6.13 Computed streamlines in front of the plunger, assuming isothermal flow, Newtonian fluid, and a frictionless plunger surface.

12. In an attempt to eliminate this disadvantage, Bob Westover designed a continuous plunger-type extruder using four sets of plunger cylinders, two for melting and two for pumping. [See R. F. Westover, ''Continuous Flow Ram Type Extruder,'' *Mod. Plast.* (1963).] He also designed a viscometer with two plunger cylinders connected head-on with a capillary tube between them to evaluate the effect of hydrostatic pressure on viscosity.

13. Rose examined the flow pattern in a capillary tube where one immiscible liquid displaces another one. In the front end of the displacing liquid the flow pattern is one he termed ''fountain flow,'' and in the other ''reverse fountain flow.'' In polymer processing the significance of the former was demonstrated in the advancing melt front in mold filling (see Chapter 13).

Bhattacharji and Savic (47) derived the following approximate velocity profiles:

$$v_z = V_0\left(1 - \frac{2r^2}{R^2}\right)\left(1 - e^{-z\sqrt{6/R}}\right) \tag{E6.13-1}$$

and

$$v_r = -\frac{V_0\sqrt{6}r}{R^3}(R^2 - r^2)e^{-z\sqrt{6}/R} \tag{E6.13-2}$$

We note that if V_0 is added to v_z, the "laboratory" frame of reference is restored (i.e., stationary cylinder and moving plunger), and that at large z values the velocity profile converges to the familiar Poiseuille-type parabolic profile. We also observe that at an axial distance of one radius from the plunger, 91% of the fully developed velocity profile is obtained and at one diameter from the plunger, 99% is obtained. Finally, we note that at $r = R/\sqrt{2}$ the axial velocity component vanishes (equals the velocity of the plunger), at $r > R/\sqrt{2}$ the fluid moves toward the plunger, and at $r < R/\sqrt{2}$ it moves away from the plunger.

Example 6.14 Squeezing Flow between Two Parallel Disks This flow characterizes compression molding; it is used in certain hydrodynamic lubricating systems and in rheological testing of asphalt, rubber, and other very viscous liquids.[14] We solve the flow problem for a Power Law model fluid as suggested by Scott (48) and presented by Leider and Bird (49). We assume a quasi-steady-state "slow" flow[15] and invoke the lubrication approximation. We use a cylindrical coordinate system placed at the center and midway between the plates as shown in Fig. E6.14a.

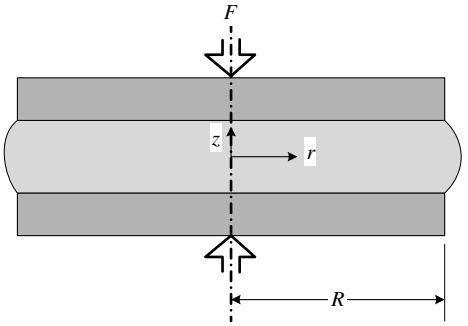

Fig. E6.14a Schematic representation of squeezing flow with a cylindrical coordinate system placed midway between the disks.

14. The Williams Plastometer, which is based on this geometry, has been used in the rubber industry for many years. [I. Williams," Plasticity and its Measurement," *Ind. Eng. Chem.*, **16**, 362–364 (1931).] More recently, Leider and Bird (49) pointed out the advantage of this simple geometry for transient nonviscometric rheological testing of polymeric melts.

15. For "fast" squeezing flow we would need a constitutive equation that accounts for the stress overshoot phenomenon.

In light of these assumptions, the Power Law model reduces to:

$$\tau_{rz} = m\left(-\frac{dv_r}{dz}\right)^n \tag{E6.14-1}$$

and the equation of continuity reduces to

$$\frac{1}{r}\frac{\partial}{\partial r}(rv_r) + \frac{\partial v_z}{\partial z} = 0 \tag{E6.14-2}$$

which can be integrated to give

$$-\dot{h}\pi r^2 = 2\pi r \int_0^h v_r \, dz \tag{E6.14-3}$$

where $\dot{h} = dh/dt$ is the instantaneous disk velocity. The r component of the equation of motion with inertial terms and normal-stress terms omitted, reduces to

$$\frac{\partial \tau_{rz}}{\partial z} = -\frac{\partial P}{\partial r} \tag{E6.14-4}$$

The time dependence of v_r is introduced through the boundary condition at $h(t)$ as given by Eq. E6.14-3, where

$$v_r(h) = 0 \tag{E6.14-5}$$

Furthermore, requirements of symmetry dictate that $\partial v_r/\partial z = 0$ or $\tau_{rz} = 0$ at $z = 0$. It follows from the simplifying assumptions that the other two components of the equation of motion reduce to $\partial P/\partial\theta = 0$ and $\partial P/\partial z = 0$, hence the pressure P is a function of r only, and Eq. E6.14-3 can be integrated with respect to z, to give:

$$\tau_{rz} = \left(-\frac{\partial P}{\partial r}\right)z \tag{E6.14-6}$$

Substituting Eq. E6.14-6 into Eq. E6.14-1 and integrating over z we obtain the velocity profile:

$$v_r = \frac{h^{1+s}}{1+s}\left(-\frac{1}{m}\frac{dP}{dr}\right)^s \left[1 - \left(\frac{z}{h}\right)^{1+s}\right] \tag{E6.14-7}$$

where $s = 1/n$. Note that this velocity profile is identical to that of a Power Law model fluid in fully developed flow between parallel plates with the local pressure gradient and instantaneous disk separation. By substituting the velocity v_r from Eq. E6.14-7 into Eq. E6.14-3, followed by integration, a differential equation for the pressure gradient is obtained in terms of the instantaneous disk velocity:

$$\frac{dP}{dr} = -m\left(\frac{2+s}{2h^{s+2}}\right)^n (-\dot{h})^n r^n \tag{E6.14-8}$$

which can be integrated to obtain the pressure profile

$$P = P_a + m\frac{(2+s)^n}{(n+1)}\frac{(-\dot{h})^n R^{1+n}}{2^n\ h^{1+2n}}\left[1-\left(\frac{r}{R}\right)^{1+n}\right] \tag{E6.14-9}$$

where P_a is the atmospheric pressure. The maximum pressure, as expected, is at the center of the disk. The total instantaneous force that must be applied to the disk to maintain the velocity $\dot{h}$ is obtained from Eq. E6.14-9 by integrating the product of the pressure and the differential surface area to give:

$$F_N = m\pi\frac{(2+s)^n}{(3+n)}\frac{(-\dot{h})^n R^{3+n}}{2^n h^{1+2n}} \tag{E6.14-10}$$

which is the Scott equation. Note that, for a Newtonian fluid, the force is proportional to the fourth power of the radius, and inversely proportional to the third power of the separation gap.

Normally we would apply a *constant* force and measure the gap separation profile. This is obtained from Eq. E6.14-10

$$\frac{h(t)}{h_0} = \left[1+\frac{2(1+s)(3+n)^s}{2+s}\left(\frac{F_N}{\pi m R^2}\right)^s\left(\frac{h_0}{R}\right)^{1+s} t\right]^{(-n)/(1+n)} \tag{E.6.14-11}$$

where $h_0 = h(0)$. Finally, the preceding equation yields the value of the "half time," that is, the time needed to reduce the gap size to half its initial value:

$$\frac{t_{1/2}}{n} = K_n\left(\frac{\pi m R^2}{F_N}\right)^s\left(\frac{R}{h_0}\right)^{1+s} \tag{E6.14-12}$$

where

$$K_N = \left(\frac{2^{1+s}-1}{2n}\right)\left(\frac{2+s}{1+s}\right)\left(\frac{1}{1+s}\right)^s \tag{E6.14-13}$$

According to the Scott equation, plotting $\ln(t_{1/2})$ versus $\ln(1/F_N)$ should give a straight line. This is what Leider (50) observed with a series of fluids in the Scott equation range. However, Leider and Bird (49) extended the analysis to include stress overshoot phenomena by using a semiempirical expression for the shear stress:

$$\tau_{rz} = m\left(-\frac{dv_r}{dz}\right)^n [1+(b\dot{\gamma}t-1)e^{-t/an\ \lambda}] \tag{E6.14-14}$$

where λ is a time constant and $\dot{\gamma}$ is the shear rate, which modifies Eq. E6.14-10 to

$$F_N = m\pi\frac{(2+s)^n}{(3+n)}\frac{(-\dot{h})^n R^{3+n}}{2^n h^{1+2n}}\left\{1+\left[\frac{(2+s)}{2^{1+s}}\left(\frac{-\dot{h}h_0^s}{h^{2+s}}\right)bt-1\right]e^{-t/an\ \lambda}\right\} \tag{E6.14-15}$$

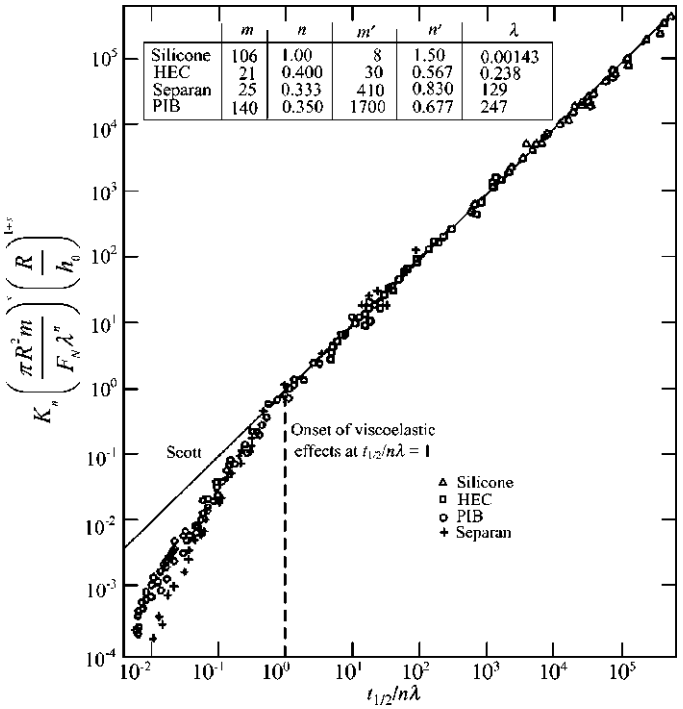

Fig. E6.14b Dimensionless plot of squeezing flow data by Leider (50) representing 181 runs for four fluids: silicone oil, 1% solution of hydroxyethyl cellulose (HEC), 0.5% solution of Separan (polyacrylamide) in glycerin, and polyisobuthylene solution. [Reprinted by permission from P. J. Leider, ''Squeezing Flow between Parallel Disks, II, Experimental Results,'' *Ind. Eng. Chem. Fundam.*, **13**, 342–346 (1974).]

Their experimental results are shown in Fig. E6.14b, which plots dimensionless half-time versus dimensionless reciprocal force. Clearly, the Scott equations describe the experimental results given earlier as $t_{1/2}/n\lambda = 1$. They recommend that the choice of the parameter λ be made on the basis of the Power Law parameters m and n and a similar Power Law relationship of the primary normal stress difference function $\Psi_1(\dot{\gamma}) = m_1\dot{\gamma}^{1/(n_1-n)}$ as follows:

$$\lambda = \left(\frac{m_1}{2m}\right)^{1/(n_1-n)} \tag{E6.14-16}$$

They also recommend the selection of parameters a and b so as to give the best fit for the stress overshoot data obtained for a constant shear-rate experiment. By following this procedure, good agreement between experiments and theory was obtained, as demonstrated in Fig. E6.14b.

Next we examine two important *continuous* positive-displacement pumps: the gear pump and the co-rotating fully intermeshing twin-screw pumps. First we show in the following Example how to convert building block 5 into a continuous intermeshing twin-screw pump.

Example 6.15 Conversion of Building Block 5 in Figure 6.2 Consisting of a Plate Moving Normal to its Plane into a Fully Intermeshing Counterrotating Twin-screw Pump

The conceptual process is a bit tortuous, but as shown in Fig. E6.15a, it is not unreasonable. In step one we wish to convert axial motion into rotary motion. This can be achieved by using by a rolling cylinder over a flat plate. Next we have the rolling cylinder move around a second solid cylinder. Then the rolling cylinder is sliced into segments and the second cylinder converted into a screw such that the rolling segments roll in the screw channel. Finally, the rolling cylinders in the screw channel can be replaced by a second intermeshing screw rotating in the opposite direction to the first screw, which will push the material forward in the same fashion, leading to a fully intermeshing twin-screw pump. Note that a 90° angle twin screw converts (conceptually) into a gear pump.

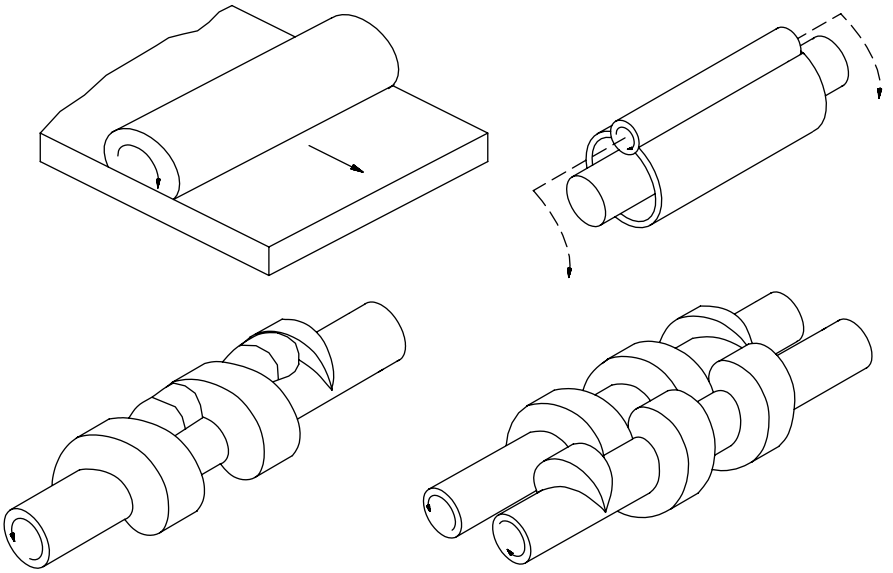

Fig. E6.15a The synthesis of the intermeshing counterrotating TSE, the gear pumps, and paddle pump from building block 5.

The gear pump [Fig. 6.37(c)] permits accurate flow-rate metering, coupled with high discharge pressure for both low and high viscosity liquids. In polymer processing, gear pumps were applied in pumping low molecular weight (low viscosity) polymers such as nylons for high-rate pelletizing after reactors of polyolefines, and as ''booster'' pumps attached to the discharge end of plasticating extruders for both raising pressure and for accurately controlling flow rate (e.g., in fiber spinning).

The principle of operation of gear pumps is simple: The melt is fed between the exposed adjacent gear teeth, and transported by the rotating gears from inlet port to the discharge port. During this time the liquid is enclosed in a small space created by the adjacent teeth, the root of the gear and the housing. The latter moves relative to the gear generating drag-induced rotational flow within the space, similar to the cross-channel circulatory flow in SSEs. There is also a small leakage flow in the clearance over the teeth.

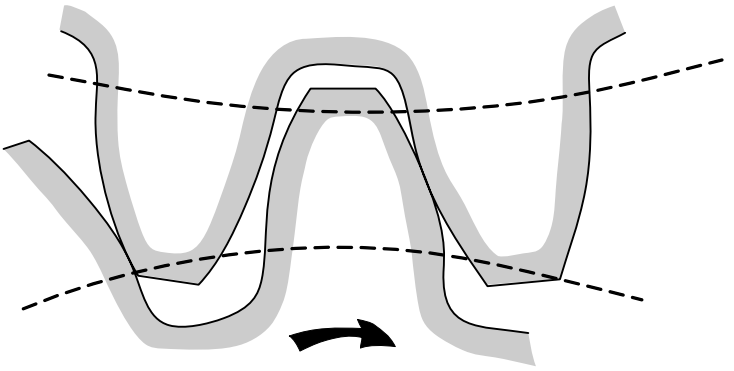

Fig. 6.38 Tooth configuration of gear pumps.

The inlet and outlet ports are sealed from each other by meshed gears. The meshing action squeezes the melt out of the discharge space. The flow is continuous, but every instant that a new set of gear teeth is exposed to the discharge space, both the pressure and flow rate are affected, and thus both oscillate slightly at a frequency proportional to gear speed times the number of teeth.

The shape of the gear is generally of the involute[16] type (Fig. 6.38). With straight-teeth gears, liquid can be trapped between the intermeshing teeth, resulting in ''backlash'' with its excessive noise and wear. With low-viscosity liquid, this problem can be relieved by positioning strategically located relief ports. Since this is not possible for polymeric melts, double helical gears are normally used, as shown in Fig. 6.39. Upon intermeshing, this geometry of teeth results in a squeezing-out action of the melt, from the center outward.

Example 6.16 The Flow Rate of a Gear Pump Ideally the displaced volume determines the flow rate of a gear pump, and it is independent of rheological properties. If the volume of

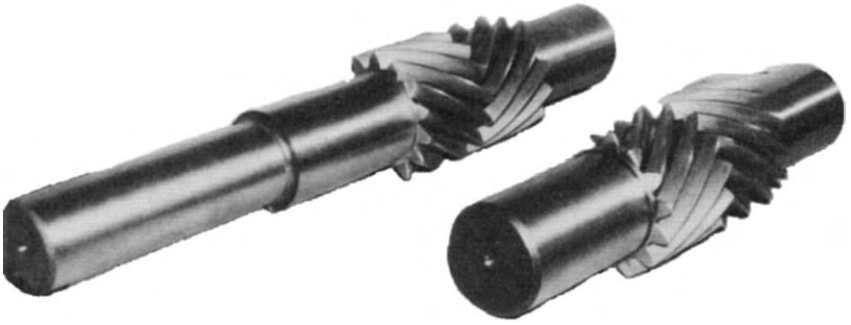

Fig. 6.39 Double helical gears. [Photograph courtesy of Farrel Corp., Ansonia, CT.]

16. Such a shape is derived from the curve obtained by the end of a string wrapped around the circumference of a stationary cylinder and being unwrapped under tension.

the space between the teeth is given by V_n, the number of teeth n, and the speed of rotation N, the volumetric flow rate Q will be given by

$$Q = V_n n N \tag{E6.16-1}$$

The die resistance at the discharge port determines the discharge pressure.

In reality, however, some leakage does occur between the teeth and the housing, and between the intermeshing gears, somewhat reducing pumping efficiency. The leakage flow is sensitive, of course, to viscosity. A full hydrodynamic analysis of gear pumps would require the evaluation of the leakage flows (51), the circulatory flow within the space between the teeth, and the squeezing flow between the meshing teeth, where the stresses on the gear teeth are affected by both the viscosity as well as non-Newtonian elastic properties of the liquid such as stress overshoot. Moreover, nonisothermal conditions should be accounted for. Yet as shown in Fig. E6.16, the theoretical flow rate is reasonably close to experimental results for very good first-order estimations.

Gear pumps are characterized by relatively high flow rates at low frequencies of rotation with low specific power consumption, but they also have a number of disadvantages. In gravitational feeding, there is an upper limit of viscosity beyond which the polymer will not fill the gears, resulting in what is called *starving*. When used downstream, low pressure-generating processing equipment, such as co-rotating intermeshing TSEs in postreactor finishing operations, the processing equipment must operate under conditions that deliver the melt to the gear-pump melt intake at a set minimum

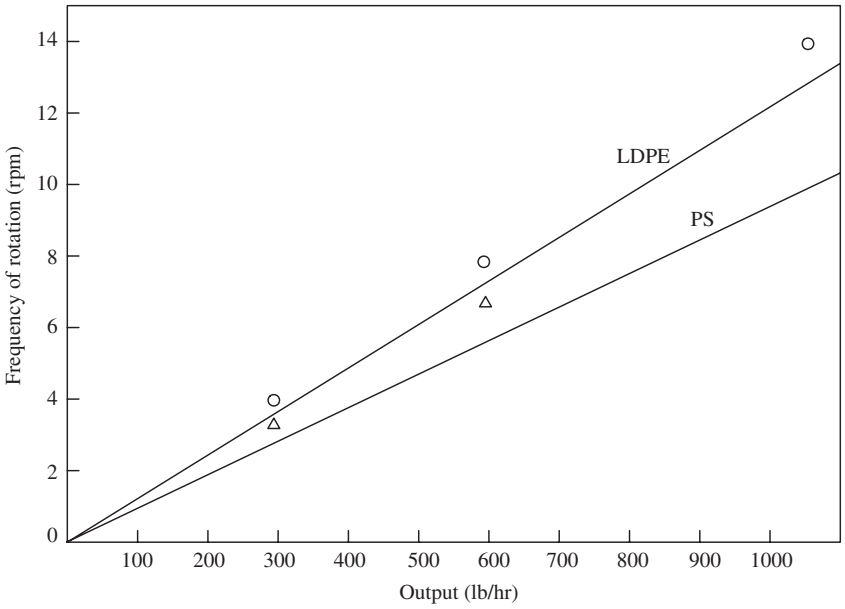

Fig. E6.16 Output versus gear frequency of rotation for a 5.6-in-diameter 4.5 in wide, double (30°) helical, 14-teeth 0.67-in-deep gear pump, and with LDPE (circles) and PS (triangles). Smooth curves are the theoretical ones at the respective densities. [Reprinted with permission from C. Y. Cheng, Farrel Corp., Ansonia, CT, private communication, 1972.]

value of the order of 100–200 psi. The other limitation is the large forces that can develop in the meshing region, which tend to separate the gears and create wear. Finally, gear pumps may not be used for thermally and shear sensitive polymers because of the numerous dead spots present.

6.8 TWIN SCREW EXTRUDER PUMPS

By placing two screws side by side to create a TSE (52–54), the number of geometrical design variables, compared to a SSE, is greatly enriched. Indeed, TSEs come in a large variety of configurations and arrangements with a wealth of patent literature. The three principal variants are shown in Fig. 6.40, and they are (a) the direction of rotation, (b) the level of intermeshing, and (c) the level of engagement. The resulting types of flow channels are shown in Fig. 6.41.

The screws can *co-rotate*, in which case the screws have helix angles in the same direction (either right-handed or left-handed), or *counterrotate*, in which case, the screws have opposite helix angles. The screws can be nonintermeshing or intermeshing, that is, the flight of one screw penetrates into the channel of the other. In the latter case, the screws can be fully or partially engaged. When fully engaged, the flight of one screw completely fills the channel of the other and the screws are "self-wiping." Depending on the geometry of the screw of a corotating fully intermeshing twin screw, as shown in Fig. 6.41, the channel may be continuous, with a smooth transition from the channel of one screw to that

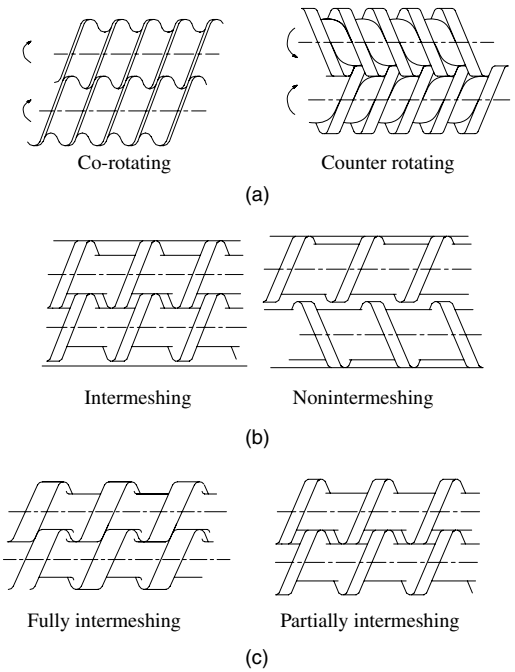

Fig. 6.40 Classification of TSEs systems. [Reproduced by permission from J. F. Agassant, P. Avenas, J.-Ph. Sergent, B. Vergnes, and M. Vincent, *La Mise en Forme Des Matières Plastiques, Technique et Documentation*, Third Edition, Technique & Documentation, Paris, 1996].

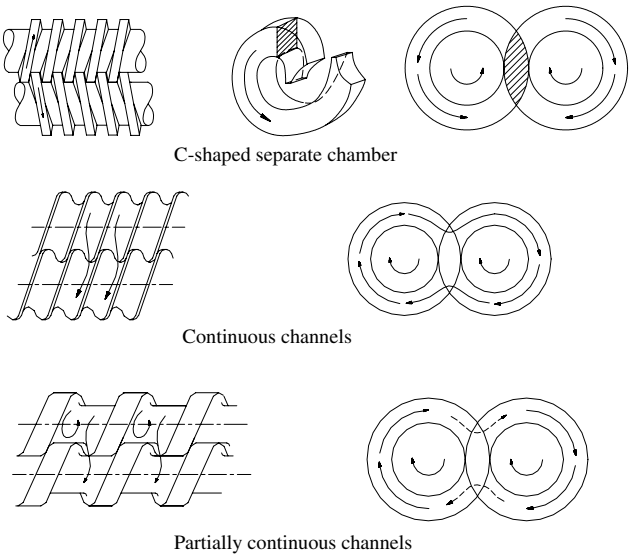

Fig. 6.41 Different types of TSE flow channels. [Reproduced by permission from J. F. Agassant, P. Avenas, J.-Ph. Sergent, B. Vergnes, and M. Vincent, *La Mise en Forme Des Matiéres Plastiques, Technique et Documentation*, Third Edition, Technique & Documentation, Paris, 1996].

of the other, or partially continuous, with the flight width partially blocking the passage from the channel of one screw to that of the other.

The fully intermeshing Co-TSEs are used extensively in all applications where mild to intensive compounding must be done. These machines are constructed with multiple-section screws,[17] each having different geometrical designs, and with self-wiping kneading blocks. In the case of counterrotating fully intermeshing TSEs, the channel of one screw is completely blocked by the other, creating isolated channel segments. This positive displacement type of TSE, which has good plasticating capability at low specific energy consumption, sometimes uses conical screws to reduce the size of the isolated chamber space as it moves from entrance to exit. In addition, screws can be single or multiflighted. Screws do not have to be of equal size (in which case, for intermeshing screws they rotate at different speeds), though in all practical cases they are. Finally, there may be more than two screws, but these will be not discussed here. Clearly, the number of available geometrical design variables greatly exceeds those of most other processing machines.

This rich variety of design solutions, with their complex geometrical features, implies the need for a complementary, rich arsenal of theoretical analyses. Such a resource has never been created and only the most prevalent types of machines have been analyzed in reasonable detail. Among these are the co-rotating fully intermeshing TSEs, the counterrotating fully intermeshing TSEs, and the tangential nonintermeshing TSEs.

Pumping and pressurization in these three configurations are analyzed next.

17. The screw segments (elements) are assembled on keyed shafts.

The Co-rotating Intermeshing Screw Pump

The pumping mechanism of the co-rotating intermeshing twin screw is drag-induced flow, much like that of the SSE based on building block 1 in Fig. 6.2. Its main advantage is its self-wiping surfaces, including the flights and root of the screw, which eliminate dead spots, while its disadvantages include higher machining costs due to the tight clearances, and some limitation on power inputs due to the proximity of the axes of the two screws.

First, we discuss the geometry of the co-rotating intermeshing twin screw, which was studied in detail by Booy (56), who derived the relevant geometrical relationships. Consider a section perpendicular to the axes of the screws as shown in Fig. 6.42 for single-, double-, and triple-flighted screws, with the detailed geometrical variables of double-flighted screws shown in Fig. 6.43.

The cross section, fulfilling the requirement of self-wiping, has a *unique shape* determined by only three variables: the diameter, $2R_s$, the centerline distance, C_L, and the number of tips or parallel flights, n. The whole screw can be viewed as the axial assembly of an infinite number of infinitely thin slices of screws slightly rotated relative to each other, with each pair fully wiping each other. Hence, for the geometrical definitions of any screw section, it is sufficient to study the geometry of a single pair.

The angle ψ bounding the interpenetrating region, as shown in Fig. 6.43, is given by

$$\cos \psi = \frac{C_L/2}{R_s} = \rho_c/2 \tag{6.8-1}$$

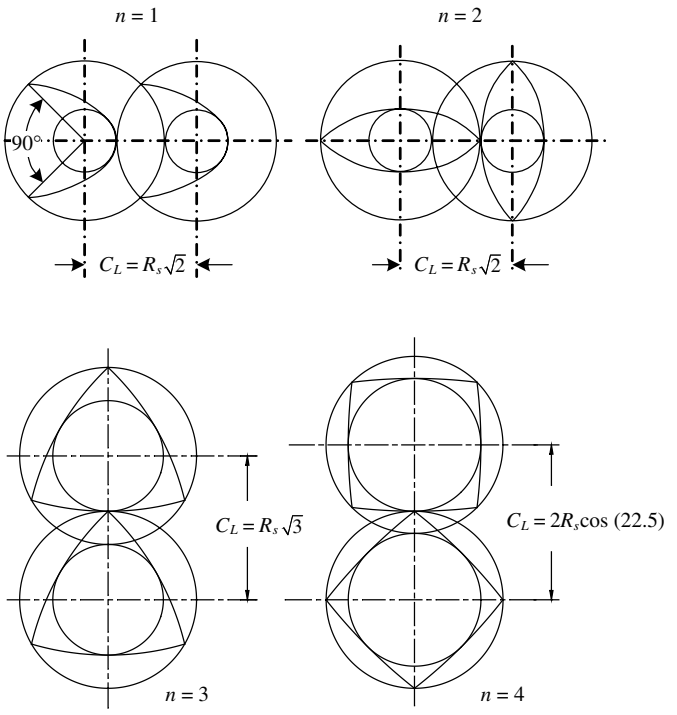

Fig. 6.42 Schematic cross sections of co-rotating fully intermeshing twin screws for single-, double-, triple-, and quadrupled-flighted screws. [Reprinted by permission from M. L. Booy, "Geometry of Fully Wiped Twin-Screw Equipment" *Polym. Eng. Sci.*, **18**, 973 (1978).]

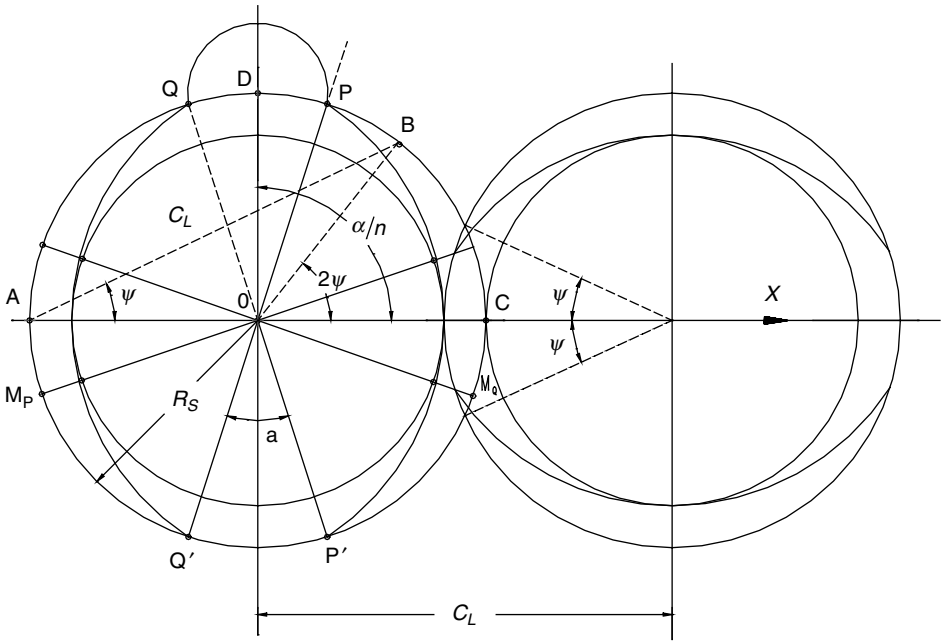

Fig. 6.43 Geometrical parameters of a co-rotating fully intermeshing double-flighted twin screw. [Reprinted by permission from M. L. Booy, ''Geometry of Fully Wiped Twin-Screw Equipment'' *Polym. Eng. Sci.*, **18**, 973 (1978).]

where the dimensionless parameter ρ_c is the ratio of centerline distance to the barrel radius. The angle defining the width of the flight tip α is related to angle ψ by the following relationship

$$\alpha = \frac{\pi}{n} - 2\psi \tag{6.8-2}$$

Thus for double-channel screws, $n = 2$, Eq. 6.8-2 shows that a ψ value of $\pi/4$ yields a zero tip angle, $\alpha = 0$, and from Eq. 6.8-1 $\rho_c = \sqrt{2}$. Similarly, for a triple flighted screw $\alpha = 0$ and $\rho_c = \sqrt{3}$ at $\psi = \pi/6$. Smaller ψ angles or larger ρ_c lead to larger tip angles α.

The channel-depth profile is shown in Fig. 6.44. Between points B_1 and B_2 over an angle equaling the tip of flight α, the channel depth is constant and has a maximum value of $H = 2R_s - C_L$; between points A and P, namely, over the tip of the flight, the channel depth is zero (i.e., equals the radial clearance that is neglected in this analysis). Between points B and A the channel depth varies with the angle γ as follows:

$$H(\gamma) = R_s(1 + \cos\gamma) - \sqrt{C_L^2 - R_s^2 \sin^2\gamma} \tag{6.8-3}$$

We note that the channel depth at any angle γ remains constant in the down-channel direction.

The area of the barrel cross section A_{bc} and the area of the screw cross section A_s, are, respectively,

$$A_{bc} = 2(\pi - \psi)R_s^2 + C_L R_s \sin\psi \tag{6.8-4}$$

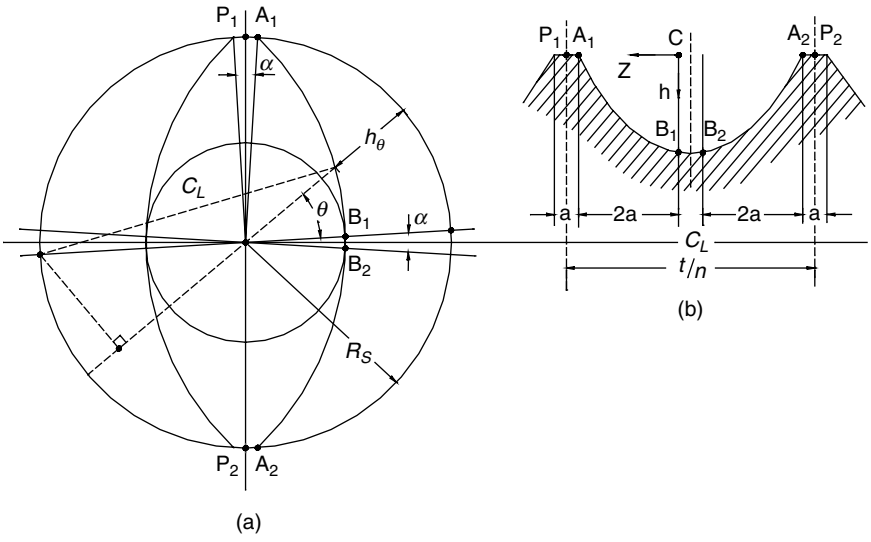

Fig. 6.44 The channel-depth profile (a) in a cross section normal to the axis, and (b) an axial cross section. [Reprinted by permission from M. L. Booy, "Geometry of Fully Wiped Twin Screw Equipment" *Polym. Eng. Sci.*, **18**, 973 (1978).]

and

$$A_s = n(\psi C_L^2 - C_L R_s \sin\psi) = \frac{1}{2} n\alpha[R_s^2 - (C_L - R_s)^2] \tag{6.8-5}$$

The free cross-sectional area, A_f, between screws and barrel is

$$A_f = A_{bc} - A_s \tag{6.8-6}$$

and the free volume between screws and barrel V_f is

$$V_f = A_f L \tag{6.8-7}$$

where L is the axial length of the extruder. The mean residence time is obtained by dividing free volume by the volumetric flow rate.

As in single screw geometry, the helix θ, is given by

$$\tan\theta = \frac{B}{2\pi r} \tag{6.8-8}$$

where r is the radial position, and B is the lead. The channel width is given by

$$W = \frac{B\cos\theta}{n} - e \tag{6.8-9}$$

where e is the flight width perpendicular to the down-channel direction; it is given by

$$e = \alpha R_s \sin\theta \tag{6.8-10}$$

In SSEs the number of parallel channels equals the number of parallel flights. In a TSE the number of parallel channels is larger than the number of flights. For example, as

indicated in Fig. 6.42, for double-flighted screws we obtain three parallel channels. In general the number of parallel channels, m, is given by

$$m = 2n - 1 + \frac{\alpha n}{\pi} \tag{6.8-11}$$

but since α is small, the number of parallel channels can be well approximated by $m = 2n - 1$.

Figures 6.45(a) and 6.45(b) show schematically the cross section of a double-flighted screw configuration with the three parallel channels, and the flattened unwound screws showing the markings of the flight tips, with corresponding points T and A marked on both. At the particular cross section shown, Channel 1 is confined to Screw 1, Channel 3 is partly in Screw 1 and partly in Screw 2, and Channel 2 is confined to Screw 2. Figure 6.45(b) also shows the passage of the material from the channels of Screw 1 to those of Screw 2 and back again. Thus, the streakline described by a fluid particle is a spiral within the helical channel of Screw 1, passing to similar spiral motion in the helical channel of Screw 2. At closed discharge, at the axial location shown in the figure, in Channels 1 and 2 fluid particles will be circulating in the C-shaped planes of each screw, and in Channel 3 they will be circulating between the two screws in the plane shown.

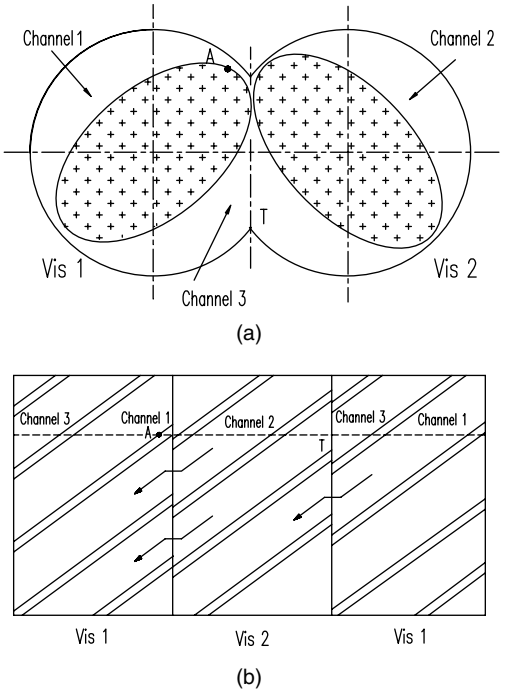

Fig. 6.45 (a) Schematic view of a double-flighted screw identifying the three parallel channels; (b) a section of the flattened unwound screws with the markings of the flight tips. The figure shows a short section of Screw 1 connecting to Screw 2 and back to Screw 1. [Reproduced by permission from J. F. Agassant, P. Avenas, J. Ph. Sergent, B. Vergnes, and M. Vincent, *La Mise en Forme Des Matières Plastiques, Technique et Documentation*, Third Edition, Technique & Documentation, Paris, 1996.]

We also notice in Fig. 6.45(b) that for small values, the transition from one screw to the next is smooth, creating an almost continuous flow; whereas for larger α values, the flight of the ''other'' screw creates an obstruction to flow.

Newtonian flow models for fully filled elements were developed by several authors (57–61). Here we derive the simplest isothermal Newtonian model for calculating the flow rate in a channel, which is identical to that of SSEs, as discussed in detail in Section 6.3. The volumetric flow rate in each channel is $Q_{ch} = Q/m$, where Q is the total volumetric flow rate.

Thus, considering a channel of length L_c, width W, and height H, the flow rate Q_{ch} is given by

$$Q_{ch} = \frac{1}{2} V_{bz} WH - \frac{WH^3}{12\mu} \frac{\Delta P_c}{L_c} \tag{6.8-12}$$

where ΔP_c is the pressure rise over length L_c, and V_{bz} is the down-channel velocity of the barrel surface relative to the screw:

$$V_{bz} = V_b \cos\theta = 2\pi N R_s \cos\theta \tag{6.8-13}$$

Now it is clear that the drag- and pressure-flow components need to be multiplied by appropriate shape factors.[18] The total pressure rise, ΔP_t, depends on its length L_t:

$$\Delta P_t = \Delta P_c \frac{L}{L_c} \left(1 - \frac{\psi}{\pi}\right) \tag{6.8-14}$$

where the factor $1 - \psi/\pi$ was introduced to account for the fact that, in the transition space between the screws, drag flow vanishes because of the opposing motion of the other screw.

The Counterrotating Intermeshing Screw Pump

An excellent historical review and applications of this type of extruder were produced by White (53), and the flow was modeled by Janssen et al. (62) and Wyman (63), whose derivation we follow. The easiest way to visualize the conveying mechanism of a counterrotating intermeshing TSE is to place a robot ''viewer'' into the screw channel at point 0 in Fig. 6.37(d) and let it report its observations. We first stop the rotation of the screws and tell our viewer to explore the space around it. It will report that the space is entirely confined by steel walls: the barrel surface from above, the flights of screw A at either side, and the intermeshing flight of screw B both up-channel and down-channel. The space is a helically distorted C-shaped channel that can be shown schematically, as in Fig. 6.46, or by molding silicone rubber into the space in Fig. 6.47. Clearly, by fully

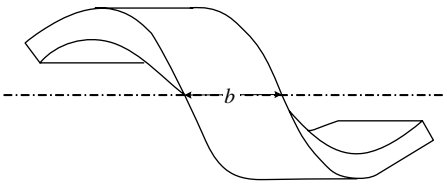

Fig. 6.46 The three-dimensional schematic view of the channel segments formed by two counterrotating intermeshing twin screws.

18. See Table 10.8.

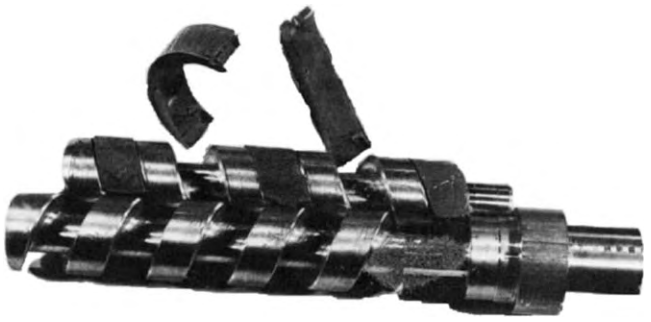

Fig. 6.47 Two intermeshing screws with the channel segments of one of the screws filled with silicone rubber, reproducing the shape of the channel segments. Two segments are pulled out, one retaining the original curved shape and the other flattened out into a trapezoidal channel.

meshing two mirror-image screws, both screw channels are subdivided into short helical segments. We next derive simple mathematical models for the flow rate and velocity profiles within the chambers.

Unlike in drag-induced flows, where we compute the flow rate from the velocity profiles, in this case, because of the positive displacement nature of the flow, we could easily relate flow rate to the axial motion of the closed chambers. But in order to understand the nature of the flow inside the chamber, for mixing and power consumption we do need to derive the detailed velocity profiles.

What happens when the screws start to rotate? The robot viewer will report that all the walls of the confined space began moving, but if it moves axially with velocity:

$$V_l = L_s N \tag{6.8-15}$$

where L_s is the lead shown in Fig. 6.37(d), and N is the frequency of screw rotation, the walls are moving parallel to their surface and it can maintain a fixed position relative to the wall. Thus, the whole compartment is transported at constant axial velocity toward the die. From this *Lagrangian* point of view, the barrel surface will be moving with velocity V_l in the opposite direction, and the root of the screw in the *up-channel helical direction* with velocity,

$$V_s = NZ_s \tag{6.8-16}$$

where Z_s is the helical length of one full turn on the root of the screw, given by

$$Z_s = \frac{L_s}{\sin\theta_s} \tag{6.8-17}$$

where θ_s is the helix angle on the root of the screw. From these equation we get

$$V_s = \frac{V_l}{\sin\theta_s} \tag{6.8-18}$$

The flights are, of course, also moving in the same direction as the root of the screw.

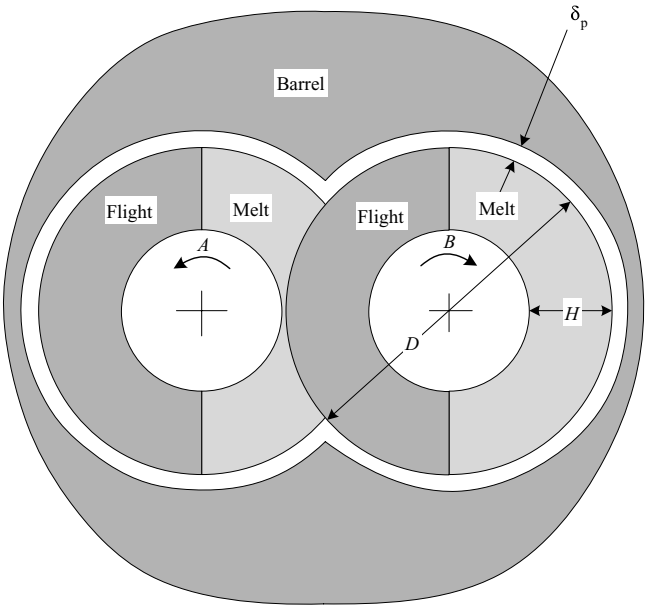

Fig. 6.48 Schematic view of the cross section of an intermeshing counterrotating TSE.

Now that the physical configuration has been clarified, we can consider in detail the mathematical model for the process. First, we find a relationship between the flow rate and the geometrical and operational variables. Neglecting leakage flow between the screws, as well as that between the screws and the barrel, this is simply given by multiplying the velocity V_l with the cross-sectional area of the melt-filled channel, A_m, as shown in Fig. 6.48

$$Q = V_l\, A_m \tag{6.8-19}$$

For single-flighted screws, A_m (indicated in Fig. 6.48 by the dotted area) equals the full cross-sectional area of the annular space between the root of one screw $\pi(D_f - H)H$ less the area corresponding to the overlap of the flanks of the flights. Thus neglecting flight clearance, we get

$$A_m = \pi(D_f - H)H - \frac{D_f^2}{2}\cos^{-1}\left(1 - \frac{H}{D_f}\right) + \frac{D_f - H}{2}\sqrt{H(2D_f - H)} \tag{6.8-20}$$

The volumetric flow rate (both screws) is given by

$$Q = \pi N \bar{D} L_s H\left[1 - \frac{1}{2\pi}\left(\frac{D_f}{\bar{D}}\right)\left(\frac{D_f}{H}\right)\cos^{-1}\left(1 - \frac{H}{D_f}\right) + \frac{1}{2\pi}\left(\frac{D_f}{D}\right)\left(1 - \frac{H}{D_f}\right)\sqrt{\frac{2D_f}{H} - 1}\right] \tag{6.8-21}$$

where $\bar{D} = D_f - H$ is the mean diameter. The actual flow rate is less than the theoretical value because of leakage flows between chambers. Specifically, there are leakage flows

between the screw flights and the barrel, between the tips of flights of one screw and the root of the second screw, and between the flanks of the flights. These leakage flows were calculated by Janssen et al. (62,64–67), who also carried out experiments with Newtonian fluids, confirming their theoretical model, and by Klenk (68–70) and Doboczky (71,72). Power consumption in twin-screw geometry is given by Schenkel (6), who also analyzes the various twin screws and compares their action to single-screw pumps.

We now develop a simple model, termed the *plate-and-frame* model, which approximates the flow patterns inside the chamber. Since the chambers move at constant axial velocity given by Eq. 6.8-15, from a *Lagrangian* point of view, that is, from the point of view of an observer moving axially at this velocity, the channel walls appear at fixed position and the velocity profile within the chamber can be assumed as being at steady state. Assuming relatively shallow channels, we unwind the channel and flatten it out, as shown in Fig. 6.49. We note the surface of the barrel, which moves at velocity V_l in the direction opposite to the forward axial direction, and the root of the screw, which moves at velocity V_s in the upstream helical direction. The flights, of course, move together with the root of the screw. The blocking screw rotates with a tangential velocity $\pi N D_s$. The end result of the simplified model is as follows: The flights and the cylinders (screw B) form a parallelepiped frame. The "frame" is placed within two infinite plates: the surface of the barrel and the root of the screw. Figure 6.50 depicts top and side views of this plate-and-frame model. Each retaining surface moves parallel to its plane, as pointed out earlier and shown in the figure.

The velocity of the barrel surface can be broken down into two components: down-channel $V_l \sin\theta_b$ and cross-channel $V_l \cos\theta_b$ toward the "pushing" flight. The screw velocity is the vectorial sum of two components: the tangential velocity of the root of the screw $\pi N D_s$ and the velocity of the barrel or the viewer V_l. Finally, Fig. 6.50(b) gives the first hint of the nature of the flow pattern in the chamber. We note that both the screw and the barrel drag melt toward the pushing screw. Neglecting end effects and assuming that the net flow rate is zero (no leakage), the shape of the velocity profile in the down-channel direction (v_z) must assume a shape as indicated in Fig. 6.50(b). This also implies a pressure buildup against the pushing screw.

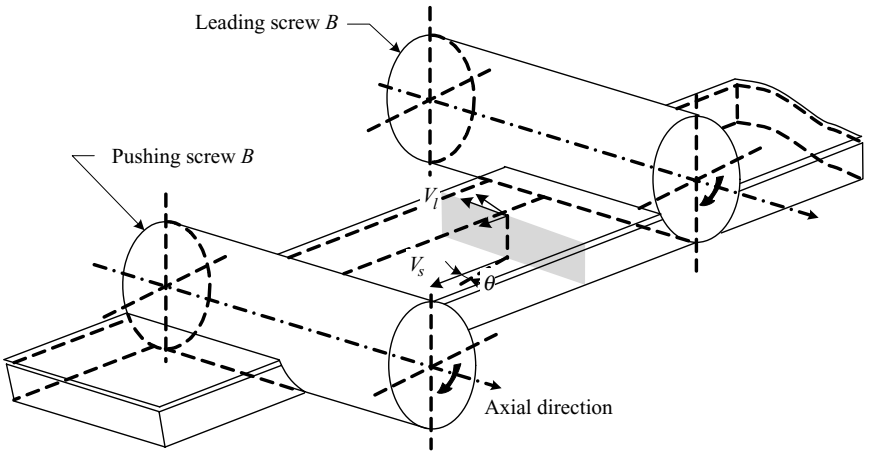

Fig. 6.49 The unwound helical channel segment forming a single chamber of the counterrotating twin screw.

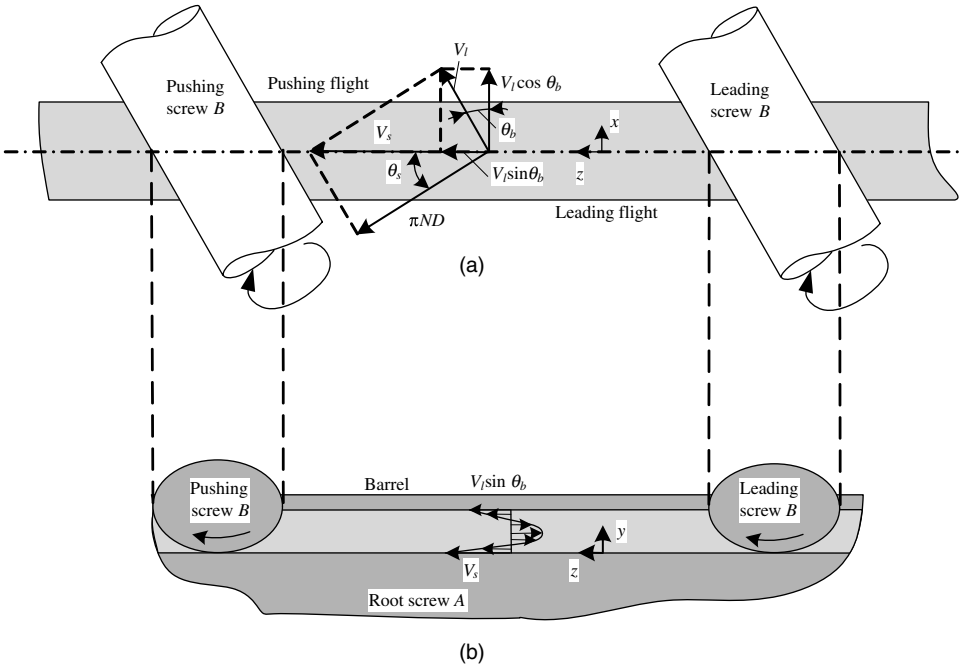

Fig. 6.50 (a) Top, and (b) side views of the unwound channel shown in Fig. 6.49.

We next derive the exact velocity profile, assuming steady, laminar, isothermal, and fully developed flow without slip at the walls, of an incompressible Newtonian fluid. The equation of continuity reduces to

$$\frac{\partial v_y}{\partial y} = 0 \tag{6.8-22}$$

which upon integration yields $v_y =$ constant; but since v_y vanishes at either plate, it must vanish everywhere. Thus, we find that $v_y = 0$. The velocity components that are left in the equation of motion are $v_z(y)$ and $v_x(y)$. The equation of motion reduces to

$$\frac{\partial P}{\partial x} = \mu \frac{\partial^2 v_x}{\partial y^2} \tag{6.8-23}$$

and

$$\frac{\partial P}{\partial z} = \frac{\partial^2 v_z}{\partial y^2} \tag{6.8-24}$$

with boundary conditions

$$v_x(0) = 0 \tag{6.8-25}$$
$$v_x(H) = V_l \cos \theta_b \tag{6.8-26}$$
$$v_z(0) = V_s \tag{6.8-27}$$
$$v_z(H) = V_l \sin \theta_b \tag{6.8-28}$$

The y component of the equation of motion indicates that $P \neq f(y)$; thus, Eqs. 6.8-23 and 6.8-24, with the preceding boundary conditions, can be integrated to give the required velocity profiles

$$v_x = V_l \cos\theta_b \xi + \xi(\xi - 1)\left(\frac{H^2}{2\mu}\frac{\partial P}{\partial x}\right) \tag{6.8-29}$$

and

$$v_z = (V_l \sin\theta_b - V_s)\xi + \xi(\xi - 1)\left(\frac{H^2}{2\mu}\frac{\partial P}{\partial z}\right) + V_s \tag{6.8-30}$$

where H is the channel depth. By assuming zero net flow rate in both directions (no leakage), we integrate the velocity profiles to obtain the following expression for the pressure gradients:

$$\frac{\partial P}{\partial x} = \frac{6\mu V_l \cos\theta_b}{H^2} \tag{6.8-31}$$

and

$$\frac{\partial P}{\partial z} = \frac{6\mu(V_l \sin\theta_b + V_s)}{H^2} \tag{6.8-32}$$

Thus, as in SSEs, the pressure rises linearly in the directions of the pushing flight and pushing screw, reaching a maximum at the corner between them. However, the absolute pressure cannot be determined from the model unless the chamber is partially empty, where the pressure can be assumed atmospheric. Otherwise, the leakage flow must be considered and the pressure profile along the screw determined.

By substituting Eqs. 6.8-31 and 6.8-32 into Eqs. 6.8-29 and 6.8-30, respectively, we obtain

$$\frac{v_x}{V_l \cos\theta_b} = \xi(3\xi - 2) \tag{6.8-33}$$

and

$$\frac{v_z}{V_l \sin\theta_b} = \xi(3\xi - 2) + \frac{V_s}{V_l \sin\theta_b}(1 - 4\xi + \xi^2) \tag{6.8-34}$$

Figure 6.51 shows the velocity profiles for square pitched screws ($\theta = 17.65^\circ$), with $V_l \sin\theta_b = 1$. The velocity profiles reveal intense internal circulation, whereby melt is dragged by the root of the screw toward the pushing screw in the lower portion of the channel, while it flows in the opposite direction (opposing the motion of the barrel surface) in the upper portion of the channel. At the same time, there is also circulatory flow in the channel width direction where in the upper part of the channel, the melt is dragged by the barrel surface toward the pushing flights and flows back in the lower portion of the channel. The interaction of the two velocity profiles eliminates the possibility of any stagnant layers.

The paths described by the fluid particles will depend on their initial location and will be quite complex. In principle, these paths can be calculated from the velocity profiles and

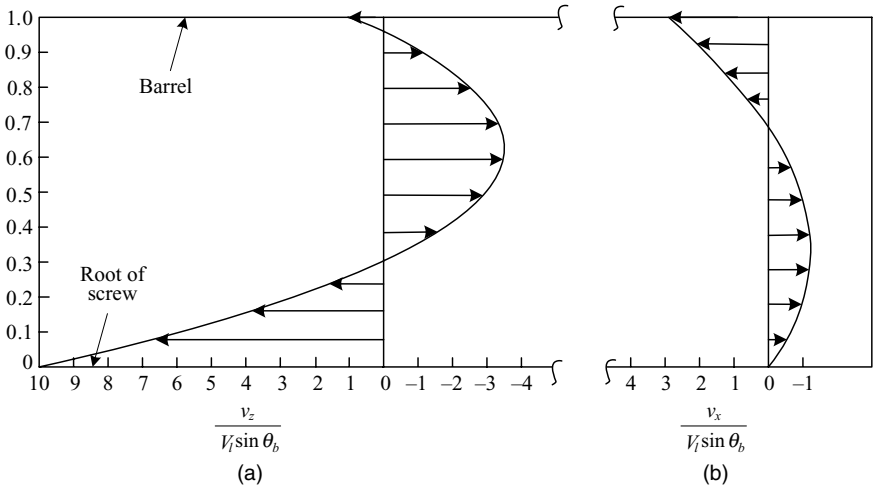

Fig. 6.51 Velocity profiles in the (a) down-channel and (b) cross-channel directions, assuming a square pitched screw. Basis: $V_l \sin\theta_b = 1$, $V_s/(V_l \sin\theta_b) = 1/\sin\theta_s \sin\theta_b \cong 10$, $v_x(1)/V_l \sin\theta_b) = v_x(1)/(V_l \cos\theta_b)(\cos\theta_b/\sin\theta_b) \cong v_x(1)/(V_l \cos\theta_b) \cong 3.13$.

they are expected to have the shape of open-loop helices. The situation is somewhat more complicated in the neighborhood of the nips (Fig. 6.52). Near the pushing flight, both the pushing screw and the root of the screw *A* drag melt toward the nip. This results in intensive mixing with both high rates and high stresses. The opposite effect occurs at the trailing screw. We discuss the nip regions in Chapter 10.

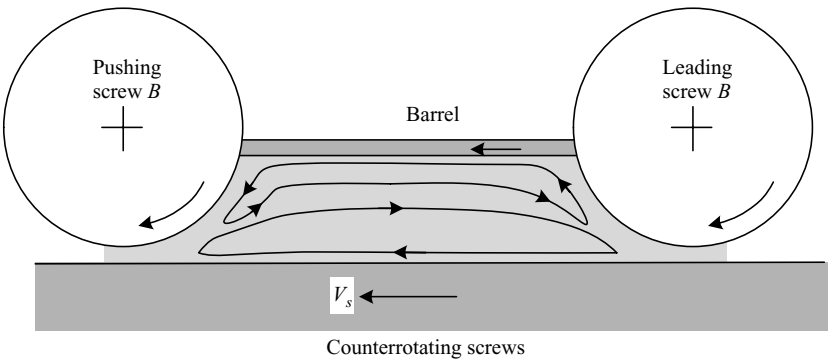

Fig. 6.52 Schematic representation of the streamlines in the neighborhood of the "nips."

The Tangential Nonintermeshing Twin-screw Pump

This TSE consists of two parallel counterrotating screws, as shown in Fig. 6.53. The distance between the screw centers is $L < D_b$, where D_b is the barrel diameter; thus, there is an open axial slit along the barrel. This type of extruder has advantages for the feeding of particulate solids (e.g., powder), venting, and devolatilization of the molten polymer.

Kaplan and Tadmor (74) proposed a mathematical model for isothermal pumping in this extruder for Newtonian fluids, which they termed "the three plate model." We follow that

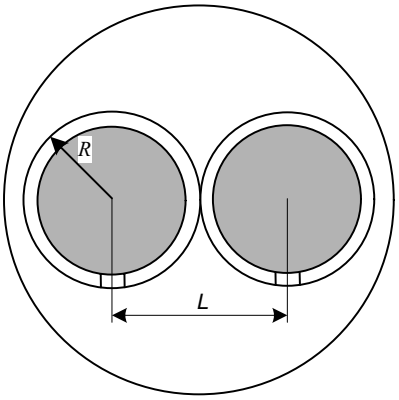

Fig. 6.53 Cross-sectional view of the twin-screw extruder. L is the distance between the centers of the screws and $D_b = 2R$ is the barrel diameter.

model and assume that the screws have identical frequencies of rotation and are positioned such that their respective flights oppose each other. The flow conditions in the channels of both screws are identical, and therefore, solving for one provides a complete solution.

As in single screw analysis, we assume that one screw is stationary while the barrel (with the other screw) is rotating in the opposite direction at the same frequency of rotation. A viewer ''riding'' on a fluid particle in the stationary screw channel will observe the root of the screw below and the screw flights on either side or the barrel above. The barrel surface, however, is not a smooth continuous surface like it is in a single screw pump, but at every turn of the barrel a slit passes by. Through the slit, the observer will see the other rotating screw. For shallow channels, we unwind the screw channel and place it on a rectangular coordinate system with the slitted barrel, as shown in Fig. 6.54.

A cross section perpendicular to the root of the screw and parallel to the flights is shown in Fig. 6.55, where the other screw across the slit is shown. Clearly, the two screws move at the same velocity in the same direction; therefore, they will appear to each other as stationary. Thus, neglecting curvature and flight effects, the model simplifies to a three–parallel plate model, as shown in Fig. 6.56, with the lower and upper plates representing

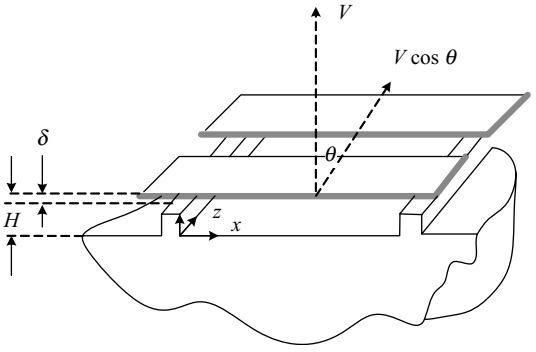

Fig. 6.54 The geometry of the unwound channel with the slitted barrel moving at velocity V_b and V_{bz} in the down-channel direction.

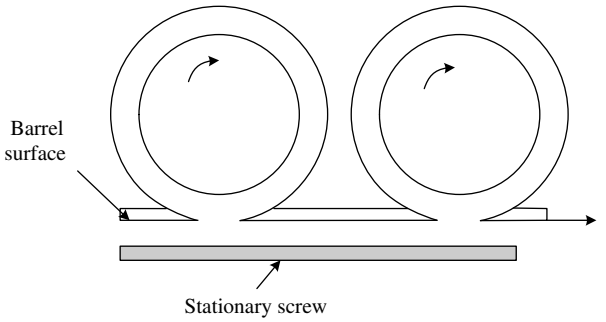

Fig. 6.55 A down-channel cross-sectional view of the unwound channel.

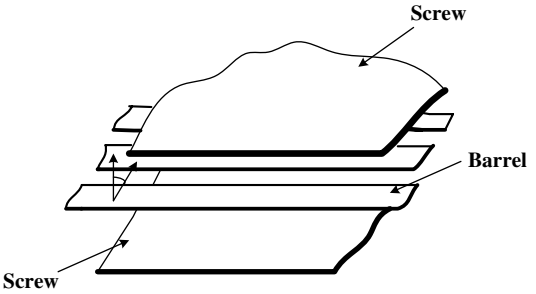

Fig. 6.56 The three-parallel plate model. The upper and lower stationary plates represent the screws, and the slitted midplate is the barrel surface.

the two screws, which are stationary, and the moving central slitted plate representing for both screws the barrel surface. The velocity of the slitted barrel is $V_b = \pi N D_b$ at an angle θ (the helix angle) to the down-channel direction, z. The slits in the barrel are perpendicular to the direction of movement.

Now, for convenience, we assume that the barrel surface is stationary and that the upper and lower plates representing the screws move in the opposite direction, as shown in Fig. 6.57, but for flow rate calculations, it is the material retained on the barrel rather than that dragged by the screw that leaves the extruder. We assume laminar, isothermal, steady, fully developed flow without slip on the walls of an incompressible Newtonian fluid. We distinguish two flow regions marked in Fig. 6.57 as Zone I and Zone II. In the former, the flow is between two parallel plates with one plate moving at constant velocity relative to

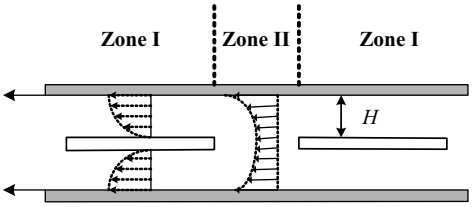

Fig. 6.57 Schematic representation of the velocity profiles in Zones II and I. Note that in Zone I pressure is built up due to drag flow between screw and barrel, whereas, in Zone II pressure is lost due to the pure pressure flow.

the other, and pressure can be generated as in single-screw extrusion. In Zone II, the flow is pressure-driven between two parallel plates and pressure drops.

The velocity profile in Zone I, with the boundary conditions $v_z(0) = 0$ and $v_z(H) = -V_{bz}$ is

$$v_z = \frac{1}{2\mu}\left(\frac{\partial P}{\partial z}\right)y^2 - \left[\frac{1}{2\mu}\left(\frac{\partial P}{\partial z}\right)H + \frac{V_{bz}}{H}\right]y \tag{6.8-35}$$

where H is the channel depth in Zone I. The velocity profile in this zone relative to a stationary screw is

$$v_z' = v_z + V_{bz} \tag{6.8-36}$$

and the flow rate Q delivered by one of the screws is obtained by integrating Eq. 6.8-36, subsequent to inserting Eq. 6.8-35 into Eq 6.8-36

$$Q = \frac{1}{2}V_{bz}HW - \frac{H^3W}{12\mu}\left(\frac{\partial P}{\partial z}\right) \tag{6.8-37}$$

Equation 6.8-37 expresses the flow rate in Zone I as a function of the pressure gradient in this zone, and is identical to the single-screw theory.

The pressure rise (or drop) in this Zone ΔP_1 is obtained from Eq. 6.8-37

$$\Delta P_1 = \frac{12\mu}{WH^3}\left(\frac{1}{2}V_{bz}WH - Q\right)\Delta z_1 \tag{6.8-38}$$

where Δz_1 is the helical length of the channel screw from the end of the slit in the barrel to the beginning of the next one. Clearly, if the drag flow rate is higher than the net flow rate, pressure will rise in the down-channel direction.

In Zone II, the velocity profile with boundary conditions $v_z(H) = -V_{bz}$ and $(\partial v_z/\partial y)_{y=0} = 0$ is

$$v_z = \frac{y^2 - H^2}{2\mu}\left(\frac{\partial P}{\partial z}\right) - V_{bz} \tag{6.8-39}$$

The velocity profile relative to stationary screws is given by Eq. 6.8-36 and, integrating it subsequent to substituting Eq. 6.8-39, gives the flow rate *per screw* as

$$Q = -\frac{wH^3}{3\mu}\left(\frac{\partial P}{\partial z}\right) \tag{6.8-40}$$

Clearly, positive flow rate requires a negative pressure gradient, that is, a pressure drop or pressure loss. The pressure drop is given by

$$\Delta P_2 = -\frac{3\mu Q}{WH^3}\Delta z_2 \tag{6.8-41}$$

where Δz_2 is the helical length of the screw channel in the slitted zone.

The total pressure change along one full turn is the sum of Eqs. 6.8-38 and 6.8-41

$$\Delta P_t = \frac{6\mu}{H^2} V_{bz} \Delta z_1 - \frac{3\mu Q}{WH^3}(4\Delta z_1 - \Delta z_2) \tag{6.8-42}$$

which can be written in terms of the fraction of the down-channel length without a slit on the barrel $f = \Delta z_1 / \Delta z_t$ to give

$$\frac{\Delta P_t}{\Delta z_t} = \frac{6\mu V_{bz}}{H^2} f - \frac{3\mu Q}{WH^3}(1 + 3f) \tag{6.8-43}$$

Finally, from Eq. 6.8-44 the flow rate per screw, Q, can be expressed as

$$Q = \frac{1}{2} WHV_{bz} F_{DTW} - \frac{WH^3}{12\mu}\left(\frac{\Delta P_t}{\Delta z_t}\right) F_{PTW} \tag{6.8-44}$$

where

$$F_{DTW} = \frac{4f}{1 + 3f} \tag{6.8-45}$$

$$F_{PTW} = \frac{4}{1 + 3f} \tag{6.8-46}$$

which is the single screw model with appropriate correction factors for the effect of the slit. Since $f < 1$, the drag-flow term is reduced because of the loss in drag in the slitted area, and the pressure-flow term is increased because of the larger gap in the slitted section. For $f = 1$, Eq. 6.8-46 converges, as it should to the single-screw parallel-plate model.

Kaplan and Tadmor (73) expanded the model to include leakage flow effects, considered non-Newtonian fluids, and verified the model experimentally with a polyisobutylene. We discuss the flow further in a tangential, nonintermeshing TSE in Chapter 10.

REFERENCES

1. Z. Tadmor, "The Synthesis of Polymer Processing Machines," *Int. Polym. Process.*, **5**, 1–14 (1990).
2. Z. Tadmor, "Machine Invention, Innovation and Elementary Steps," *Adv. Polym. Technol.*, **21**, 87–97 (2002).
3. F. Reuleaux, *Cinématique*, "Principales d'une Théorie Générale des Machines," Libraire F. Savy, Paris, 1877.
4. H. A. Simon, *The Science of the Artificial*, MIT Press, Cambridge, MA, 1969.
5. V. Hubka, *Principles of Engineering Design*, Butterworth, Boston, 1982.
6. G. Schenkel, *Plastics Extrusion Technology and Theory*, Illife Books, London, 1966.
7. G. Schenkel, "Trends and Highlights in Polymer Processing 1938–1988," *Int. Polym. Process.*, **3**, 3 (1988).

8. I. Asimov, *Asimov's Biographical Encyclopedia of Science and Technology*, Avon Books, New York, 1976.
9. Z. Tadmor, ''Method for Processing Polymeric Materials,'' U.S. Patent 4,142,805, and ''Method and Apparatus for Processing Polymeric Materials,'' U.S. Patent 4,194,841.
10. Z. Tadmor, P. Hold, and L. N. Valsamis, ''A Novel Polymer Processing Machine. Theory and Experimental Results,'' *Proc. 37th Annu. Techn. Conf. of the Society of Plastics Engineers*, New Orleans, (November 1979), pp. 193–204.
11. P. Hold, Z. Tadmor, and L. V. Valsamis, ''Applications and Design of a Novel Polymer Processing Machine,'' *Proc. 37th Annu. Tech. Conf. of the Society of Plastics Engineers*, New Orleans, (November 1997), 205–211.
12. Z. Tadmor, L. N. Valsamis, P. S. Mehta, and Y. C. Yang, ''Corotating Disk Pumps for Viscous Liquids,'' *IEC Process Design Devel.*, **24**, 311–320 (1985).
13. P. S. Mehta, L. N. Valsamis, and Z. Tadmor, ''Foam Devolatilization in Multi-Channel Corotating Disk Processors,'' *Polym. Process Eng*, **2**, 103–128 (1984).
14. Z. Tadmor, ''Corotating Disk Scraped Surface Heat Exchangers,'' *Food Techn.*, Dec 1985 pp. 66–74.
15. I. Edelist and Z. Tadmor, ''Velocity Profiles in Corotating Disk Processors,'' *Polym. Process Eng*. **1**, 1 (1983).
16. B. David and Z. Tadmor, ''Extensive Mixing in Corotating Processors,'' *Int. Polym. Processing*, **3**, 28–47 (1988).
17. Z. Tadmor and I. Klein, *Engineering Principles of Plasticating Extrusion*, Van Nostrand-Reinhold, New York, 1970. (a) p. 190, (b) p. 202, (c) p. 194–199, (d) p. 397, (e) Chapters 6 and 8.
18. M. Kaufman, ''Advection and Mixing in Single Screw Extruder—An Analytic Model,'' *The AIChE Annual. Techn. Conf. Meeting Proc*., San Francisco (2003).
19. R. S. Rowell and D. Finlayson, ''Screw Viscosity Pumps,'' *Engineering*, **114**, 606 (1922); *ibid*., **126**, 249 (1928).
20. R. M. Grifith, ''Fully Developed Flow in Screw Extruders,'' *Ind. Eng. Chem. Fundam*., **1**, 180–187 (1962).
21. R. E. Colwell and K. R. Nicholls, ''The Screw Extruder,'' *Ind. Eng. Chem*., **51**, 841–843 (1959).
22. J. R. A. Pearson, *Mechanical Principles of Polymer Melt Processing*, Oxford Pergamon Press, Oxford, 1966.
23. H. Zamodits, *Extrusion of Thermoplastics*, Ph.D. Thesis, University of Cambridge, 1964; also H. Zamodits and J. R. A. Pearson, ''Flow of Melt in Polymer Extruders, Part 1. The Effect of Transverse Flow on a Superimposed Temperature Profile,'' *Trans. Soc. Rheol*., **13**, 357 (1969).
24. M. L. Booy, ''The Influence of Non-Newtonian Flow on Effective Viscosity and Channel Efficiency in Screw Pumps,'' *Polym. Eng. Sci*., **21**, 93 (1981).
25. K. P. Choo, M. L. Hami, and J. F. T. Pittman, ''Deep Channel Operating Charcteristics of a Single Screw Extruder: Finite Element Predictions and Experimental Results for Isothermal Non-Newtonian Flow,'' *Polym. Eng. Sci.*, **21**, 100 (1981).
26. J. Nebrensky, J. F. T. Pittman, and J. M. Smith, ''Flow and Heat Transfer in Screw Extruder, I. A Variational Analysis Applied in Helical Coordinates,'' *Polym. Eng. Sci.*, **13**, 209 (1973).
27. M. L. Hami and J. F. T. Pittman, ''Finite Element Solutions for Flow in a Single-Screw Extruder, Including Curvature Effects'', *Polym. Eng. Sci.*, **20**, 339 (1980).
28. J. R. A. Pearson, *Mechanics of Polymer Processing*, Elsevier, London, 1985.
29. J. F. T. Pittman and K. Rashid, ''Heat Transfer in Recirculating Extruder Channel Flow,''*J. Polym. Eng*., **5**, 1 (1985).
30. I. Bruker, C. Miaw, A. Hasson, and G. Balch, ''Numerical Analysis of the Temperature Profile in the Melt Converying Section of a Single Screw Extruder: Comparison with Experimental Data,'' *Polym. Eng. Sci.*, **27**, 504 (1987).

31. R. F. Westover, "A Hydrodynamic Screwless Extruder" *Soc Plastics Eng. J.*, **18**, 1473–1480 (1962).
32. R. E. Gaskell, "The Calendering of Plastics," *J. Appl. Mech.*, **17**, 334–336 (1950); also see D. I. Marshall and E. C. Bernhardt, in "Calendering," *Processing of Thermoplastic Materials*, Krieger, Huntington, New York, 1959, Chapter 6.
33. J. M. McKelvey, *Polymer Processing*, Wiley, New York, 1962.
34. J. T. Bergen and G. W. Scott, Jr., "Pressure Distribution in the Calendering of Plastic Materials," *J. Appl. Mech.*, **18**, 101–106 (1951).
35. C. Kiparissides and J. Vlachopoulos, "Finite Element Analysis of Calendering," *Polym. Eng. Sci.*, **16**, 712–719 (1976).
36. M. Finston, "Thermal Effects in the Calendering of Plastics Materials," *J.Appl. Mech.*, **18**, 12 (1951).
37. W. Unkrüer, "Beitrag zur Ermittlung des Druckverlaufes und der Fliessvorgange im Walzspalt bei der Kalanderverarbeitung von PVC Hart zu Folien," Doctoral Dissertation, Technische Hochschule Aachen, Aachen, Germany, 1970; see also W. Unkrüer, Kunstoffe, **62**, 7 (1972).
38. B. Maxwell and A. J. Scalora, "The Elastic Melt Extruder Works Without Screw," *Mod. Plast.*, **37**(2), 107 (1959).
39. V. L. Kocherov, Yu. L. Lukach, E. A. Sporyagin, and G. V. Vinogradov, "Flow of Melts in Disk-type Extruder," *Polym. Eng. Sci.*, **13**, 194–201 (1973).
40. P. A. Good, A. J. Schwartz, and C. W. Macosko, "Analysis of the Normal Stress Extruder," *AIChE. J.*, **20**, 67–73 (1974).
41. R. B. Bird, R. C. Armstrong, and O. Hassager, *Dynamics of Polymeric Fluids*, Vol. 1, *Fluid Mechanics*, JWiley 1977, p.397.
42. B. Maxwell, "A New Method of Solving the Feeding and Melting Zone Problems in the Normal Stress Extruder," Presented at the 31st Annu. Tech. Conf. of the Society Plastics Engineers, Montreal Canada (1975).
43. Z. Tadmor, P. S. Mehta, L. N. Valsamis and J. Yang, "Corotating Disk Pumps for Viscous Liquids," *Ind. Eng. Chem. Process Des. Devel.*, **24**, 311–320 (1985).
44. Z. Tadmor, P. Hold, and L. Valsamis, "A Novel Polymer Processing Machine" Proc. *37th Annu. Tech. Conf. of the Society of Plastics Engineers*, New Orleans, 1979; also A. Tadmor, P. Hold, and L. Valsamis, *Plast. Eng.*, Part I, 1979, pp. 193–204, Part II, 1979, pp. 34–37.
45. I. Edelist and Z. Tadmor, "Velocity Profiles in a Corotating Disk Processor," *Polym. Process Eng.*, **1**, 1 (1983).
46. W. Rose, "Fluid-Fluid Interface in Steady Motion," *Nature*, **191**, 242–243 (1961).
47. S. Bhattacharji and P. Savic, "Real and Apparent Non Newtonian Behavior in Viscous Pipe flow of Suspensions Driven by a Fluid Piston," *Proc. Heat and Mass Transfer Fluid Mechanics Institute*, **15**, 248 (1965).
48. J. R. Scott, *IRI Trans.*, **7**, 169 (1931).
49. P. J. Leider and R. B. Bird "Squeezing Flow Between Parallel Discs I. Theoretical Analysis," *Ind. Eng. Chem. Fundam.*, **13**, 336–341 (1974).
50. P. J. Leider, "Squeezing Flow between Parallel Disks II Experimental Results," *Ind. Eng. Chem. Fundam.*, **13**, 342–346 (1974).
51. A. Ishibashi, "Studies of Volumetric Efficiency and Theoretical Delivery of Gear Pumps," *Bull. Jp. Soc. Mech. Eng.*, **13**, 688–696 (1970).
52. J. F. Agassant, P. Avenas, J.-Ph. Sergent, B. Vergnes, and M. Vincent, *La Mise en Forme des Matières Plastiques, Technique et Documentation*, Paris, 1996.
53. J. L. White, *Twin Screw Extrusion Technology and Principles*, Hanser, Munich, 1990.
54. J. L. White, A. Y. Coran and A. Moet, *Polymer Mixing Technology and Engineeering*, Hanser, Munich, 2001.

55. H. Herrmann, U. Burkhardt, and S. Jacopin, "A Comprehensive Analysis of Multiscrew Extruder Mechanisms," *Proc. 35th Annu. Techn. Conf., Society of Plastics Engineers*, Montreal, Quebec, Canada (1977).
56. M. L. Booy, "Geometry of Fully Wiped Twin-Screw Equipment," *Polym. Eng. Sci.*, **18**, 973 (1978).
57. M. L. Booy, "A Noniterative Numerical Solutions of Poisson's and Laplace's Equations with Applications to Slow Viscous Flow", *Trans. ASME Series D*, **88**, 725–733 (1966); also, "Isothermal Flow of Viscous Liquids in Corotaing Twin Screw Devices," *Polym. Eng. Sci.*, **20**, 1220 (1980).
58. C. D. Denson and B. K. Hwang, "The Influence of the Axial Pressure Gradient on Flow Rate for Newtonian Liquids in a Self Wiping, Corotating Twin Screw Extruder," *Polym. Eng. Sci.*, **20**, 965 (1980).
59. W. Szydlowski and J. L. White, "An Improved Theory of Metering in an Intermeshing Co-rotating twin-screw extruder," *Adv. Polym. Technol.*, **7**, 177 (1987).
60. J. Tayeb, B. Vergnes, and G. J. Della Valle, *J. Food Sci.*, **53**, 616 (1988).
61. D. Goffart, D. J. vander Wal, E. M. Klomp, H. W. Hoogstraten, L. P. B. M Janssen, L. Bregsse, and Y. Trolez, "Three-dimensional Flow Modeling of a Self-wiping Corotating Twin-screw Extruder. Part I: The Transporting Section," *Polym. Eng. Sci.*, **36**, 901 (1996).
62. L. P. B. M. Janssen, L. P. H. R. M. Mulders, and J. M. Smith, "A Model for the Output from the Pump Zone of the Double-screw Processor or Extruder," *Plast. Polym.*, **43**, 93 (1975).
63. C. E. Wyman, "Theoretical Model for Intermeshing Twin Screw Extruders: Axial Velocity Profile in Shallow Channels," *Polym. Eng. Sci.*, **15**, 606–611 (1975).
64. L. P. B. M. Janssen, *Twin Screw Extrusion*, Elsevier, Amsterdam, 1978.
65. L. P. B. M. Janssen, J. J. Pelgrom, and J. M. Smith, *Kunststoffe*, **66**, 724 (1976).
66. L. P. B. M. Janssen, and J. M. Smith, *Plast. Rubber Process.*, **44**, 90 (1976).
67. J. A. Speur, H. Mavridis, J. Vlachopoulos, and L. P. B. M. Janssen, "Flow patterns in the calender gap of a counterrotating twin screw extruder," *Adv. Polym. Technol.*, **7**, 39 (1987).
68. K. P. Klenk, "Property-based technology for processing rigid PVC power on single- and twin screw extruders, (Beitrag zur werksoffgerechten Verarbeitung von PVC hary-Pulver auf Ein- und ZweiSchnecken- Extruder)," *Plastverarbeiter.*, **22**, 33–38 (1971).
69. K. P. Klenk, "Processing rigid PVC power on single- screw and twin- screw extruders in consistency with material properties, (Beitrag zurwerkstoffgerechten Verarbeitung von PVC hart- Pulver auf Einund Zwei- Schnecken- Extrudern)," *Plastverarbeiter.*, **22**, 105–109 (1971).
70. K. P. Klenk, *Plastverarbeiter*, **22**, 189 (1971).
71. Z. Doboczky, *Plastverarbeiter*, **16**, 58 (1965).
72. Z. Doboczky, *Plastverarbeiter*, **16**, 395 (1965).
73. A. Kaplan and Z. Tadmor, "Theoretical Model for Non-Intermeshing Twin Screw Extruders," *Polym. Eng. Sci.*, **14**, 58–66 (1974).

PROBLEMS

6.1 ***Pressurization Methods*** The equation of motion indicates the possible alternative sources of pressurization. Indicate the source of the following pressurization methods: human heart, centrifugal pump, gear pump, blow molding, volcanoes, single screw extruder, ram extruder, injection molding, compression molding, centripetal pump, and fully intermeshing co- and counterrotating screw extruder.

6.2 ***Novel Pumping Configurations*** The accompanying figure shows a series of pump configurations. Identify the building block the pump is based upon and its operation.

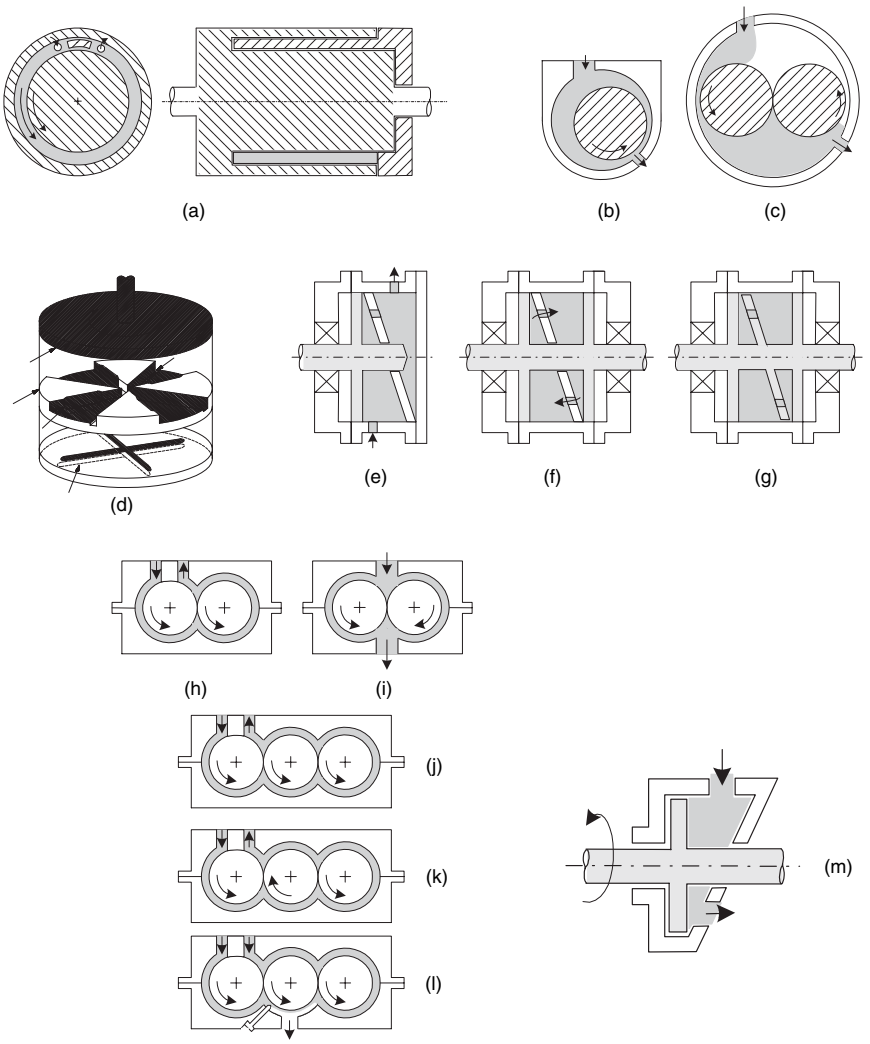

6.3 ***The Roll Pump*** Derive a mathematical model for the roll-pump [depicted in Fig. E6.1a(c)] having a barrel inner diameter, D_b, and a roll diameter, D_s, relating the flow rate, Q, pressure rise, $P_{\text{out}} - P_{\text{in}}$, and roll speed, N, to the relevant geometrical variables. Neglect back flow over the channel blade clearance.

6.4 ***Parallel-Plate Flow of Newtonian Fluids*** A Newtonian polymeric melt with viscosity $0.2\,\text{lb}_\text{f}\text{s/in}^2$ and density $48\,\text{lb/ft}^3$, is pumped in a parallel-plate pump at steady state and isothermal conditions. The plates are 2 in wide, 20 in long, and 0.2 in apart. It is required to maintain a flow rate of 50 lb/h. (a) Calculate the velocity of the moving plate for a total pressure rise of 100 psi. (b) Calculate the optimum gap size for the maximum pressure rise. (c) Evaluate the power input for the parts (a) and (b). (d) What can you say about the isothermal assumption?

6.5 ***Screw Extruders for Pumping Water*** It is claimed that the Greek mathematician Archimedes (born in Sicily about 287 B.C. and died about 212 B.C.) invented the device called the screw of Archimedes for pumping water, though the Egyptians are supposed to have had the device long before for pumping water from the Nile. Discuss the use of extruders for water pumping. What are the limitations and advantages?

6.6 ***The Freely Rotating Spiral Extruder Pump*** A free-standing spiral flight, fitted with a small clearance between a stationary barrel of diameter D_b and stationary solid cylinder of diameter D_s rotates at a constant frequency of rotation N. (a) Which building block among those listed in Fig. 6.2 is this pumping device built on? (b) Assuming a shallow-channel configuration, derive a mathematical model relating the flow rate, Q, pressure rise, $P_{out} - P_{in}$, and N, to the geometrical variable as the parameters.

6.7 ***Single-screw Pump with Inner Recycle*** A constant channel-depth single-screw pump with a linearly rising pressure has a hollow shaft, as shown in the accomapnying figure, connected to the channel such that part of the flow is recycled. Assuming isothermal Newtonian flow (a) derive and expression for the flow rate of the extruder, and (b) for the recycle rate.

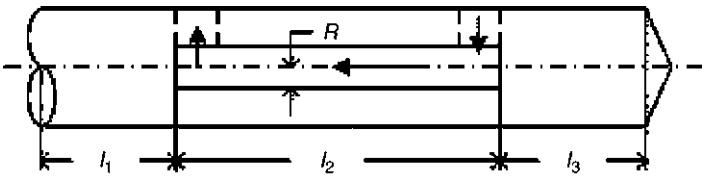

6.8 ***Flat Spiral Pump*** A spiral flight of height H is welded to a stationary disk creating a spiral channel of constant width W, as shown in the accompanying figure. By placing a second disk over the channel, a flat spiral pump is created. Clockwise rotation of the upper disk pumps liquid from the outer inlet port to the inner exit port. Derive an expression for the flow rate of an incompressible Newtonian fluid in isothermal flow.

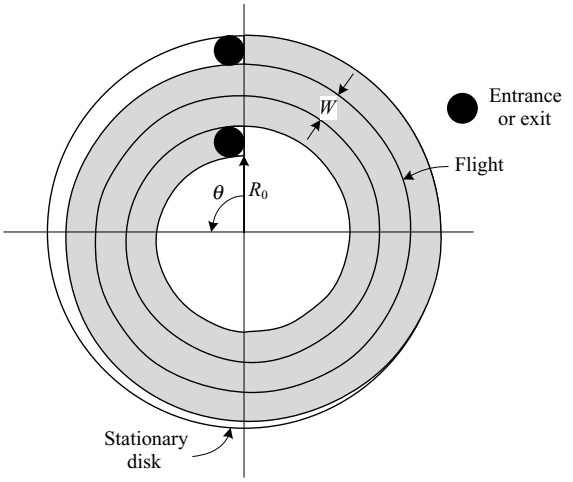

6.9 ***Partially Filled Screw Channel*** The accompanying figure below shows a partially filled screw channel. Using the single-screw Newtonian parallel plate model show that the free boundary profile is given by[19]

$$\left(1-\frac{X}{W}\right)+\frac{X_0}{W}\ln\left[\frac{1-\frac{X_0}{W}}{\frac{X}{W}-\frac{X_0}{W}}\right]=\frac{z_f-z}{W\tan\theta_b}$$

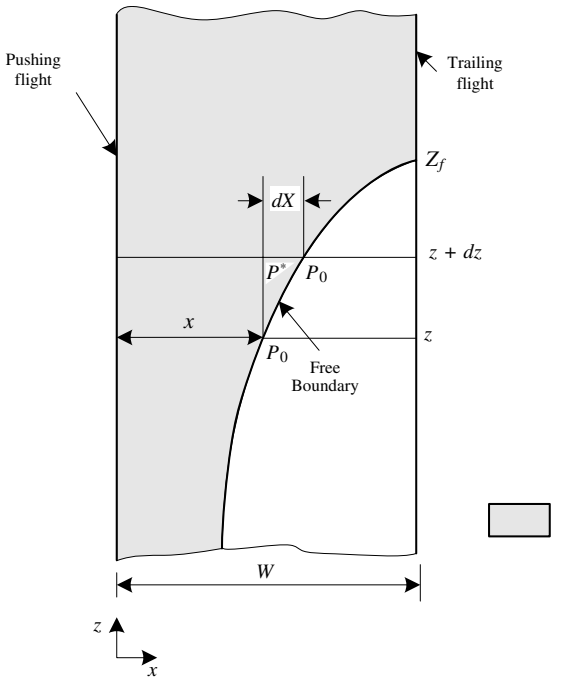

6.10 ***Blade Coating*** A schematic view of a blade-coating operation is shown in the accompanying figure. (a) Show that the coating thickness is $H_c = H_0/(1+\zeta_0)$

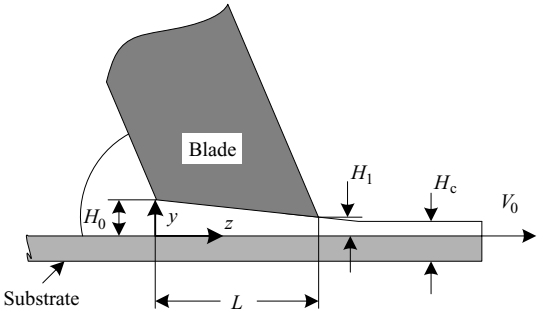

19. A. Berlis, E. Broyer, C. Mund, and Z. Tadmor, ''Flow Patterns in Aprtially Filled Extruder Screw,'' *Plastics Polym.*, **41**, 145–148 (June 1973).

where $\zeta_0 = H_0/H_1$. (b) Show that the normal force on the blade F_N is given by[20]

$$F_N = \left(\frac{6\mu L^2 W V_0}{H_0 H_1}\right)\left(\frac{1-\zeta_0(1-\ln\zeta_0)}{(\zeta_0-1)^2}\right)$$

6.11 ***Nonsymmetric Calendering***[21] Derive the pressure distribution of a Newtonian fluid in a calender (a) with different size rolls but equal peripheral speed; (b) with different speeds but equal-size rolls. Make the same simplifying assumptions that were made in the Gaskell model in Section 6.4.

6.12 ***Non-Newtonian Flow between Jointly Moving Parallel Plates (JMP) Configuration*** Derive the velocity profile for isothermal Power Law model fluid in JMP configuration.

6.13 ***Relative Efficiency of the JMP and Single Moving Plate (SMP) Configurations***[22] (a) Derive and prove Eqs. 6.6-7 and 6.6-8; (b) Show that the specific power input, and the power dissipated into heat, of the optimized JMP and SMP models are given by $(p_w)_{\text{JMP}}/(p_w)_{\text{SMP}} = 1/(1+s)$ and $(p_w^*)_{\text{JMP}}/(p_w^*)_{\text{SMP}} = 1/(1+s)$.

6.14 ***Design of Co-rotating-disk Coal-slurry Pump*** Moderately viscous suspensions of 50–70% finely pulverized coal in oil and water can be used as a substitute for liquid fuel. The suspension is a non-Newtonian Power Law model fluid with $m = 16\,\text{Ns}^n/\text{m}^2$, $n = 0.82$ at 60°C, with density $100\,\text{lb/ft}^3$, and a specific heat of 1 Btu/lb°F. Design a 100-gpm co-rotating-disk pump with 10 parallel wedge-shaped chambers and $\alpha = 0.5$, generating 100 psi head pressure. The inlet and outlet and the channel block occupies 25% of the circumference.

20. Y. Greener and S.Middleman, "Blade Coating of Viscoelastic Fluids," *Polym. Eng. Sci.*, **14**, 791–796 (1974).

21. R. E. Gaskell, "The Calendering of Plastic Materials," *J. App. Mech.*, **17**, 334–336 (1950).

22. Z. Tadmor, P. S. Mehta, L. N. Valsamis, and J. C. Yang, "Corotating Disk Pumps for Viscous Liquids," *Ind. Eng. Chem. Process Des. Devel.*, **24**, 311–320 (1985).